Nuclear Physics B149 (1979) 413–496
© North-Holland Publishing Company

EVENT SHAPES IN e^+e^- ANNIHILATION *

Geoffrey C . FOX and Stephen WOLFRAM
California Institute of Technology, Pasadena, California 91125, USA

Received 25 September 1978
(Revised 20 November 1978)

We present a complete set of rotationally invariant observables (H_l) which characterizes the 'shapes' of final states in e^+e^- annihilation. They are infrared stable when calculated in QCD perturbation theory. We compare the 'shapes' of final states from the processes $e^+e^- \to q\bar{q}$, $e^+e^- \to q\bar{q}(G)$ and from the three-gluon decays of heavy vector mesons. We also consider the production and decay of heavy quarks and leptons. Using a realistic model for the development of hadron jets, we find that for c.m. energies above about 10 GeV, these processes may be clearly distinguished by their distributions in the H_l. We indicate how our analysis may be extended to deep inelastic lepton-hadron interactions and hadron-hadron collisions involving large transverse momenta.

1. Introduction

Quantum chromodynamics (QCD) provides an increasingly successful theory for strong interactions. One of its most striking predictions is the existence of gluons. Perhaps the most direct way in which to detect these new fundamental particles is to observe the jets of hadrons resulting from their production in e^+e^- annihilation. Experiments have shown that at high energies, final states in $e^+e^- \to$ hadrons usually consist predominantly of two jets of hadrons [1] presumably coming from the quark and antiquark resulting from the process of fig. 1. QCD explains this basic two-jet structure [2] but indicates that one of the final quarks should sometimes emit a gluon (G) as in fig. 2 [3]. Such processes would tend to lead to final states containing three jets. In addition, QCD suggests that resonances containing heavy quark pairs (for example, the ψ and Υ; denoted generically by ζ) should decay predominantly into three gluons (fig. 3), again leading to three-jet final states [4]. It is, therefore, important to identify events in which three hadron jets are produced.

A number of observables which characterize the 'shapes' of final states in e^+e^-

* Work supported in part by the US Department of Energy under Contract No. EY76-C-03-0068.
A summary of parts of this work is contained in ref. [31].

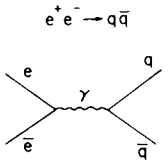

Fig. 1. The lowest-order diagram for the process $e^+e^- \to q\bar{q}$.

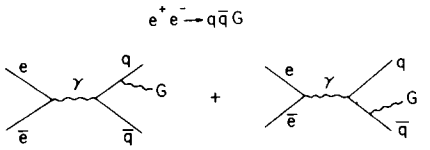

Fig. 2. The lowest-order diagrams for the process $e^+e^- \to q\bar{q}G$, where G is a vector gluon.

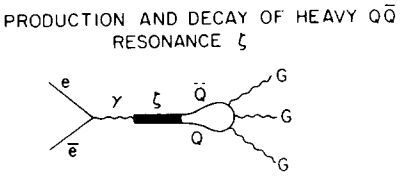

Fig. 3. The lowest-order diagram for the production and decay into three gluons of a vector meson (ζ) containing a pair of heavy quarks (Q).

annihilation have been proposed for this purpose [5,6]. There is no natural axis defined in the final state in e^+e^- annihilation. An axis may, however, be found by demanding that it minimize some observable. Such a minimization has been the basis of previous experimental (sphericity) and theoretical (spherocity, thrust, acoplanarity) observables designed to measure the structure of final states in e^+e^- annihilation. For the observables of theoretical interest, the minimization has turned out to be inconvenient to implement [24]. Moreover, this procedure may induce spurious jet structure. The minimization would probably be satisfactory if all events had a two-jet structure; according to QCD, however, more than 30% of the events in non-resonant e^+e^- annihilation at c.m. energies around 20 GeV should consist of three or more jets, so that methods based on finding an optimal two-jet axis appear suspect. The problem of minimization can, however, be circumvented by measuring an observable which characterizes the 'shapes' of final states, but whose value does not depend on the axis used to evaluate it. A set of such observables exists, given by (the $Y_l^m(\Omega)$ are the usual spherical harmonics, and $P_l(\cos\phi)$ the Legendre polynomials)

$$H_l \equiv \frac{4\pi}{2l+1} \sum_{m=-l}^{+l} \left| \sum_i Y_l^m(\Omega_i) \frac{|\boldsymbol{p}_i|}{E_{\text{tot}}} \right|^2 = \sum_{i,j} \frac{|\boldsymbol{p}_i||\boldsymbol{p}_j|}{E_{\text{tot}}^2} P_l(\cos\phi_{ij}) \qquad (1.1)$$

where the indices i and j run over the hadrons which are produced in the event, and ϕ_{ij} is the angle between particles i and j. When the first form for the H_l is used, one must choose a particular set of axes to evaluate the angles (Ω_i) of the momenta of the final-state particles, but the values of the H_l deduced will be independent of the choice. Note that the H_l constitute a complete set of shape parameters in a way that is made precise in sect. 2. Energy-momentum conservation requires that $H_0 \simeq 1$, $H_1 = 0$. The process $e^+e^- \to q\bar{q}$ gives $H_l = 1$ for even l, and $H_l = 0$ for odd l, since the final quark momenta are collinear.

The processes $e^+e^- \to q\bar{q}G$ and $e^+e^- \to \zeta \to GGG$ give final states for which there are many possible kinematic configurations, corresponding to a range of possible 'shapes'. These processes therefore lead to distributions in the H_l which are very different from the delta function due to $e^+e^- \to q\bar{q}$. For example, the process $e^+e^- \to \zeta \to GGG$ yields a $d\sigma/dH_2$ which is nearly flat over the range $0.25 \leqslant H_2 \leqslant 1$ allowed by kinematics, while $e^+e^- \to q\bar{q}$ gives only $H_2 = 1$. The fragmentation of the quarks and gluons into hadrons serves to distort the distributions of 'shapes', but at sufficiently high energies ($\sqrt{s} \gtrsim 10$ GeV), hadronic final states resulting from each of the three subprocesses of figs. 1–3 should be clearly distinguished by measuring their distributions in H_l/H_0.

The multi-jet final states resulting from decays of pairs both of heavy mesons carrying new flavors and of heavy leptons may also be identified by measurements of their 'shapes' using the H_l.

This paper is organized as follows. In sect. 2, we discuss various mathematical aspects of the H_l, define the 'correlation function' $F(x)$ and give examples of the H_l for simple shapes. We also present some generalizations of the H_l. In sect. 3, we discuss the definition of jets in QCD and give arguments for the infrared finiteness of the H_l calculated from perturbation theory. Sect. 4 describes our results for the processes $e^+e^- \to q\bar{q}$, $e^+e^- \to q\bar{q}G$, $e^+e^- \to \zeta \to GGG$ and for the production and decay of heavy quarks and leptons. In sect. 5, we present results for realistic hadronic final states formed by the various quark-gluon subprocesses discussed in sect. 4. Sect. 6 contains a brief discussion of a class of shape parameters which exploit the correlation between the direction of the incoming beam axis and the configuration of the final state. Sect. 7 considers the extension of our H_l analysis to deep inelastic lepton-hadron interactions and in sect. 8 we give a very brief discussion of two-dimensional analogues of the H_l. These are relevant to processes in which a natural plane is defined; the most important applications appear to be large $p_\perp$ hadron reactions and deep inelastic lepton-hadron scattering. The appendix summarizes the kinematics for three-jet production.

2. The harmonic moments H_l and the correlation function F

2.1. Properties of the H_l

Consider a sphere placed symmetrically around an e^+e^- annihilation event. Mark the point at which each produced particle pierces the sphere, and assign to it a weight equal to the magnitude of the momentum of the particle divided by the total center of mass energy. A convenient analogy to this system is a set of point masses placed on the surface of a sphere at each of the points (Ω_i) marked, and with magnitudes (m_i) equal to the weights previously assigned. Momentum conservation for the particle event will cause the center of mass of the resulting body to be at its geometrical center and energy conservation requires its total mass to be one. Now, corresponding to eq. (1.1), define

$$H_l \equiv \frac{4\pi}{2l+1} \sum_{m=-l}^{+l} \left| \sum_i Y_l^m(\Omega_i)\, m_i \right|^2 = \sum_{i,j} m_i m_j P_l(\cos\phi_{ij}) , \tag{2.1}$$

so that the values of the H_l for the mass distribution will be the same as those for the particle event from which it was derived. In this section it will usually be convenient to work with continuous distributions of mass on the surface of the sphere, rather than with sets of point masses, as above. Many of our results will also apply to the limiting case of point masses.

For continuous distributions of mass $\rho(\Omega)$, let

$$H_l \equiv \frac{4\pi}{2l+1} \sum_{m=-l}^{+l} \left| \int \rho(\Omega)\, Y_l^m(\Omega)\, \mathrm{d}\Omega \right|^2 \tag{2.2}$$

$$= \sum_m \left| \int \rho(\Omega)\, D^{l\,*}_{m0}(\Omega)\, \mathrm{d}\Omega \right|^2 .$$

The H_l provide a characterization of the mass distribution independent of the set of axes used to determine them. Each H_l is, in fact, simply a sum of the absolute squares of the $2l+1$ order-l multipole moments of the mass distribution. Note that, unlike multipole moments, the $H_l[\rho]$ are not linear functionals of ρ: $H_l[\rho_1 + \rho_2] \neq H_l[\rho_1] + H_l[\rho_2]$. (A restricted linear superposition principle does, however, hold. See subsect. 4.6.) Note also that $0 \leqslant H_l/H_0 \leqslant 1$.

To prove that the H_l as defined in eq. (2.2) are indeed rotational invariants (independent of choice of axes), define the multipole moments

$$A_l^m \equiv \int \rho(\Omega)\, Y_l^m(\Omega)\, \mathrm{d}\Omega . \tag{2.3}$$

Then

$$H_l = \frac{4\pi}{2l+1} \sum_m |A_l^m|^2 . \tag{2.4}$$

Now apply a rotation R to the coordinate axes. The multipole moments with respect to the new set of axes are

$$(A_l^m)' = \int \rho(\Omega)\, Y_l^m(R^{-1}\Omega)\, \mathrm{d}\Omega$$

$$= \sum_{m'} D^{l\,*}_{mm'}(R^{-1}) \int \rho(\Omega)\, Y_l^{m'}(\Omega)\, \mathrm{d}\Omega\,, \tag{2.5}$$

so that

$$\frac{2l+1}{4\pi}(H_l)' \equiv \sum_m |(A_l^m)'|^2$$

$$= \sum_m \Big[\sum_{m'} D^{l\,*}_{mm'}(R^{-1}) \int \rho(\Omega)\, Y_l^{m'}(\Omega)\, \mathrm{d}\Omega \Big]$$

$$\times \Big[\sum_{m''} D^{l\,*}_{m''m}(R) \int \rho(\Omega)\, Y_l^{m''\,*}(\Omega)\, \mathrm{d}\Omega \Big] \tag{2.6}$$

$$= \sum_{m'} \sum_{m''} \delta_{m'm''} \Big[\int \rho(\Omega)\, Y_l^{m'}(\Omega)\, \mathrm{d}\Omega \Big] \Big[\int \rho(\Omega)\, Y_l^{m''\,*}(\Omega)\, \mathrm{d}\Omega \Big]$$

$$= \frac{2l+1}{4\pi} H_l\,.$$

This completes the proof of the rotational invariance of the H_l, which was, in fact, already manifest in the second definition of H_l in eq. (1.1).

Unlike multipole moments, the H_l do not contain all the information necessary to reconstruct the mass distribution $\rho(\Omega)$. Information on the 'relative phases' of multipole moments of different orders has been lost. The relative amounts which multipole moments of a particular l but different m contribute to H_l cannot be determined. For example, the two distributions $[Y_2^0(\Omega) + Y_3^0(\Omega)]$ and $[Y_2^0(\Omega) + Y_3^0(Q\Omega)]$ (Q is any non-trivial rotation) will have the same H_l. Use of the observables discussed in subsect. 2.7 would, however, serve to remove this ambiguity.

2.2. *The correlation function F*

Although the H_l do not uniquely determine $\rho(\Omega)$, they do determine the 'density correlation function' *

$$F(x = \cos\beta) = 2 \int \rho(\hat{\Omega})\, \rho^*(\hat{\Omega}\hat{R}\,(\alpha, \beta, \gamma))\, \mathrm{d}\hat{\Omega}\,, \tag{2.7}$$

* This is similar to the 'rotation function' used in crystallography [7].

where $\hat{\Omega}$ and $\hat{R}$ are now both operators in the rotation group. The integral is over all possible rotations $\hat{\Omega}$, parametrized by three Euler angles. $\rho(\hat{\Omega})$ is the value of ρ at the point reached by applying the rotation operator Ω to the z-axis of the chosen coordinate system. $\rho(\hat{\Omega}\hat{R})$ is the value of ρ at the point reached by applying first $\hat{R}$, then $\hat{\Omega}$, to the z-axis. $\rho(\hat{\Omega})$ is given in terms of the multipole moments defined in eq. (2.3) by

$$\rho(\hat{\Omega}) = \sum_{l,m} \left(\frac{2l+1}{4\pi}\right)^{1/2} A_l^m D_{m0}^l(\hat{\Omega}) , \tag{2.8}$$

so that

$$\rho(\hat{\Omega}\hat{R}) = \sum_{l',m'} \left(\frac{2l'+1}{4\pi}\right)^{1/2} A_{l'}^{m'} D_{m'm''}^{l'}(\hat{\Omega}) D_{m''0}^{l'}(\hat{R}) . \tag{2.9}$$

Substituting these forms into the definition (2.7), one obtains

$$\begin{aligned} F(x = \cos\beta) = & \sum_{l,m,l',m',m''} \frac{\sqrt{(2l+1)(2l'+1)}}{2\pi} \int A_l^m (A_{l'}^{m'})^* D_{m0}^l(\hat{\Omega}) \\ & \times D_{m'm''}^{l'*}(\hat{\Omega}) D_{m''0}^{l'*}(\hat{R}(\alpha,\beta,\gamma))\, d\hat{\Omega} \\ = & \sum_l 4\pi |A_l^m|^2 D_{00}^l(\hat{R}(\alpha,\beta,\gamma)) \\ = & \sum_l (2l+1) H_l P_l(\cos\beta) . \end{aligned} \tag{2.10}$$

$F(x)$ is clearly a rotational invariant: any rotation of the coordinate axes may be absorbed into a redefinition of the integration measure in eq. (2.7). Note that eq. (2.10) shows that $\int_{-1}^{1} F(x)\, dx = 2H_0 = 2$.

Since the $P_l(x)$ form a complete set of functions of x, all the information which the H_l carry is, in fact, contained in the 'density correlation function' $F(x)$ which may be calculated from them.

2.3. The geometrical construction for F

The form (2.7) leads to a simple geometrical picture for $F(x)$. Select a point P on the sphere. Draw around that point a circle C which subtends an angle β with P at the center of the sphere, as illustrated in fig. 4. Then find the integral of $\rho(\Omega)$ around the circumference of the circle C, and multiply the result by the value of $\rho(\Omega)$ at P. $F(\cos\beta)$ is now obtained by integrating over all possible points P on the sphere.

As a first example of this procedure, take the mass on the surface of the sphere to be contained completely within two small circular caps (A,A′) centered at antipodal points (an analogy to a 2-jet event). This mass distribution is shown in fig. 6.

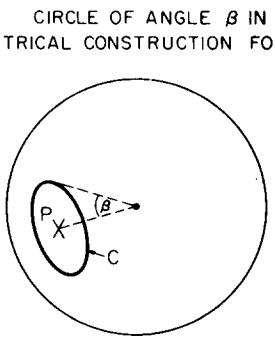

Fig. 4. Definition of the circle C used in the geometrical construction for the 'correlation function' $F(x)$.

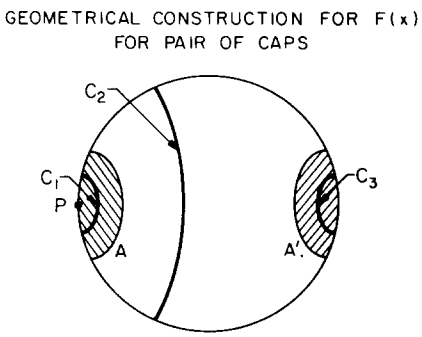

Fig. 5. Circles used in the geometrical construction for the 'correlation function' $F(x)$ of a mass distribution consisting of two antipodal caps.

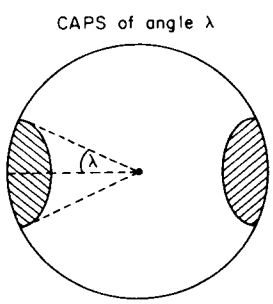

Fig. 6. Mass distribution consisting of two antipodal caps with finite density subtending half-angles λ at the center of the sphere.

Unless P lies within one of these caps, it can give no contribution to $F(x)$, since $\rho(\Omega) = 0$ elsewhere. Choose P to be in one of the caps of finite density. If β is small, then C (the circle centered at P used to evaluate $F(x)$) will be within the $\rho \neq 0$ region which surrounds the point P chosen, and for those values of β, $F(x)$ will therefore be non-zero. If β is larger, then C will lie in the region between A and A', where $\rho = 0$. For these values of β, $F(x) = 0$. Finally, if β is nearly π, then C will lie within the cap A' around the point antipodal to P on the sphere, so that $F(x)$ will again be non-zero. The three circles used in this estimation of $F(x)$ are shown in fig. 5. We have now found the form of $F(x)$ for a mass distribution consisting of two small caps centered at antipodal points: $F(x)$ will be large for x around ± 1 and will fall rapidly to zero away from these points.

The same procedure may be used to find $F(x)$ for a uniform mass distribution ('spherical' event). In this case, the circle C at angle β around any point on the sphere will contribute to $F(x)$ an amount 2π, independent of β, so that $F(x)$ = constant.

The form of $F(x)$ for a uniform distribution of mass may also be found in other ways. $\rho(\Omega) = 1/4\pi$ corresponds to a total mass 1 distributed uniformly on the surface of the sphere. Substituting this form for $\rho(\Omega)$ into eq. (2.7), one finds $F(x) = 1$. The constant value of $F(x)$ for a uniform mass distribution found by the geometrical method is thus determined to be 1. This result may also be obtained using the expression (2.10) for $F(x)$ in terms of the H_l. For a uniform mass distribution (with unit total mass), $H_0 = 1$ and $H_l = 0$ for $l > 1$. The formula (2.10) then gives $F(x) = P_0(\cos\beta) = 1$.

2.4. *Typical forms of F(x) and the H_l for continuous mass distributions*

In this subsection, we consider some examples of the forms of $F(x)$ and the H_l for various continuous mass distribution. The case of point masses (particle events) has several subtleties, and is discussed in subsect. 2.5.

As a first example, we choose the two-cap mass distribution introduced in subsect. 2.3. We take the density in the caps to be constant, and the total mass contained within them to be 1. For this mass distribution

$$
\begin{aligned}
H_l &= \frac{1}{4(1-\cos\lambda)^2}\left[\int_{\cos\lambda}^{1} P_l(z)\,dz + \int_{-1}^{-\cos\lambda} P_l(z)\,dz\right]^2 = 0\,, \qquad (l \text{ odd})\,, \\
&= \left[\frac{\sin^2\lambda}{(1-\cos\lambda)\,l(l+1)}\,\frac{dP_l}{dx}\bigg|_{x=\cos\lambda}\right]^2, \qquad (l \text{ even})\,, \qquad (2.11) \\
&\sim \frac{1}{l^3}\,, \qquad (l \to \infty)\,,
\end{aligned}
$$

where λ is half the angle subtended by the cap at the center of the sphere (see fig. 6). As for any mass distribution which is invariant under an inversion about the center

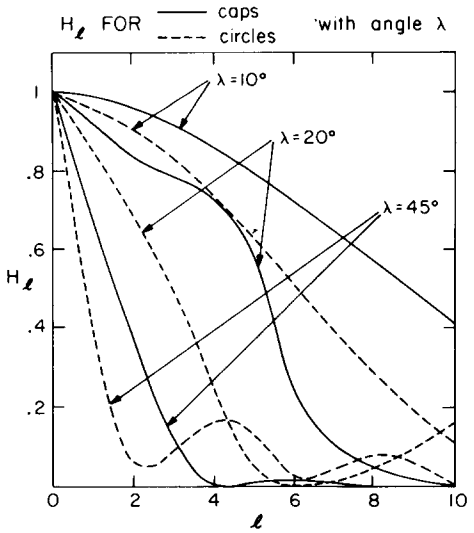

Fig. 7. The shape parameters H_l for mass distributions consisting of caps and circles with angles λ, as illustrated in figs. 6 and 8, respectively. Note that the inversion symmetry of both configurations leads to $H_l = 0$ for odd l. The values of the H_l only for l an even integer are, in fact, plotted in the figure; the points are joined for ease of reading.

of the sphere, the H_l in this case are zero for all odd values of l. The H_l for a selection of values of λ are given in fig. 7. For comparison, the H_l for circular line masses subtending the same angles (see fig. 8) are also given (dashed lines). The points in fig. 7 have been joined by smooth curves for ease of reading, but it should be noted that only the H_l for even integer values of l are, in fact, plotted. The forms of $F(x)$ for

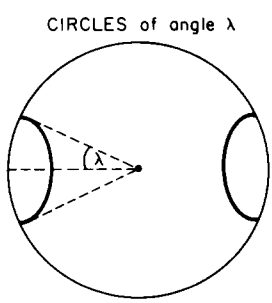

Fig. 8. Mass distribution consisting of two antipodal circular line masses subtending half-angles λ at the center of the sphere.

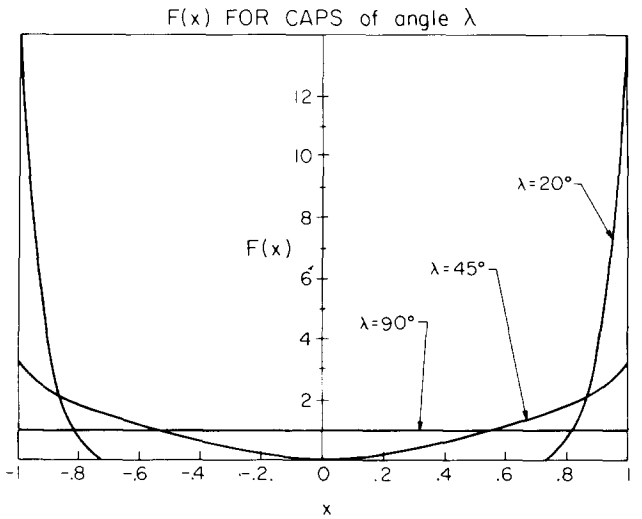

Fig. 9. The 'correlation function' $F(x)$ for mass distributions consisting of antipodal caps subtending half-angles λ at the center of the sphere (see fig. 6). $\lambda = 90°$ corresponds to a uniform distribution of mass on the sphere, while $\lambda = 0°$ represents two point masses placed at antipodal points.

caps of various sizes λ (fig. 6) are plotted in fig. 9. As expected on the basis of the geometrical construction described above, $F(x) = 0$ for $|x| \leqslant \cos(2\lambda)$, since in this case the circle C can never pass through a region of finite density. For $\lambda > 45°$, $F(x)$ is therefore never zero. To show the rate of convergence of the series expression for $F(x)$ (see below), the value of $|F(0)|$ has been plotted in fig. 10 as a function of the maximum l included in the sum (2.10), for various cap sizes.

The cap mass distribution is analogous to an event consisting of two hadron jets. A loose analogy to a three-hadron jet event is provided by a band of finite density centered on the equator of the sphere, with angular thickness $2\lambda > 0$ (see fig. 11). If $\lambda = 0$, this mass distribution reduces to a line mass around the equator of the sphere. In this case

$$\begin{aligned} H_l &= 0\,, \qquad (l \text{ odd})\,, \\ &= |P_l(0)|^2 = \left(\frac{(l-1)!!}{(l/2)!\,2^{l/2}}\right)^2\,, \qquad (l \text{ even})\,, \\ &\sim \frac{1}{l}, \qquad (l \to \infty)\,, \end{aligned} \tag{2.12}$$

where, once again, the inversion symmetry of this mass distribution causes all the

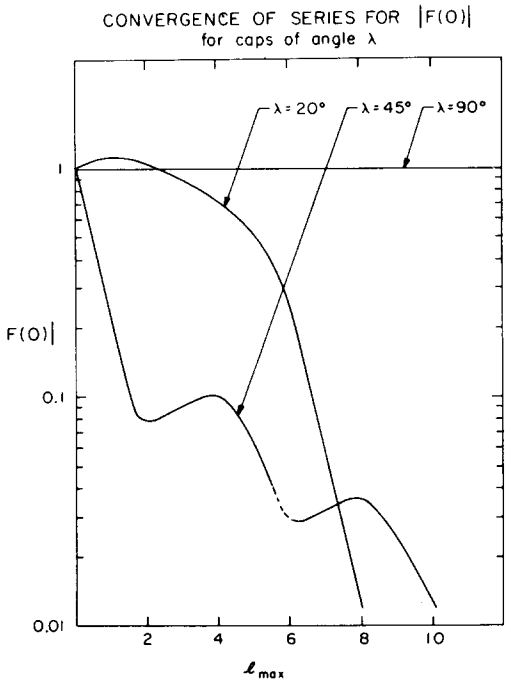

Fig. 10. Example of the convergence of the series (2.10) for the 'correlation function' $F(x)$. The value of $|F(0)|$ for caps with half-angle λ (see fig. 6) is plotted as a function of the value (l_{max}) of l at which the series has been truncated. Only points for which l_{max} is an even integer are, in fact, plotted in the figure; they are joined for ease of reading. The exact value of $|F(0)|$ is zero for caps with $\lambda \leqslant 45°$, and is 1 for $\lambda = 90°$ (corresponding to a uniform mass distribution).

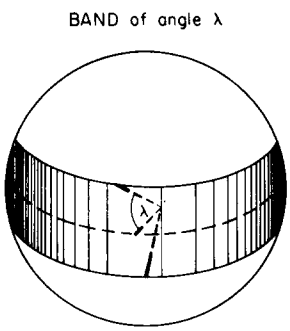

Fig. 11. Mass distribution consisting of an equatorial band of finite density subtending an angle 2λ at the center of the sphere.

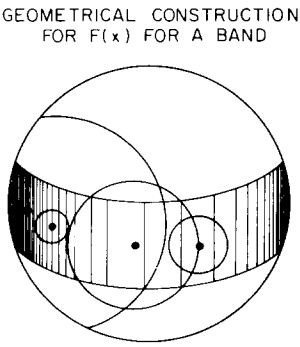

Fig. 12. Typical circles used in the geometrical construction for the 'correlation function' $F(x)$ for an equatorial band of mass.

H_l for odd l to vanish. If $\lambda \neq 0$, then

$$H_l = \frac{1}{4\sin^2\lambda}\left[\int_{-\sin\lambda}^{\sin\lambda} P_l(z)\,dz\right]^2 = 0\,, \qquad (l \text{ odd})\,,$$

$$= \left[\frac{\cos^2\lambda}{l(l+1)\sin\lambda}\,\frac{dP_l}{dx}\bigg|_{x=\sin\lambda}\right]^2, \qquad (l \text{ even})\,, \tag{2.13}$$

$$\sim \frac{1}{l^3}\,, \qquad (l \to \infty)\,.$$

The geometrical construction described above gives some indication of the form of $F(x)$ for an equatorial mass band. A circle of any size centered in the band will always lie within the band for some fraction of its circumference (see fig. 12). $F(x)$ will, therefore, never be zero. Circles with small angular radii $\beta(=\cos^{-1}x)$ will usually lie completely inside the band so that $F(x)$ will be large for x close to one. For smaller x (larger circle radii), much of the circles' circumferences will be outside the band of finite density, so that $F(x)$ will then be smaller. Finally, when x approaches -1, the circles centered at one point on the band will lie in the antipodal region of the band. For an equatorial band of mass, therefore, $F(x)$ will be large for x near ± 1, and smaller, but not zero, in between. As the thickness λ of the band decreases, so the widths of the peaks in $F(x)$ around $x = \pm 1$ will decrease. The exact form of $F(x)$ for equatorial mass bands of various thicknesses are shown in fig. 13.

In the case $\lambda = 0°$, corresponding to a line mass around the equator of the sphere, the series (2.10) for $F(x)$ may be summed exactly:

$$F(x) = \sum (2l+1)\,H_l P_l(x) \tag{2.14}$$

$$= \sum_{\text{even } l} (2l+1)|P_l(0)|^2 P_l(x) = \frac{2}{\pi\sqrt{1-x^2}}\,.$$

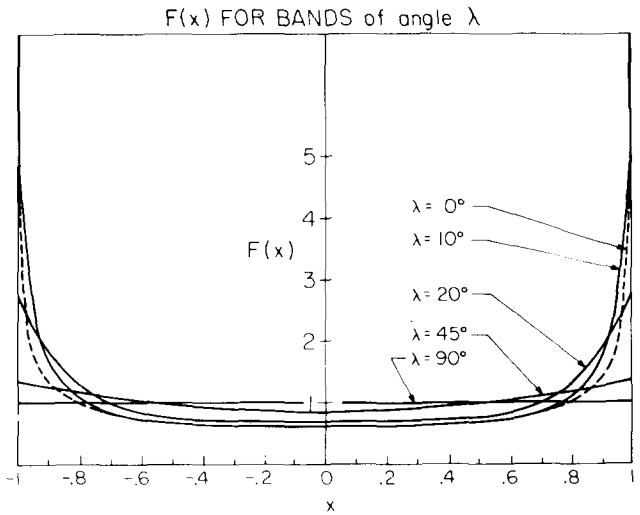

Fig. 13. The 'correlation function' $F(x)$ for mass distributions consisting of equatorial bands of finite density subtending a half-angle λ at the center of the sphere (see fig. 11). $\lambda = 90°$ corresponds to a uniform distribution of mass on the sphere. $\lambda = 0°$ corresponds to an equatorial line mass, for which $F(x)$ may be obtained in closed form (eq. (2.14)).

This result may be understood on the basis of the geometrical construction for $F(x)$ described above. Consider any point on the equator (all are equivalent). The mass density measured with respect to this point is given by

$$d\sigma(\Omega) = \left[\frac{\delta(\alpha) + \delta(\alpha - \pi)}{2\pi}\right] \frac{d(\cos\beta)d\alpha}{\sin\beta} \quad , \tag{2.15}$$

where β is the polar angle defined in subsect. 2.3 ($\cos\beta = x$) and α is an azimuthal angle. Integrating over the angle α, and summing over all possible points chosen on the equator, one finds $F(x) = 2/(\pi \sin\beta)$, which is eq. (2.15).

The curve for $\lambda = 90°$ in fig. 13. corresponds to a uniform distribution of mass on the sphere. This case is analogous to a phase-space (isotropic) distribution of particles.

We now discuss the behavior of the H_l at large l and the convergence of the series for $F(x)$. For piecewise differentiable density functions with azimuthal symmetry, $\rho(x)$, the formula (2.2) for the H_l may be integrated by parts to give

$$H_l = |[\rho(x)\, I_l(x)] - \int \frac{d\rho(x)}{dx}\, I_l(x)\, dx|^2 \, ,$$

$$I_l(x) = \int_x^1 P_l(y)\, dy = \sqrt{1 - x^2}\, P_l^{-1}(x) \tag{2.16}$$

$$\sim \frac{1}{l^{3/2}}, \qquad (l \to \infty) \, ,$$

where a suitable sum over the continuous pieces of $\rho(x)$ is understood. Hence in most cases,

$$H_l \sim \frac{1}{l^3}, \qquad (l \to \infty). \tag{2.17}$$

This may be seen explicitly from the expressions (2.11) and (2.13) for the H_l for cap and band mass distributions. For mass distributions with special symmetries, the H_l may decrease faster than l^{-3}. For example, if $\rho(x) \sim x^n$ in each hemisphere, then $H_l \sim l^{-3-2n}$ for large l. Reasonably smooth mass distributions, therefore, give rise to a series for $F(x)$ whose terms decrease like l^{-2} or faster for large l, so that the sum converges. In practice, this asymptotic behavior does not set in until very large values of l are reached.

2.5. F(x) and the H_l for point mass distributions

To begin this subsection, we discuss the values of the H_l for a few point mass distributions. The results are summarized in table 1. In the 'triangle' configuration, three equal point masses are taken to lie at the vertices of an equilateral triangle contained within the sphere. Note that this mass distribution is not invariant under inversions, so that the H_l for it are non-zero even for odd values of l. Notice also that the values of H_l do not always decrease smoothly with l; they are slightly enhanced when l is a multiple of the periodicity of the mass distribution.

The most distinctive feature of the H_l for point mass distributions is their behavior at large l. In subsect. 2.4, we showed that the H_l for continuous mass distributions decrease at least as fast as $1/l^3$ as $l \to \infty$. On the other hand, the H_l for point

Table 1
Values of the H_l for some simple point mass distributions

	Mass distribution				
	Uniform	Two antipodal points	Equatorial line	Triangle	Square
H_0	1	1	1	1	1
H_1	0	0	0	0	0
H_2	0	1	0.25	0.25	0.25
H_3	0	0	0	0.63	0
H_4	0	1	0.14	0.14	0.69
H_5	0	0	0	0.27	0
H_6	0	1	0.10	0.55	0.34
H_7	0	0	0	0.18	0
H_8	0	1	0.08	0.28	0.64

mass distributions tend to a constant for large l. The fact that the H_l do not decrease with l for point mass distributions is evidenced by the case of two-jet events, for which $H_{2l} = 1, H_{2l+1} = 0$. For a point mass distribution

$$\rho(\Omega) = \sum_i m_i \delta(\Omega - \Omega_i) , \tag{2.18}$$

so that the corresponding $F(x)$ as defined by eq. (2.7) is

$$F(x) = 2\sum_{i,j} m_i m_j \delta (\cos \phi_{ij} - x) , \tag{2.19}$$

where ϕ_{ij} is the angle between the masses i and j. For particle events, the m_i in (2.19) are replaced by $|\boldsymbol{p}_i|/\sqrt{s}$. There will be a contribution to the sum in (2.19) from the case $i = j$ of

$$F_{\text{same}}(x) = 2\sum_i m_i^2 \delta(1 - x) . \tag{2.20}$$

The behavior of the H_l for large l is most conveniently studied using the second form in the basic definition (2.1). As l tends to infinity, only the terms where $\cos \phi_{ij} = \pm 1$ survive; the other contributions decrease like $1/\sqrt{l}$. The H_l, therefore, tend to a non-zero limit as $l \to \infty$ given by

$$\lim_{l\to\infty} [H_{2l} + H_{2l+1}] = 2\sum_i m_i^2 , \tag{2.21a}$$

$$\lim_{l\to\infty} [H_{2l} - H_{2l+1}] = 2\sum_{i,j'} m_i m_{i'} , \tag{2.21b}$$

where in (2.21b), we sum over all pairs of particles i and i' which are back-to-back ($\cos \phi_{ii'} = -1$). For two-jet events, the two sums in (2.21a,b) are equal so that $H_{2l} = 1, H_{2l+1} = 0$. In most cases, the sum in (2.21b) is zero and we find that H_l tends to the same limit for odd and even l. Note that the value of this limit is just one half the coefficient of $\delta(1 - x)$ in $F(x)$. This is evident from the Legendre expansion (2.10) for $F(x)$.

2.6. Energy correlation functions and their relation to F(x)

For particle events, we define the two-detector energy correlation function

$$\tilde{F}_2(\sigma_1, \sigma_2) = \frac{16\pi^2}{|\sigma_1||\sigma_2|} \frac{|\boldsymbol{p}|_1 |\boldsymbol{p}|_2}{s} , \tag{2.22}$$

where $|\boldsymbol{p}|_i$ are the total three-momenta (or energies, if all the particles are massless) incident on detectors covering the regions σ_i of total solid angle $|\sigma_i|$. We form the rotationally invariant observable F_2 by averaging $\tilde{F}_2$ over all possible positions for

the detectors, while maintaining their relative orientation. In the limit $|\sigma_i| \to 0$, F_2 becomes a function only of the angle β between the two point detectors, and is identical to $F(\cos\beta)$. Hence the H_l are simply the coefficients in the Legendre expansion for F_2 in the limit $|\sigma_i| \to 0$ *. The set of H_l and $F(x)$ provides the same information about the shape of events, but the information is differently arranged in the two cases. However, while the H_l are infrared stable and therefore computable in QCD perturbation theory for finite l, the limit of the H_l as $l \to \infty$ is not. Since $F(x)$ probes this limit through the sum (2.10), it too is not infrared stable. This failing of $F(x)$ will be discussed in more detail in subsect. 3.4.

It is possible to regain results for F_2 in the case $|\sigma_i| \neq 0$ from $F(x)$ by integrating it over x with a suitable weighting function. For example, if the σ_i are caps of angular radius δ with centers an angle χ apart, then

$$F_2(\sigma_1, \sigma_2) = \frac{4\pi^2}{|\sigma_1||\sigma_2|} \sum_k (2l+1) I_l^2(\cos\delta)\, P_l(\cos\chi) H_l\,, \tag{2.23}$$

where the $I_l(\chi)$ are defined in eq. (2.16). This series converges for finite δ even though the H_l do not decrease with l. On comparing eq. (2.23) with eq. (2.10), one sees that the series for $F_2(\sigma_1, \sigma_2)$ has an extra $1/l^3$ convergence factor compared to that for $F(x)$. From eq. (2.23) it is possible to relate the mean value of F_2 over events to the mean values of the H_l. However, the distributions of events in H_l and in F_2 are not related. We shall discuss the distribution $(1/\sigma)\, d\sigma/dF_2$ in a later publication [29].

2.7. *Generalizations of the H_l*

The H_l form a complete set of rotationally invariant shape parameters bilinear in the density function ρ. One can find further rotationally invariant shape parameters only by considering higher powers of ρ, or equivalently, the multipole moments A_l^m defined in eq. (2.3). To find shape parameters of degree n in ρ, one must combine the n spherical tensors $A_{l_i}^{m_i}$ in such a way as to form a scalar under the rotation group. This may be done using $3j$ symbols. For example, the degree 3 analogue

* As discussed in subsect. 2.4, one must, in practice, know the values of the H_l up to rather high l in order to obtain a good approximation to $F(x)$. Note that the mean $F(x)$ has been computed directly for the process $e^+e^- \to q\bar{q}(G)$ in ref. [28], and all the processes discussed in this paper in ref. [29]. In these references, the form of $\langle F(x)\rangle$ for detectors at a fixed angle to the beam axis have also been calculated. The resulting correlation functions may be expressed as a Legendre expansion analogous to (2.10), in terms of the non-rotationally-invariant observables

$$H_l^{\alpha\beta} = \left(\frac{4\pi}{2l+1}\right) \sum_m \left[\sum_i \frac{|p_i|}{\sqrt{s}}\, Y_l^m(\Omega_i)\, P_\alpha(\Omega_i)\right] \left[\sum_j \frac{|p_j|}{\sqrt{s}}\, Y_l^m(\Omega_j)\, P_\beta(\Omega_j)\right]^* .$$

of the H_l is

$$T^3_{l_1 l_2 l_3} = (4\pi)^{3/2} \sum_{m_1,m_2,m_3} \begin{pmatrix} l_1 & l_2 & l_3 \\ m_1 & m_2 & m_3 \end{pmatrix} A^{m_1}_{l_1} A^{m_2}_{l_2} A^{m_3}_{l_3} , \qquad (2.24)$$

$$|l_1 - l_2| \leqslant l_3 \leqslant |l_1 + l_2| .$$

In this formalism the H_l are given by the only scalar (spin-0) combination of two spherical tensors:

$$(-1)^l \sqrt{2l+1}\, H_l \equiv T^2_{l_1 l_2} = 4\pi \sum_{m_1,m_2} \begin{pmatrix} l_1 & l_2 & 0 \\ m_1 & m_2 & 0 \end{pmatrix} A^{m_1}_{l_1} A^{m_2}_{l_2} , \qquad (2.25)$$

where, of course, the result is only non-zero if $l_1 = l_2 = l$. The formalism may easily be used to construct higher degree shape parameters, but for $n > 3$ there is more than one way of combining n spherical tensors to give a scalar.

The complete set of $T^n_{l_1 \ldots l_n}$ appear rather powerful since they determine $\rho(\Omega)$ up to an arbitrary overall rotation. (This is easy to show for the two-dimensional analogues of the $T^n_{l_1 \ldots l_2}$ which are generalizations of the C_l observables discussed in sect. 8.)

It turns out that observables formed from combinations of various $T^3_{l_1 l_2 l_3}$ provide a test for planes of particles in e^+e^- annihilation events *: the observables vanish for events in which all the particles are coplanar, but have a non-zero value for isotropic events. They, therefore, offer the possibility of a direct discrimination between events arising from the production of three quarks and gluons (e.g., $e^+e^- \to \zeta \to GGG$) and pure phase-space events. These observables are discussed in more detail in ref. [17].

3. Infrared stability

Graphs in which gluons or quarks may be soft, or may become collinear, receive divergent contributions from these kinematic configurations. The Kinoshita-Lee-Nauenberg (KLN) theorem guarantees, however, that in the total cross section such divergences cancel, leaving a finite result [8]. The divergences encountered in the calculation of the moments of the H_l,

$$\langle H^P_l \rangle = \frac{\int H^P_l \, d\sigma}{\int d\sigma} , \qquad (3.1)$$

* The simplest example of this class of observables is

$$\tfrac{2}{9}[H_0 - 3H_2 - \tfrac{1}{5}\sqrt{14}\, T^3_{222}] = \sum_{i,j,k} |p_i||p_j||p_k|/(\sqrt{s})^3 (\hat{p}_i \times \hat{p}_j \cdot \hat{p}_k)^2 ,$$

where $\hat{p}_i$ is a unit vector along the momentum p_i of particle i.

are very similar to those involved in the calculation of the total cross section. It seems very probable, therefore, that they should cancel in the same way.

In eq. (3.1), we are implicitly calculating the moments of the H_l for final states consisting of free quarks and gluons. We discuss the procedure in detail in subsect. 3.2. In reality, one must calculate the H_l for final states consisting of hadrons. We discuss this in subsect. 3.3. Our discussion there will require precise definition of a jet, and since this problem provides a useful introduction, we shall consider it first.

3.1. Jets

A typical quark or gluon jet is shown schematically in fig. 14. Such a jet would be indistinguishable from a single particle by a detector with energy resolution greater than ϵ and angular resolution greater than δ. (ϵ and δ are normalized so that a detector which only counts the total cross section and cannot distinguish any details of the final state has $\epsilon = \delta = 1$.) To order g^0 (g is the QCD coupling constant) the only diagram for production of two jets by a virtual photon is that of fig. 15. To order g^2, there are two types of diagram which lead to two-jet final states. Examples are given in figs. 16a, b. For the diagram of fig. 16a to contribute to the 2-jet cross section, either the gluon or quark must have an energy $\leqslant \epsilon E$, or they must be traveling in the same direction to within δ. If these conditions are not satisfied, then the detector will be able to tell that three, rather than two, particles were produced, and the event will be classified as a three-jet one. In order to regularize the calculation of diagrams such as those in fig. 16, one must assign the gluon a fictitious mass, μ. Then the probability corresponding to diagrams like fig. 16b will contain terms of the form $[\log \mu]^{P_\mu}$, $0 \leqslant P_\mu \leqslant 2$. Diagrams like fig. 16a will contain terms of the form $[\log \delta]^{P_\delta}\ [\log \epsilon]^{P_\epsilon}\ [\log \mu]^{P_\mu}$, $0 \leqslant P_\delta + P_\epsilon + P_\mu \leqslant 2$.

If δ and ϵ are both taken to be one, that is, if the detector is never able to distinguish a 'three-jet' event, so that it measures only the total cross section, then the KLN theorem guarantees that it will measure a finite cross section to any order in g^2.

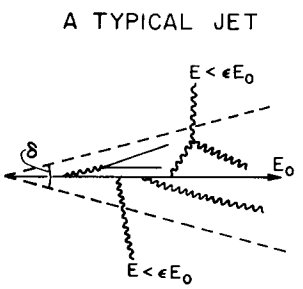

Fig. 14. Schematic form of a typical quark or gluon jet. Particles within the jet must either have an energy less than a fraction ϵ of the energy of the primary particle, or must travel at an angle less than δ with respect to it.

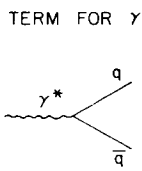

Fig. 15. The lowest order diagram for the process $\gamma^* \to q\bar{q}$.

Specifically, to order g^2, the terms in $[\log \mu]^p \mu$ in the loop and tree graphs will cancel, so long as $\delta = \epsilon = 1$. It turns out that the cancellation of μ-dependent terms occurs, at every order in g^2, even if $\delta, \epsilon \neq 1$ [25]. (This result was verified explicitly to $O(g^2)$ in ref. [2] and essentially to $O(g^4)$ in ref. [9].) This means that the cross section for production of two or three jets at $O(g^2)$ is free of divergences, as long as ϵ and δ are both finite. If either of ϵ and δ is set to zero, then a divergent cross section will be obtained. The cross section would be for production of, say, a quark, with no associated gluons. Since any quark produced will always radiate some gluons, such a cross section is not physically meaningful.

The cross section at $O(g^2)$ for inclusive production of a quark from a virtual photon is shown in fig. 17, as a function of the fractional energy x, of the quark. For the quark to have its maximum energy ($x = 1$), the kinematics of the process (see the appendix) require no gluons, of any energy, to have been produced. However, processes like that in fig. 16b can occur, and give rise to a divergent cross section just at $x = 1$. That is, they contribute terms to the differential cross section like $-c\delta(1 - x)$, where c is a positive constant which diverges when $\mu = 0$. The integral of $d\sigma/dx$ shown in fig. 17 over x from 0 to 1 is rendered finite by the presence of the δ function at $x = 1$ (to see this, one must first regularize by taking $\mu \neq 0$; the relevant formulas are given in sect. 4). This corresponds to the total cross section at $O(g^2)$, which is known to be finite from the KLN theorem.

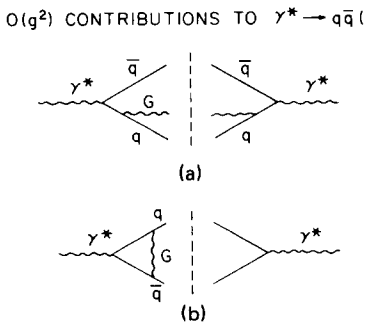

Fig. 16. Examples of terms at $O(g^2)$ in the amplitude squared for the process $\gamma^* \to q\bar{q}(G)$. The first diagram will contribute either to the two- or three-jet cross section, depending on the momentum of the gluon, while the second will contribute only to two-jet production.

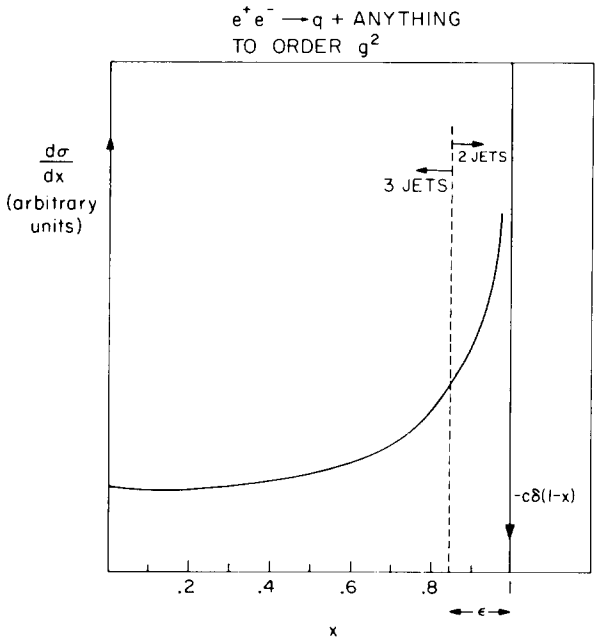

Fig. 17. The differential cross section for the process $e^+e^- \to q$ + anything calculated to order g^2, as a function of the fractional energy, x, of the quark. The final state is considered to contain two jets if $x > 1 - \epsilon$, and to contain three jets if the quark has $x < 1 - \epsilon$. Only the process $e^+e^- \to q\bar{q}G$ (fig. 16a) contributes to 3-jet production, but both $e^+e^- \to q\bar{q}G$ (fig. 16a) and $e^+e^- \to q\bar{q}$ (figs. 15 and 16b) can give rise to two-jet final states. The infrared divergences in the cross sections for these processes cancel when the total two-jet production cross section is computed.

Let us now introduce the energy resolution ϵ. Quarks with $x > 1 - \epsilon$ will be assumed to belong to 2-jet events, while those with $\epsilon < x < 1 - \epsilon$ will be distinguished as belonging to three-jet events. If ϵ is taken to be 0, then all of the sharply rising 3-particle production cross section will be included in the 3-jet cross section, while the negative delta function associated with the two-particle production process will not be included. Clearly, with this choice for ϵ, the '3-jet' production cross section will be infinite. As discussed above, however, such a choice for ϵ is not physically sensible. If a finite value for ϵ is chosen, then the two- and three-jet configurations will be defined as indicated in fig. 17, and their cross sections will be separately finite.

The above discussion is incomplete because it ignores divergences associated with collinear quarks and gluons. In fact, one must only include in the 3-jet sample events in which all the quarks and gluons are separated by angles greater than δ. (Only if the quarks are taken to be massless does the collinear quark and gluon configuration lead to a divergence but collinear gluon pairs inevitably give diver-

gent contributions.) Instead of making cuts in both angle and energy, one may cut only in k_T or H_2 in order to isolate three-jet events.

The conclusion of this discussion is, therefore, that, while it is sensible to ask for the total cross section to any order in g^2, it is not sensible to ask for the total probability that, say, two jets are produced to that order, unless one has specified reasonable values for the resolution parameters ϵ and δ which delineate two- and three-jet production.

3.2. Moments of the H_l for final states of quarks and gluons

Now let us return to the evaluation of the $\langle H_l^P \rangle$. We shall begin by ignoring the fact that the quarks and gluons produced by the virtual photon will eventually be combined into hadrons. At first we simply calculate $\langle H_l^P \rangle$ for final states consisting of free quarks and gluons. To do this, we must evaluate the expression (3.1), where the integral is over all possible kinematic configurations for the final state, and in H_l a sum is done over all the particles in each final-state configuration. The numerator of (3.1) may be written as

$$\sum_{\text{diagrams}} \int \frac{d\sigma}{dx_1 \ldots dx_n} H_l^P \, dx_1 \ldots dx_n \, . \tag{3.2}$$

First consider evaluating this for H_0. Clearly, in every kinematic configuration, H_0 will simply be 1. Then (3.2) reduces to an expression for the total cross section, which is known to be finite. Now consider evaluating $\langle H_2 \rangle$. For the result to be sensible, it must be independent of the gluon mass (infrared cut-off) μ, when the integral over all kinematic configurations ($\delta = \epsilon = 1$) is done. To order g^2, one may construct H_2 explicitly, and check that the integral (3.2) is independent of μ. This is done in sect. 4. The integral is found to divide into two parts. The first is identical to the total cross section, while the second contains a weighting function which vanishes in all kinematic configurations for which divergences occur in the differential cross section *. Note that the particularly simple form for H_2 in the case of 3-particle final states (see eq. (4.9)) will not persist in higher orders: only at $O(g^2)$ is the divergent term encountered in the calculation of the moments of H_2 exactly the total cross section.

Perturbation theory can only be valid if successive terms in the perturbation expansion are, on average, progressively smaller. In QED, the breakdown of the perturbation expansion in the infrared region is well-known. The same phenomenon occurs in QCD. If the main contribution to the expectation value of an observable comes from a kinematic region close to an infrared divergence, then its value deduced from perturbation theory must be suspect. The parameter which governs the applicability of perturbation theory to the process $e^+e^- \to q\bar{q}G$ is presumably

* Divergences in differential cross sections are typically of the form $[\log k_\perp]^P/k_\perp$, where $k_\perp$ is the transverse momentum between two of the final quarks or gluons. Cancellations occur between processes in which $k_\perp$ is strictly zero and those in which it is small. The difference of the H_l between these two configurations is $O(k_\perp^2)$, and so gives no infrared divergences when the integral over $k_\perp$ is performed.

$\alpha_s(s)/(1-x_1)(1-x_2)$, where $x_1(x_2)$ are the fractional energies of the $q(\bar{q})$ and $\alpha_s(s)$ is the QCD (running) coupling constant evaluated at the c.m. energy under consideration. As $x_1, x_2 \to 1$, this parameter becomes large and the $q\bar{q}G$ final state becomes indistinguishable from $q\bar{q}$ with $x_1 = x_2 = 1$. When the parameter is large, higher orders in the perturbation expansion will be no less important than the low orders under consideration. The results for the total cross section and (as we shall argue below) for the moments of the H_l are finite at each order in the perturbation expansion. However, the actual finite numerical values may be modified significantly by the inclusion of higher orders. It is believed that this phenomenon does not occur for the total cross section. This is exemplified by the $O(g^2)$ contribution to the total cross section, which is smaller than the lowest-order term by a factor of $\alpha_s(s)/\pi$. Some moments of the cross section will, while remaining finite, probe kinematic regions close to infrared divergences to a greater extent than the total cross section. These moments should remain finite, but may well receive numerically important contributions from higher-order effects. This phenomenon occurs for some of the high-order moments of, for example, H_2, in the process $e^+e^- \to q\bar{q}G$ (see subsect 4.4).

Cancellations of μ-dependent terms in the total cross section come when a tree graph at one order in g^2 gives rise to (almost) the same final-state kinematic configuration as loop graphs of the same order. So long as an observable does not distinguish between the canceling graphs (that is, it gives them all the same weight in an integral of the type (3.2)), the integrals for its moments should experience the same cancellations of μ-dependent terms as occur in the integral for the total cross section. The H_l have this property. The decomposition of the integral for $\langle H_2 \rangle$ mentioned above is one consequence. In a divergent kinematic configuration, different graphs are treated the same, just as in the calculation of the total cross section.

Any variable which is proportional to the energies of the final particles will have the same value for kinematic configurations which differ simply by the addition of a gluon of indefinitely low energy. However, one must also demand that the variables do not distinguish between configurations containing a single particle and two (or more) nearly collinear particles with the same total energy [5,6]. The H_l fulfill both requirements. It, therefore, seems very reasonable to expect that the infrared divergences associated with the calculation of their moments to every order in g^2 will cancel in the manner described above. The same cancellation should occur for the moments of 'spherocity' but not for those of 'sphericity', since the latter is not linear in the momenta of nearly collinear final particles ★.

★

$$\text{spherocity} = \left(\frac{4}{\pi}\right)^2 \min\left[\sum_i |p_\perp^i| / \sum_i |p_i|\right]^2,$$

$$\text{sphericity} = \tfrac{3}{2} \min\left[\sum_i |p_\perp^i|^2 / \sum_i |p_i|^2\right],$$

where the $p_\perp^i$ are the momenta of the particles i transverse to the jet axis which is defined by demanding that the values of the variables be minimal. See ref. [6] for discussions of other variables.

The linearity in momenta of the H_l is advantageous at the hadron as well as the quark and gluon level. For example, the values of the H_l are essentially unaffected by decays with small internal transverse momenta; they have the same value whether the parent particles or their decay products are measured.

3.3. Moments of the H_l for hadronic final states

Further problems appear when one attempts to calculate the moments of the H_l (or 'spherocity', 'thrust' and so on) for genuine processes involving the production of hadrons rather than of quarks and gluons. For example, at $O(g^2)$, one must decide whether a quark and soft gluon will fragment into hadrons as a quark or like a quark and a gluon. This means that in order to estimate the production of hadrons, one must divide up the $O(g^2)$ cross section into 2- and 3-jets parts by using sensible values for the parameters δ and ϵ which distinguish the two. Then, in the two-jet region, we assume that it is a two-quark state which fragments to hadrons, while in the three-jet region, the gluon as well as the two quarks are taken to fragment separately into hadrons.

It is as if the formation of the final hadron state provides a measuring apparatus with finite resolution for the subprocess involving quarks and gluons. The configuration of the final hadron state is unaffected by small changes in the energies and momenta of the quarks and gluon which generate them. Only a large deviation in the energies of the quarks from those of the process $e^+e^- \to q\bar{q}$ is reflected by the appearance of three hadron jets in the final state; smaller deviations are beyond the 'resolution' of the hadrons in the final state. The 'resolution' of the hadrons will be determined by the model for their production by the 'fragmentation' of quarks and gluons. To be exact, this fragmentation should be taken to depend on the total c.m. energy, $\sqrt{s}$. Such s dependence, which involves mixing between quark and gluon fragmentation functions, is believed to be given by simple renormalization group equations. However, the necessary formalism has so far been developed only for single-hadron inclusive distributions [10] *. In order to make realistic estimates for the moments of H_l, we require a model for the generation of a complete hadronic final state. For this purpose, we use the model developed by Field and Feynman [18], despite the fact that it exhibits exact scaling at asymptotic energies. Fortunately, the model turned out to be adequate, and our final results are essentially independent of the arbitrary cut-offs (ϵ, δ) between two- and three-jet events.

3.4. The infrared instability of $F(x)$

From the formula (2.20), one finds that the coefficient of the $\delta(1-x)$ term in $F(x)$ is $2\Sigma_i E_i^2/s$, which is not infrared stable against collinear divergences. Since

* The s dependence of the fragmentation is partly accounted for by our inclusion of $O(g^2)$ processes. The remaining s dependence has contributions both at $O(g^2)$ (whose form depends on the separation of two- and three-jet events) and from higher-order processes.

$\int_{-1}^{1} F(x)\,dx = 2$, this divergent contribution must be absorbed by a compensating divergence at other values of x. The presence of divergences in $F(x)$ is to be expected, since events containing two particles which are arbitrarily close in angle will be weighted differently in the computation of $F(x)$ from those containing a single particle which carries the sum of their energies, because the two particles cannot pass through the same point detector. It is clear that to the lowest order in g^2 for any process, there will be no infrared divergences in $F(x)$, and that in the next order, divergences will appear only at those values of x for which the lowest-order $F(x)$ is non-zero (e.g., for $e^+e^- \to q\bar{q}(G)$ to $O(g^2)$, divergences appear only at $x = \pm 1$). In higher orders, divergences will occur at all values of x.

The energy correlation $F_2(\sigma_1, \sigma_2)$ defined by eq. (2.22) is formally infrared stable so long as the $|\sigma_i|$ are non-zero *. However, as the angular size δ of the detectors tends to zero, $F_2(\sigma_1, \sigma_2)$ will become infrared unstable. For final states consisting of free quarks and gluons, $F_2(\sigma_1, \sigma_2)$ might serve as a satisfactory measure. However, for genuine hadronic final states, the formation of the final state from quarks and gluons introduces a finite angular resolution, whose size cannot at present be deduced directly from QCD. Unless δ is very large, the unknown resolution associated with the formation of hadrons will be the most important quantity in determining F_2, thereby rendering it useless. If one chooses a large value of δ, very little information will be obtained unless the integration over the areas $|\sigma_i|$ is performed using a non-trivial weight function, in which case essentially the H_l will be obtained.

4. Results for idealized jets

In this section, we present our results on the cross sections and H_l moments for the production of free quarks and gluons by a virtual photon. Sect. 5 discusses the results obtained using a realistic model for the fragmentation of the quarks and gluons into hadrons.

4.1 $e^+e^- \to q\bar{q}(G)$

We consider first the cross section for the process $e^+e^- \to q\bar{q}G$, which proceeds (in lowest order) through the diagrams of fig. 18. Defining (see the appendix)

$$|\boldsymbol{p}_q| = \tfrac{1}{2}x_1\sqrt{s}\,,$$
$$|\boldsymbol{p}_{\bar{q}}| = \tfrac{1}{2}x_2\sqrt{s}\,, \qquad (4.1)$$
$$|\boldsymbol{p}_G| = \tfrac{1}{2}x_3\sqrt{s}\,,$$

* Note that although $\langle F_2(\sigma_1, \sigma_2)\rangle$ can be obtained from $\langle F(x)\rangle$ by smearing in x, the distributions of events in $F(x)$ and $F_2(\sigma_1, \sigma_2)$ are not related in any simple way.

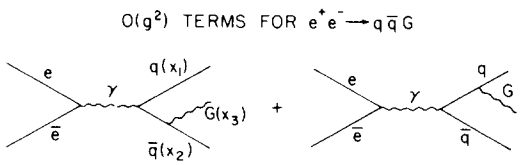

Fig. 18. The lowest-order diagrams for the process $e^+e^- \to q\bar{q}G$.

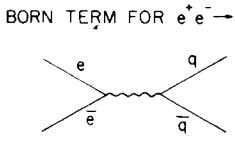

Fig. 19. The lowest-order diagram for the process $e^+e^- \to q\bar{q}$.

where $\sqrt{s}$ is the total c.m. energy (the virtual photon mass), and taking a finitè gluon mass μ as a regularizer, one finds that the differential cross section for this process (summed over the colors of the final particles) is given by *

$$\frac{d\sigma}{dx_1\,dx_2} = \sigma_0 \frac{2\alpha_s}{3\pi} \frac{1}{(1-x_1)(1-x_2)}$$

$$\times \left\{ x_1^2 + x_2^2 + \frac{\mu^2}{s}\left[2(x_1+x_2) - \left(\frac{(1-x_1)^2+(1-x_2)^2}{(1-x_1)(1-x_2)}\right)\right] + \frac{2\mu^4}{s^2}\right\}. \qquad (4.2)$$

Here σ_0 is the lowest-order cross section for the process $e^+e^- \to q\bar{q}$ shown in fig. 19, and $\alpha_s = g^2/4\pi$ is the QCD coupling constant.

The cross section for $e^+e^- \to q\bar{q}$ at order g^2 resulting from the interference of the diagrams of fig. 20 with the lowest-order diagram (fig. 19.) is [2]

$$\frac{d\sigma}{dx_1\,dx_2} = \sigma_0 \frac{4\alpha_s}{3\pi}\,\delta(1-x_1)\,\delta(1-x_2)\left\{-\tfrac{1}{2}\log^2\frac{s}{\mu^2} + \tfrac{3}{2}\log\frac{s}{\mu^2} - \tfrac{7}{4} + \tfrac{1}{6}\pi^2\right\}. \qquad (4.3)$$

(Note that each 'wave-function renormalization' diagram occurs only once in the product of figs. 19 and 20.)

Integrating the differential cross sections (4.2) and (4.3) over the final particles' phase space, one finds that the total cross section for e^+e^- annihilation into free

* Note that, for simplicity, we always take the initial e^+ and e^- to be unpolarized.

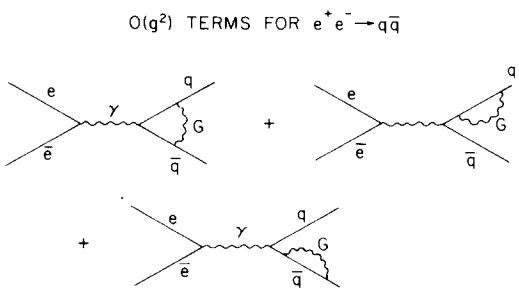

Fig. 20. Contributions to the process $e^+e^- \to q\bar{q}$ at order g^2.

quarks and gluons to order g^2 is finite and independent of μ. It is given by [26]

$$\sigma = \sigma_0 \left(1 + \frac{\alpha_s}{\pi} + O(g^4)\right). \tag{4.4}$$

In the case of this total cross section, there are good arguments based on the renormalization group [11] which suggest that the relevant coupling constant in (4.4) is $\alpha_s(s)$ given by *

$$\alpha_s(s) \simeq \frac{12\pi}{(33 - 2F)\log(s/\Lambda^2)}. \tag{4.5}$$

(We take $F = 4$ and $\Lambda = 0.5$ GeV, but our results are not sensitive to these choices.) We assume that the α_s appearing in the differential cross sections (4.2) and (4.3) should also be the $\alpha_s(s)$ given in eq. (4.5).

4.2. Decays of heavy quark resonances

It seems reasonable to guess that the decay of a heavy $Q\bar{Q}$ resonance ζ with $J^P = 1^-$ into hadrons will be initiated by its decay to three gluons, as in fig. 21 [4]. We assume that the quarks Q and $\bar{Q}$ behave as if free at the time of the annihilation. Then the differential cross section for the decay $\zeta \to GGG$ is

$$\frac{1}{\sigma}\frac{d\sigma}{dx_1 dx_2} = \frac{1}{(\pi^2 - 9)}\left[\frac{(1-x_1)^2}{(x_2x_3)^2} + \frac{(1-x_2)^2}{(x_1x_3)^2} + \frac{(1-x_3)^2}{(x_1x_2)^2}\right], \tag{4.6}$$

where $x_3 = 2 - x_1 - x_2$. The cross section (4.6) is identical to that for the decay of positronium into three photons [13]. Note that it is finite throughout the physical region. (It is the only mechanism for $\zeta \to GGG$ at $O(g^6)$, so that if the total cross

* Note, however, that the Λ^2 which appears in this formula may well differ considerable from the values deduced from measurements of other processes, or from the 'true' Λ^2 [12].

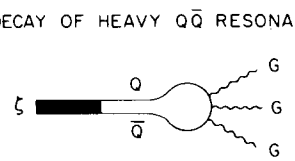

Fig. 21. The lowest-order diagram for the decay of a heavy vector meson (ζ) containing a pair of heavy quarks (Q) into three gluons.

section for $\zeta \to \mathrm{GGG}$ at $O(g^6)$ is to be finite, then so must the cross section for the process of fig. 21 be.)

The process $\zeta \to \gamma^* \to q\bar{q}$ illustrated in fig. 22 may also contribute to the hadronic decay of the ζ. The ratio of the total decay rates of the ζ due to the diagrams of figs. 22 and 21 may be estimated as (e_Q is the charge of the Q quark)

$$B \equiv \frac{\Gamma(\zeta \to \gamma^* \to q\bar{q})}{\Gamma(\zeta \to \mathrm{GGG})} \simeq \frac{81\pi}{10(\pi^2 - 9)} \frac{\alpha^2 e_Q^2}{[\alpha_s(m_\zeta^2)]^3} \frac{\sigma(e^+e^- \to \text{hadrons})}{\sigma(e^+e^- \to \mu^+\mu^-)} \quad (s = m_\zeta^2) , \tag{4.7}$$

where we have assumed (without much justification) that the coupling constant relevant to the process of fig. 21 is $\alpha_s(m_\zeta^2)$. The sensitivity of eq. (4.7) to the value of α_s makes an estimate of B for the Υ difficult. It seems likely, however, that

$$0.1 \lesssim B_\Upsilon \lesssim 1 . \tag{4.8}$$

A number of ζ decays other than to GGG and $q\bar{q}$ may also be considered. The main ones of interest are

$$\zeta(2^3S_1) \to \gamma\underbrace{\zeta(1^3P_2)}_{\mathrm{GG}} , \qquad \zeta \to \mathrm{G}\,\underbrace{(\text{glueball})}_{\mathrm{GG}} .$$

The first of these processes might be interesting [14] because the gluon jets will have higher energies than in $\zeta \to \mathrm{GGG}$, and so presumably will be better collimated. The

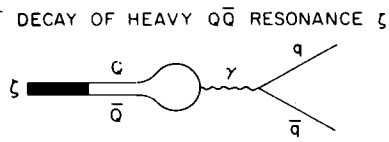

Fig. 22. The lowest-order diagram for the electromagnetic decay of a heavy vector meson (ζ) containing a pair of heavy quarks (Q) into a pair of light quarks (q).

decay

$$\zeta \to \text{G (glueball)} \longrightarrow \text{GG}$$

should give somewhat different gluon energy and angular distributions than $\zeta \to \text{GGG}$, but the effect is difficult to estimate reliably.

4.3. The H_l moments

For a 2-jet event, $H_2 = 1$. For a three-jet event (see the appendix for the definitions of ϕ_{ij})

$$\begin{aligned} H_2 &= \tfrac{1}{4} \sum_m |\, \textstyle\sum x_i Y_2^m(\Omega_i)|^2 \\ &= \tfrac{1}{4}[3(x_1 + x_2\cos^2\phi_{12} + x_3\cos^2\phi_{13}) - 2]^2 \\ &+ 3x_2^2 \sin^2\phi_{12}[\cos\phi_{12} - \cos\phi_{13}]^2 \\ &+ \tfrac{3}{4}[x_2\sin^2\phi_{12} + x_3\sin^2\phi_{13}]^2 \\ &= \tfrac{1}{4}[x_1^2 + x_2^2 + x_3^2 + 2x_1x_2P_2(\cos\phi_{12}) \\ &+ 2x_2x_3P_2(\cos\phi_{23}) + 2x_3x_1P_2(\cos\phi_{31})] \\ &= 1 - \frac{6(1-x_1)(1-x_2)(1-x_3)}{x_1x_2x_3} \,. \end{aligned} \tag{4.9}$$

This formula realizes the claim made in sect. 3 that H_2 may be divided into a constant term and a term which damps the divergence in the 3-jet differential cross section (4.2).

To evaluate the moments of H_2 for the process $e^+e^- \to q\bar{q}G$, we write

$$\langle H_2^P \rangle = \frac{\int d\sigma + \int (H_2^P - 1)\, d\sigma}{\int d\sigma} \,. \tag{4.10}$$

The $\int d\sigma$ is given to $O(g^2)$ by eq. (4.4). In the case $P = 1$, it is possible to evaluate $\int (H_2 - 1)\, d\sigma$ in closed form. Including the contribution from 2-jet events at $O(g^0)$, the final result for $\langle H_2 \rangle$ to $O(g^2)$ is *

* Evaluation of $\langle H_l \rangle$ for three-particle final states requires integration over the two phase-space variables x_1 and x_2. The integrals over x_2 may always be done in terms of elementary functions, but the integration over x_1 always involves dilogarithms [15]. Integration by parts reduces the dilogarithm integrals to the canonical forms [16]

$$\int_1^0 \frac{\log(1+x)}{x}\, dx = \text{Li}_2(-1) = -\tfrac{1}{12}\pi^2 \,, \qquad \text{or} \qquad \int_1^0 \frac{\log(1-x)}{x}\, dx = \text{Li}_2(1) = \tfrac{1}{6}\pi^2 \,.$$

$$\langle H_2 \rangle = \left[1 + \frac{2\alpha_s}{3\pi}(33 - 4\pi^2) + \frac{\alpha_s}{\pi}\right] \Big/ \left[1 + \frac{\alpha_s}{\pi}\right]$$

$$= 1 + \frac{2\alpha_s}{3\pi}(33 - 4\pi^2) + O(\alpha_s^2) \tag{4.11}$$

$$\simeq 1 - 1.4\,\alpha_s$$

$$\simeq 1 - 2.0/\log(s/\Lambda^2)\,.$$

The coefficients (c) of α_s for some higher moments of H_2 are given in table 2. Values of the moments for various c.m. energies ($\sqrt{s}$) are also given there, using $\Lambda = 0.5$ GeV. Note the negative values obtained for some of the higher moments of H_2 at low $\sqrt{s}$. These unphysical results are signals of the breakdown of perturbation theory. As higher moments of H_2 are evaluated, so the region in the differential cross section closer and closer to the 2-jet limit is probed. However, as discussed in subsect. 3.2, the lowest order in the perturbation expansion is no longer a good estimate of the differential cross section in this region. Results which depend critically on the behavior of the $e^+e^- \to q\bar{q}G$ cross section for kinematic configurations close to that for $e^+e^- \to q\bar{q}$ cannot, therefore, be determined reliably from an $O(g^2)$ estimate. These difficulties in practice effect only the high-order moments of the H_l for the process $e^+e^- \to q\bar{q}G$ at low s. The form of $(1/\sigma)\,d\sigma/dH_l$ for hadrons resulting from this process will be entirely unaffected by these problems (see sect. 5).

The first moment (mean value) of H_2 for the process $\zeta \to GGG$ is found to be given by

$$\langle H_2 \rangle = \frac{103\pi^2 - 1008}{16(\pi^2 - 9)} \simeq 0.616\,. \tag{4.12}$$

Higher moments of H_2 for this process are given in table 3. The decrease of $\langle H_2^P \rangle$

Table 2
Moments of H_2 for the process $e^+e^- \to q\bar{q}(G)$ (the sum of $e^+e^- \to q\bar{q}$ and $e^+e^- \to q\bar{q}G$ calculated through $O(g^2)$)

		$\langle H_2^P \rangle = 1 + c\alpha_s(s)$			
P	c	$\sqrt{s} = 5$ GeV	$\sqrt{s} = 10$ GeV	$\sqrt{s} = 20$ GeV	$\sqrt{s} \to \infty$
1	−1.4	0.54	0.65	0.72	1
2	−2.3	0.25	0.42	0.53	1
3	−3.1	−0.01	0.22	0.37	1
4	−3.7	−0.21	0.07	0.24	1
5	−4.3	−0.40	−0.08	0.13	1

The negative values of $\langle H_2 \rangle$, in some cases, are unphysical, and signal the inaccuracy of the $O(g^2)$ terms in the perturbation series close to an infrared divergence. As the c.m. energy ($\sqrt{s}$) increases, the $e^+e^- \to q\bar{q}$ result $H_2 = 1$ is slowly attained.

with P in this case is a consequence of the approximate flatness of $(1/\sigma)\,d\sigma/dH_2$ for $\zeta \to GGG$. ($\langle H_2^P \rangle$ for $\zeta \to GGG$ can never be negative, since in this case $(1/\sigma)\,d\sigma/dH_2 \geqslant 0$ everywhere.)

In general, $0 \leqslant H_2 \leqslant 1$. For a three-jet event, however, the value of H_2 is more tightly constrained. The form (4.9) for H_2 is easily seen to be minimized for $x_1 = x_2 = x_3 = \frac{2}{3}$ (the event is most spherical in this configuration), at which point $H_2 = \frac{1}{4}$. It is maximized in the collinear ('two-jet') configuration, for which $H_2 = 1$. For a three-particle final state, therefore

$$\tfrac{1}{4} \leqslant H_2 \leqslant 1\,. \tag{4.13}$$

In contrast, a two-jet event gives $H_2 = 1$, while a spherical ('phase-space') event has $H_2 = 0$.

For a two-jet event, $H_3 = 0$. For a three-jet event

$$H_3 = \tfrac{1}{4} \sum_m |\sum x_i Y_3^m(\Omega_i)|^2 = \tfrac{1}{4} \sum_{i,j} x_i x_j P_3(\cos\phi_{ij})$$

$$= 40\left[\frac{(1-x_1)(1-x_2)(1-x_3)}{x_1 x_2 x_3}\right]^2 . \tag{4.14}$$

The integral $\int H_3\,d\sigma$ contains no infrared divergences since the weight of the kinematic configurations close to the 2-jet one which lead to divergences is zero. For the process $e^+e^- \to q\bar{q}G$, we find

$$\langle H_3 \rangle = \tfrac{1}{3}(1980 - 200\pi^2)\,\frac{2\alpha_s}{3\pi} \simeq 2.03 \times 2\alpha s/3\pi\,, \tag{4.15}$$

while for $\zeta \to GGG$

$$\langle H_3 \rangle = \frac{15(339\pi^2 - 3344)}{144(\pi^2 - 9)} \simeq 0.215\,. \tag{4.16}$$

Notice that $H_3 = 0$ both for a spherical and for a 2-jet event. Only for events with non-trivial structure is it non-zero. Tables 4 and 5 give the values of some higher moments of H_3 for $e^+e^- \to q\bar{q}G$ and for $\zeta \to GGG$.

Table 3
Moments of H_2 for the process $e^+e^- \to \zeta \to GGG$, where ζ is a heavy $Q\bar{Q}$ resonance

P	$\langle H_2^P \rangle$
1	0.62
2	0.43
3	0.32
4	0.25
5	0.21

Table 4
Moments of H_3 for the process $e^+e^- \to q\bar{q}(G)$ (the sum of $e^+e^- \to q\bar{q}$ and $e^+e^- \to q\bar{q}G$ calculated through $O(g^2)$)

		$\langle H_3^P \rangle = c\alpha_s(s)$			
P	c	$\sqrt{s}$ = 5 GeV	$\sqrt{s}$ = 10 GeV	$\sqrt{s}$ = 20 GeV	$\sqrt{s} \to \infty$
1	0.43	0.14	0.11	0.09	0
2	0.11	0.04	0.03	0.023	0
3	0.043	0.014	0.011	0.009	0
4	0.020	0.006	0.005	0.004	0
5	0.010	0.003	0.002	0.002	0

For any three-jet process

$$0 \leqslant H_3 \leqslant \tfrac{5}{8} . \tag{4.17}$$

The maximum value is attained when $x_1 = x_2 = x_3 = \frac{2}{3}$ (the event is most 'spiky' in this configuration).

For a 2-jet event, $H_4 = 1$. There is no simple formula for H_4 in a three-jet event *, although it can be shown that in this case

$$1 \geqslant H_4 \geqslant \tfrac{9}{64} \simeq 0.1406 \tag{4.18}$$

where the minimum value is realized for $x_1 = x_2 = x_3 = \frac{2}{3}$. One finds

$$\langle H_4 \rangle_{e^+e^- \to q\bar{q}(G)} \simeq 1 - 2.1\ \alpha_s(s) , \tag{4.19}$$

$$\langle H_4 \rangle_{\xi \to GGG} \simeq 0.50 ,$$

* In fact, one finds

$$H_4 = 1 - \frac{5(1-x_1)(1-x_2)(1-x_3)}{(x_1x_2x_3)^3} \{4[((1-x_1)x_1)^2 + ((1-x_2)x_2)^2]$$
$$+ (1-x_1)(1-x_2)[2(1-x_1)(19x_1^2 - 42x_1 + 28) + (x_1 \leftrightarrow x_2)$$
$$+ x_1x_2(25(x_1^2 + x_2^2) + 50x_1x_2 - 151(x_1 + x_2) + 252) - 56] \} .$$

This general pattern persists, and, for example,

$$H_5 = \frac{7(1-x_1)^2(1-x_2)^2(1-x_3)^2}{(x_1x_2x_3)^4} \{43[(1-x_1)^2x_1^2 + (1-x_2)^2x_2^2]$$
$$+ (1-x_1)(1-x_2)[(1-x_1)(101x_1^2 - 288x_1 + 288) + (x_1 \leftrightarrow x_2)$$
$$+ x_1x_2(43(x_1^2 + x_2^2) + 86x_1x_2 - 331(x_1 + x_2) + 720) - 288] \} .$$

Table 5
Moments of H_3 for the process $e^+e^- \to \zeta \to GGG$, where ζ is a heavy $Q\bar{Q}$ resonance

P	$\langle H_3 \rangle$
1	0.215
2	0.081
3	0.036
4	0.018
5	0.009

where by $e^+e^- \to q\bar{q}(G)$ we mean the sum of the processes $e^+e^- \to q\bar{q}$ and $e^+e^- \to q\bar{q}G$.

4.4. Differential cross sections in the H_l

The differential cross sections $(1/\sigma_{tot})\, d\sigma/dH_l$ for the processes $e^+e^- \to q\bar{q}(G)$ and $\zeta \to GGG$ are shown in fig. 23 for $l = 2, 3$ and 4. Note that (apart from the $\sqrt{s}$ dependence of $\alpha_s(s)$), all these results are exactly scale invariant (do not depend on the value of $\sqrt{s}$). (The cross section for $e^+e^- \to q\bar{q}G$ is proportional to $\alpha_s(s)$. $\sqrt{s}$ = 20 GeV was chosen to evaluate $\alpha_s(s)$ for fig. 23. Results for other values of $\sqrt{s}$ may be obtained by a trivial rescaling.) The differential cross sections for $e^+e^- \to q\bar{q}G$ shown in fig. 23 exhibit infrared divergences, but as discussed above, these divergences cancel when the moments of the H_l are evaluated. Notice the sharp cut-offs in the differential cross sections at the boundaries of the physical region for three-jet processes ($H_2 = 0.25, H_3 = 0.625, H_4 \simeq 0.1046$).

As will be discussed in sect. 5, the fragmentation of the quarks and gluons into hadrons serves to make considerable modifications to the $(1/\sigma)\, d\sigma/dH_l$. At very high energies, however, such modifications become less important, and at asymptotic energies, the free quark and gluon results of fig. 23 are regained.

We have calculated only to order g^2. In higher orders, processes in which more than three jets are produced will occur, and the two- and three-jet production cross sections will be modified. As discussed above, these higher-order effects are clearly important for those moments of the H_l which probe close to the region of infrared divergence; in some cases, they are even necessary to obtain positive results. Events involving more than three jets will also undoubtedly populate ranges of the H_l outside those allowed for three-jet events by kinematics. Except in these circumstances, we expect $O(g^4)$ and higher corrections to be small.

4.5. Production of heavy quark and lepton pairs

The production and weak decay of pairs of heavy mesons (D, B, ...) carrying new flavors will give rise to events whose shapes are distinct from those of the two- and

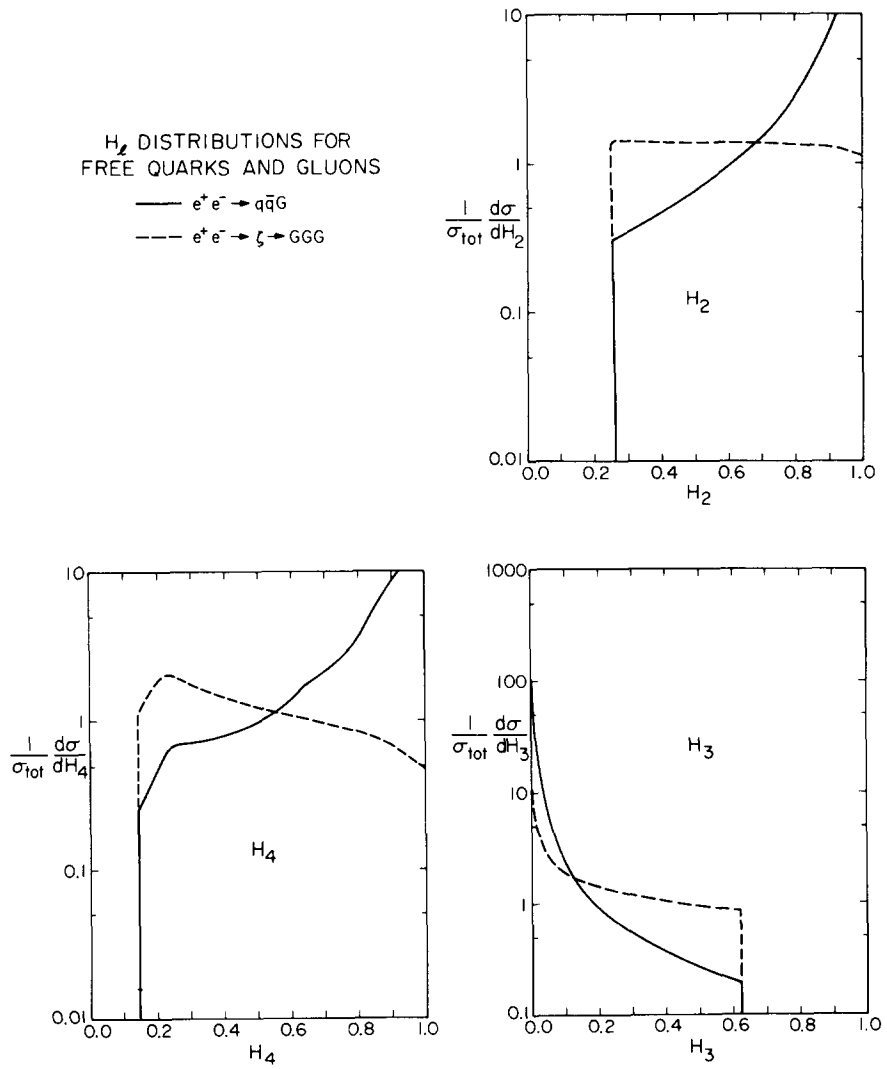

Fig. 23. The distributions in H_2, H_3 and H_4 for the processes $e^+e^- \to q\bar{q}G$ and $e^+e^- \to \zeta \to GGG$. $e^+e^- \to q\bar{q}$ gives $H_2 = 1$, $H_3 = 0$ and $H_4 = 1$. The distributions for $e^+e^- \to \zeta \to GGG$ are normalized to give unit total cross section. Of course, $e^+e^- \to q\bar{q}G$ yields an infinite total cross section, due to its divergence at $H_2 \to 1$ ($H_3 \to 0$, $H_4 \to 1$). When added to the cross section for $e^+e^- \to q\bar{q}$ calculated through $O(g^2)$, it gives a finite total cross section of $(1 + \alpha_s(s)/\pi)\,\sigma_0$ for the complete process $e^+e^- \to q\bar{q}(G)$. The curves in this figure have been calculated using $\sqrt{s} = 20$ GeV. Results for other values of $\sqrt{s}$ may be obtained by a trivial rescaling.

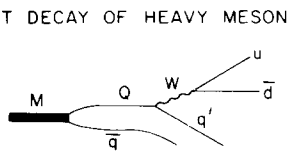

Fig. 24. Diagram for the weak decay of a heavy meson (M) through the decay of the heavy quark (Q) into three light quarks.

three-jet configurations discussed above. Three basic mechanisms for the weak decay of a heavy meson may be considered. The first, illustrated in fig. 24, involves the standard weak decay of the heavy quark Q into $q'u\bar{d}$. If a V–A (Qq') coupling is assumed, then the differential cross section for the decay in the fractional energies

$$x_1 = \frac{2E_u}{E_Q}\,,\; x_2 = \frac{2E_{\bar{d}}}{E_Q}\,,\; x_3 = \frac{2E_{q'}}{E_Q}$$

is

$$\begin{aligned}\frac{1}{\sigma}\frac{d\sigma}{dx_1\,dx_2} &= 12(2 - x_1 - x_2)(x_1 + x_2 - 1)\\ &= 12x_3(1 - x_3)\,,\\ \frac{1}{\sigma}\frac{d\sigma}{dx_1} &= 2x_1^2(3 - 2x_1)\,,\end{aligned} \tag{4.20}$$

just as in muon decay. The second mechanism, shown in fig. 25, involves the process $Q \to qG$ *. Note that in these first two mechanisms for heavy meson decay, we have considered only the weak decay of the heavy quark Q. The 'spectator' quark $\bar{q}$ will carry only a small fraction of the energy of the decaying meson, and so will not usually generate a jet. A third mechanism for heavy meson decay may also envisaged. It is illustrated in fig. 26, and involves the exchange of a W between the heavy quark Q and the 'spectator' $\bar{q}$. The importance of this third mechanism in strange particle decays is presently unknown; it is probably slightly more effective than the mechanism of fig. 24.

* The importance of such a mechanism is governed by the difference of the masses of the possible quarks in the loop. It may well be dominant in strange particle decays, but is probably unimportant in charm particle decays, since it is inevitably suppressed by $\sin\theta_c$ relative to the processes of figs. 24 and 26, and leads to non-strange final states in D meson decay. It could, therefore, account for the 'non-leptonic enhancement' observed in strange, but not charm, particle decays. In addition to the process of fig. 25, $Q\bar{q}$ mesons might decay to GG by exchanging a W just before the annihilation of the Q and $\bar{q}$. This would be suppressed relative to $Q \to qG$ by α_s, and is therefore probably safely ignored.

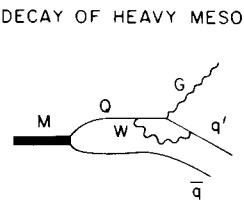

Fig. 25. Diagram for the weak decay of a heavy meson (M) through the decay of the heavy quark (Q) into a gluon and a light quark.

It is also possible that the mixing angles between heavy quarks are so arranged that the decay of a heavy quark involves many stages, each consisting of a decay to a quark of slightly lower mass. The cascades generated in this way would lead to values of the H_I very close to zero. The observation of jet structures resulting from the processes of figs. 24–26 would provide definitive evidence as to the mechanism of weak decays of possible very massive mesons carrying new flavors. The rates of these decay modes are modified by $O(\alpha_s)$ radiative corrections, but the energies of the extra final-state particles tend to be very small, so that they should not generate extra jets *. The radiative corrections to the first decay mode (fig. 24 may be computed from corrections to μ decay and from eq. (4.4) (color averaging decouples the radiative corrections to the produced quark pair). One finds that for a V–A coupling, $\Gamma \to \Gamma(1 - (\alpha_s/3\pi)(2\pi^2 - \frac{31}{2}))$, giving a 15% correction for $m_Q = 5$ GeV. For the second mechanism (fig. 25), the correction due to the $O(\alpha_s)$ process

$$Q \to q' G \hookrightarrow q\bar{q}$$

(the lowest-order vacuum polarization insertion to the gluon propagator must also

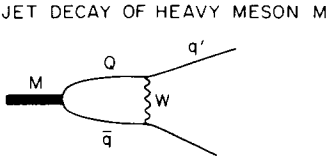

Fig. 26. Diagram for the weak decay of a heavy meson (M) in which the heavy quark (Q) undergoes a weak interaction with the spectator quark to produce a pair of light quarks.

* The renormalization group equation allows a summation of the leading logarithmic QCD corrections to weak decay rates to all orders in α_s. However, the structure of the final states is governed by emissions at large angles, which are best estimated by explicit $O(g^2)$ calculations.

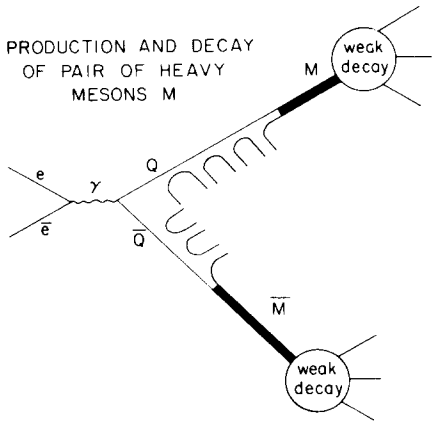

Fig. 27. Mechanism for the production and weak decay of heavy meson (M) pairs (containing heavy quarks Q) in e^+e^- annihilation.

be included, and renormalized off the gluon mass shell) simply contributes to replacing α_s by $\alpha_s(m_Q^2)$. Note that the $q\bar{q}$ pair in this process usually have a small invariant mass (hence small opening angle) and so act as one jet. The rate for the third decay mode (fig. 26) becomes roughly $\Gamma \to \Gamma(1 + \alpha_s/9\pi)$, about a 1% correction for m_Q = 5 GeV.

The basic mechanism for the inclusive production and decay of new heavy mesons (M) in e^+e^- annihilation is shown schematically in fig. 27. The hadronic shower associated with the primary vertex in fig. 27 will occur on time-scales of $\sim 10^{-24}$ s. The end-products of the showers will be M mesons with small momenta at least near the $M\bar{M}$ threshold, which will typically live $\sim 10^{-16}$ s before undergoing weak decays. The two sources of hadrons in these events act at very different times, and so will be effectively decoupled. At very high energies, the decay products of the M mesons will carry a negligible fraction of the total energy of the event; most will be radiated in the hadronic shower. At such energies, therefore, processes like fig. 28 will appear as two-jet events. Just above the threshold for $M\bar{M}$ production,

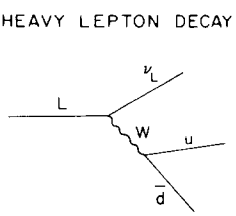

Fig. 28. Diagram for the weak decay of a (sequential) heavy lepton (L).

the events should, however, be very different from two-jet ones. We assume that no hadronic shower is generated, and that all the particles in the event come from the weak decay of the M meson. Since these have spin 0, there should be no correlation between the decays of the M and $\bar{\mathrm{M}}$ produced in a particular event. Making the approximation that the decays of M and $\bar{\mathrm{M}}$ are to free quarks (or gluons) and assuming independent decays at rest through the mechanism of fig. 24, we find that

$$\langle H_2\rangle = (\tfrac{119}{2} - 6\pi^2) \simeq 0.28\,, \qquad \langle H_3\rangle = 0.12\,, \qquad \langle H_4\rangle = 0.21\,. \tag{4.21}$$

The distributions $(1/\sigma)\,\mathrm{d}\sigma/\mathrm{d}H_l$ are shown in fig. 29. If the decay mechanisms of fig. 25 or fig. 26 are assumed, we find that

$$\begin{aligned} H_l &= \tfrac{1}{2}(P_l(\cos\xi) + 1)\,, \qquad (l \text{ even})\,, \\ &= 0\,, \qquad\qquad\qquad\quad (l \text{ odd})\,, \end{aligned} \tag{4.22}$$

where ξ is the angle between the pairs of final particles from the two mesons. The stationary points of the Legendre polynomials in eq. (4.22) are responsible for the spectacular peaks apparent in the H_l distributions for these events. The expression (4.22) for H_l yields

$$\begin{aligned} &\langle H_l\rangle = \tfrac{1}{2}\,, \quad (l \text{ even and } l \geqslant 2)\,, \\ &\langle H_l\rangle = 0\,, \quad (l \text{ odd})\,, \end{aligned} \tag{4.23}$$

upon integration over $\cos\xi$. Note that the independence of the decays of the two mesons causes the H_l for the complete process to be proportional to an average of the $\langle H_l\rangle$ for the two decays. In the notation of sect. 2, the $\langle H_l\rangle$ for the complete process become (for $l > 0$ and normalizing the densities $\rho_l(\Omega)$ so that their sum gives $H_0 = 1$)

$$\begin{aligned} \langle H_l\rangle &= \int \sum_m \Big| \int [\rho_1(\Omega)\, Y_l^m(\Omega) + \rho_2(\Omega)\, Y_l^m(R_\xi\Omega)]\, \mathrm{d}\Omega\Big|^2\, \mathrm{d}R_\xi \\ &= \tfrac{1}{4}\,(\langle H_l^1\rangle + \langle H_l^2\rangle) \\ &\quad + 2\,\mathrm{Re} \sum_{mm'} \Big[\int \rho_1(\Omega)\, Y_l^{m\,*}(\Omega)\,\mathrm{d}\Omega \int \rho_2(\Omega')\, Y_l^{m'}(\Omega')\,\mathrm{d}\Omega' D^{l\,*}_{mm'}(R_\xi)\,\mathrm{d}R_\xi\Big] \\ &= \tfrac{1}{4}(\langle H_l^1\rangle + \langle H_l^2\rangle)\,. \end{aligned} \tag{4.24}$$

The $\langle H_l\rangle$ for systems which are randomly rotated with respect to each other therefore obey a linear superposition principle.

Some of the weak decays of heavy mesons should produce leptons. Electrons and muons will appear as 'jets' containing only one particle, while heavy leptons produced in the decays will decay mostly to hadron jets.

Heavy lepton (L) pairs may also be produced directly in e^+e^- annihilation. If they carry new conserved quantum numbers, then their decays should proceed dominantly through the diagram of fig. 28. (We shall not discuss other possible quantum

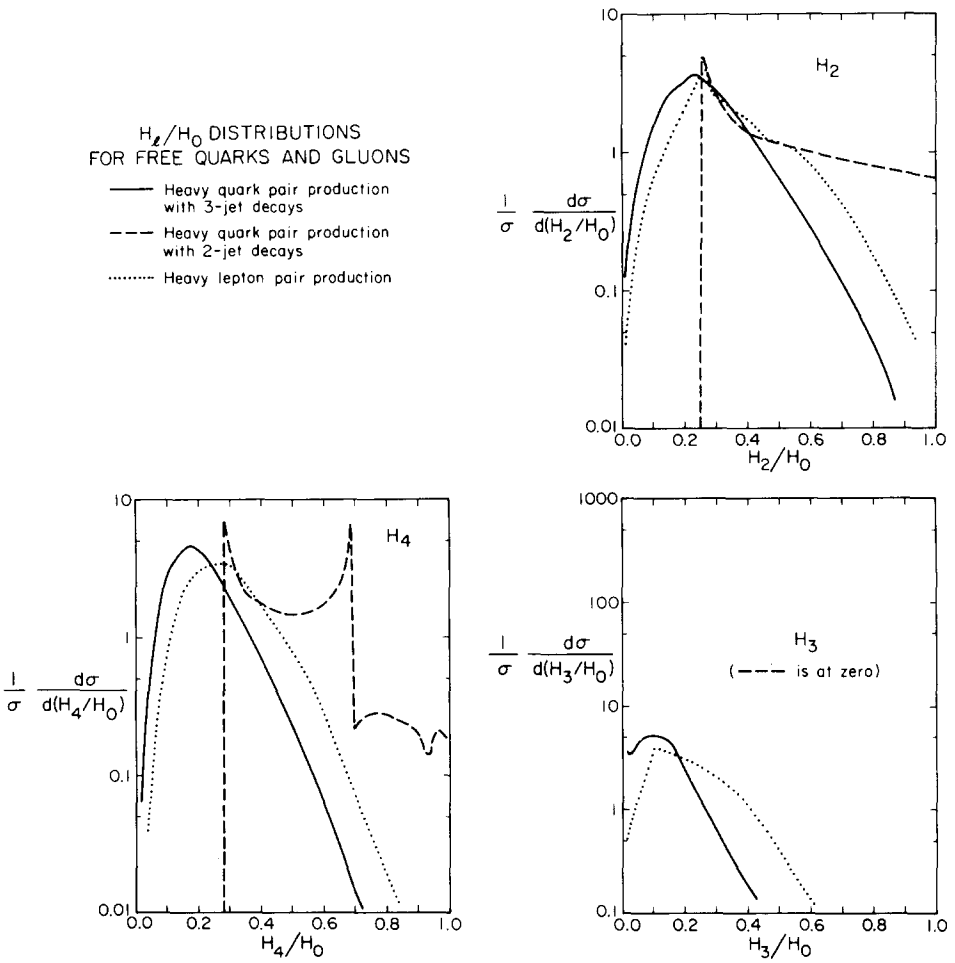

Fig. 29. The distributions in H_2, H_3 and H_4 for the production and decay of heavy quarks and leptons, through the mechanisms of figs. 24–26. (The decay schemes of figs. 25 and 26 both give rise to final states containing two jets. In the approximation of free final quarks and gluons, these two, therefore, give the same results.)

number assignments and will assume a V–A L-ν_L coupling.) Experimentally, the total visible energy in such events will be significantly less than the total c.m. energy because of the presence of the neutrino. (In an apparatus with complete acceptance, the missing energy will probably, in fact, be the best method for identifying these events.) In a free-quark model for the final state, the average fraction of the total

Table 6
Average values of the H_l for the processes discussed in sect. 4

l	$e^+e^- \to q\bar{q}$	$e^+e^- \to q\bar{q}(G)$	$\zeta \to GGG$	$e^+e^- \to M\bar{M} \to qq\bar{q}\bar{q}q$	$e^+e^- \to M\bar{M} \to \begin{cases} q\bar{G}\bar{q}G \\ q\bar{q}\bar{q}q \end{cases}$	$e^+e^- \to L\bar{L} \to q\bar{q}(\nu)\,\bar{q}q(\nu)$
	$\langle H_l \rangle$	c	$\langle H_l \rangle$	$\langle H_l \rangle$	$\langle H_l \rangle$	$\langle H_l/H_0 \rangle$
0	1	0	1	1	1	1
1	0	0	0	0	0	0.11
2	1	−1.4	0.62	0.28	0.50	0.35
3	0	0.43	0.22	0.13	0	0.23
4	1	−2.1	0.49	0.21	0.50	0.30
5	0	0.83	0.29	0.16	0	0.26
6	1	−2.7	0.44	0.20	0.50	0.28
7	0	1.2	0.33	0.18	0	0.26
8	1	−3.2	0.41	0.19	0.50	0.28
9	0	1.5	0.34	0.18	0	0.27
10	1	−3.6	0.40	0.19	0.50	0.27

For $e^+e^- \to q\bar{q}(G)$ (the sum of $e^+e^- \to q\bar{q}$ and $e^+e^- \to q\bar{q}G$ calculated through $O(g^2)$, the coefficient c of $\alpha_s(s)$ is given. The $\langle H_l \rangle$ are related to this by $\langle H_l \rangle = 1 + c\alpha_s(s)$ (l even) and $\langle H_l \rangle = c\alpha_s(s)$ (l odd).

energy visible is $\langle H_0 \rangle = 0.5$. We then find

$$\langle H_1/H_0 \rangle \simeq 0.11 , \qquad \langle H_2/H_0 \rangle \simeq 0.35 ,$$
$$\langle H_3/H_0 \rangle \simeq 0.23 , \qquad \langle H_4/H_0 \rangle \simeq 0.30 . \tag{4.25}$$

Note that even at very high energies, heavy lepton production events should retain their four-jet structure although for large $\sqrt{s}$ the pairs of jets will be boosted to small opening angles in the e^+e^- c.m.s., thereby changing the $\langle H_l \rangle$ for the events. The differential cross-sections $(1/\sigma)\, d\sigma/d(H_l/H_0)$ for idealized (free quark) heavy lepton production events are shown in fig. 29

4.6. The H_l for large l

The $\langle H_l \rangle$ for l from 0 to 10 are given in table 6 for each of the processes discussed above ($e^+e^- \to q\bar{q}$, $e^+e^- \to q\bar{q}(G)$, $e^+e^- \to \zeta \to GGG$, $e^+e^- \to M\bar{M} \to qq\bar{q}\bar{q}q$, $e^+e^- \to M\bar{M} \to qG\bar{q}G$ (or $q\bar{q}\bar{q}q$) and $e^+e^- \to L\bar{L} \to (\nu\bar{\nu})\, qq\bar{q}\bar{q}$). For $e^+e^- \to q\bar{q}(G)$, the coefficient c of α_s in $\langle H_l \rangle = 1 + c\alpha_s$ (l even), $\langle H_l \rangle = c\alpha_s$ (l odd) is given. (As discussed above, these means are calculated from the complete $O(g^2)$ cross section for e^+e^- annihilation, which includes one-loop diagram contributions to $e^+e^- \to q\bar{q}$ as well as the process $e^+e^- \to q\bar{q}G$.) From the formula (2.21), it is possible to compute the limits of the $\langle H_l \rangle$ as $l \to \infty$. As discussed in subsect. 3.4, they are only finite at the lowest order in g^2 for each process. In that case, one finds

$$\langle H_\infty(e^+e^- \to q\bar{q}) \rangle = \tfrac{1}{2} \star ,$$
$$\langle H_\infty(e^+e^- \to GGG) \rangle = \tfrac{3}{4} \int x_1^2 \frac{1}{\sigma} \frac{d\sigma}{dx_1\, dx_2}\, dx_1\, dx_2$$
$$= \frac{13\pi^2 - 127}{4(\pi^2 - 9)} \simeq 0.3751 , \tag{4.26}$$
$$\langle H_\infty(e^+e^- \to M\bar{M} \to qq\bar{q}\bar{q}q) \rangle = \tfrac{11}{60} \simeq 0.1833 ,$$
$$\langle H_\infty(e^+e^- \to L\bar{L} \to (\nu\bar{\nu})\, qq\bar{q}\bar{q})/H_0 \rangle = \tfrac{4}{15} \simeq 0.2667 ,$$
$$\langle H_\infty(e^+e^- \to M\bar{M} \to qG\bar{q}G) \rangle = \tfrac{1}{4} \star .$$

It is clear from table 6 that these limits are, in fact, approached very quickly as l increases (to within 5% at $l = 5$). For $e^+e^- \to q\bar{q}(G)$, the H_l approach a limit at large l, but this limit is not infrared finite and diverges as the artificial gluon mass is taken to zero. This behavior is evident in table 6.

The distributions $(1/\sigma)\, d\sigma/dH_l$ are shown in fig. 30 for l up to 9. Spikes in the

* See eq. (2.21) for a more precise result in this case.

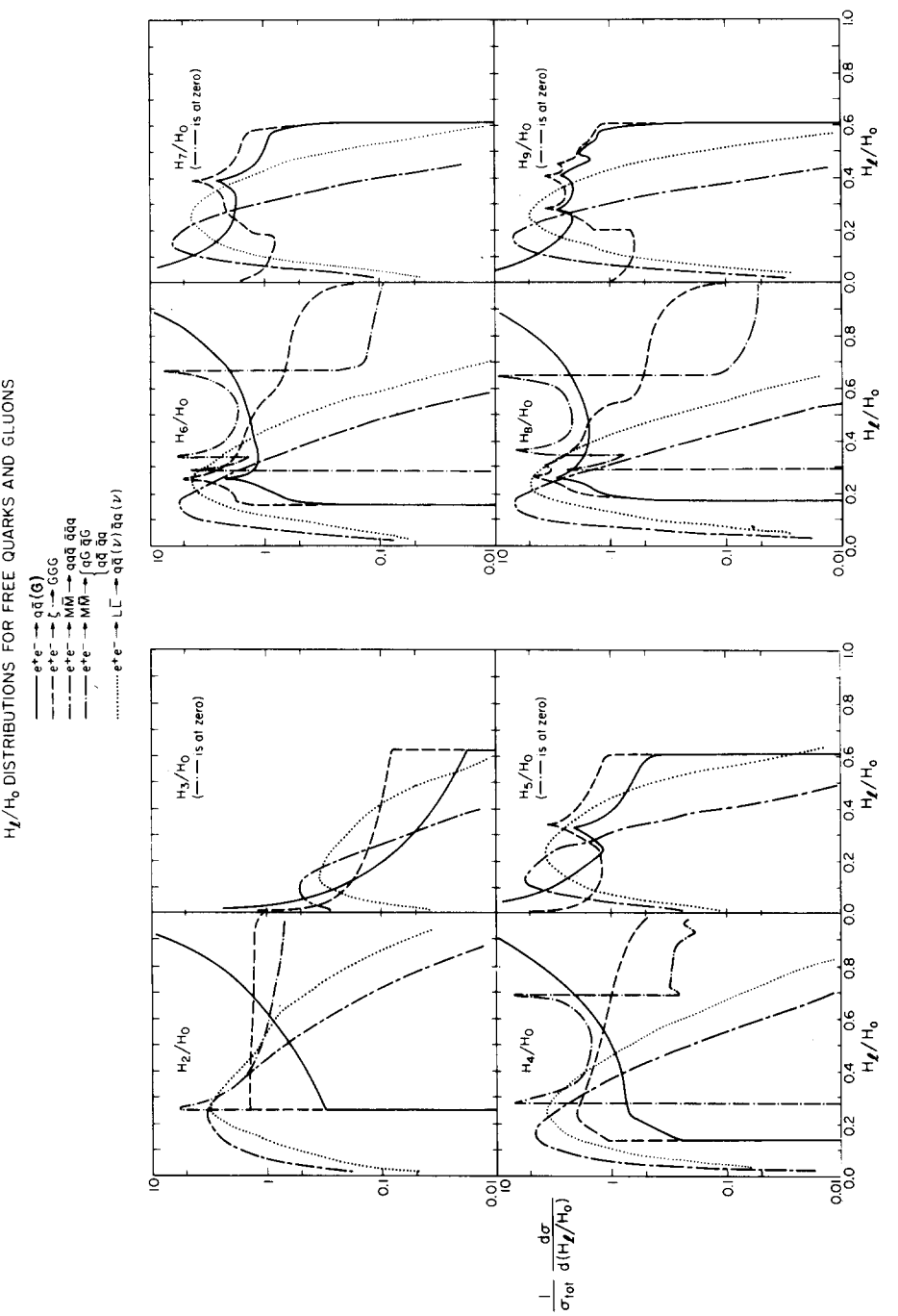

Fig. 30. The distributions $(1/\sigma)\, d\sigma/d(H_l/H_0)$ for various processes in the free quark and gluon approximation.

distributions occur when the formula for H_l is stationary with respect to variations of the parameters which specify the configuration of the final state. For production and decay of pairs of heavy quarks into a total of four final particles, the formula (4.22) shows that H_l is stationary with respect to the angle ξ between the directions of the decays when the value of H_l corresponds to a stationary point in $P_l(\xi)$. The minima are determined from the minima of the Legendre polynomials, by $\mathrm{Min}[H_{2l}] = \frac{1}{2}(1 + P_{2l}(0))$. In our model, six-particle final states resulting from the production and decay of pairs of heavy quarks or leptons are specified by the values of four parameters. Spikes in the H_l distribution for six-particle final states will occur only if the value of H_l is stationary with respect to variations in all four parameters. This does not occur for $l \leqslant 10$.

The forms of the H_l for three-particle final states are stationary with respect to the values of x_1 and x_2 which specify the final-state configuration at values of x_1 and x_2 within the physical region. For $l < 5$, the only stationary point is at $x_1 = x_2 = x_3 = \frac{2}{3}$, and yields the minimum (maximum) value of H_l for even (odd) l. For $l \geqslant 5$, other stationary points develop within the physical region, and spikes appear in the H_l distributions at the values of H_l corresponding to these stationary points. The maximum (minimum) values of H_l for odd (even) l always occur when $x_1 = x_2$ (or $x_2 = x_3$, or $x_3 = x_1$). Many stationary points develop along these lines for high l; it is always the one nearest to (but not on) the edge of the physical which yields the extremal value of H_l. For example, H_5 is stationary when $x_1 = x_2 = \frac{1}{2}, 0.560, \frac{2}{3}, 0.758, 1$, at which $H_5 = 0, 0.606, 0.273, 0.337, 0$, respectively. The first of these stationary points is at the edge of the physical region, where H_5 goes smoothly to zero. The stationary point at $x_1 = x_2 \simeq 0.560$ is one of three absolute maxima placed symmetrically on the lines $x_1 = x_2, x_2 = x_3$ and $x_3 = x_1$. There is a local minimum between these three peaks at $x_1 = x_2 = x_3 = \frac{2}{3}$. Finally, at $x_1 = x_2 \simeq 0.758$ there is a saddle point between the peaks at $x_2 = x_3 \simeq 0.560$ and $x_3 = x_1 \simeq 0.560$.

5. Results for realistic jets

5.1. The model for jet development

At present, QCD can give little guidance as to the way in which quarks and gluons 'fragment' into hadrons. We use the explicit model for the development of hadronic jets due to Field and Feynman [18]. The basic assumption of this model is that hadrons are emitted from a 'fragmenting' quark or gluon independently and with limited transverse momenta. Strong and electromagnetically decaying hadrons such as the $\rho, \omega, \eta, \eta', \ldots$ are taken to be among those produced, and their decays are treated exactly. The fragmentation of a particular type of quark or gluon is specified by giving the probability function $f(1 - z_1)$, where z_1 is the fraction of the jet's total momentum that is carried off by the first hadron emitted. If one chooses

$$f(1 - z) = (p + 1)(1 - z)^p , \tag{5.1}$$

then the distribution of the fractional momenta (z) of all hadrons in the jet is given approximately by

$$D(z) = (p + 1)(1 - z)^p/z \,. \tag{5.2}$$

A precise treatment requires the inclusion of transverse momenta and the possibility of producing many species of hadrons [18]. Field and Feynman adjusted the forms of $f(z)$ so as to agree with experimental estimates of $D(z)$ for quark fragmentation. Their final choice was

$$f_{\text{quarks}}(1 - z) = 0.12 + 2.64(1 - z)^2 \,. \tag{5.3}$$

We also need the corresponding function for gluons. In the absence of good experimental constraints, we use the simple form of eq. (5.1). We usually take $p = 4$, but we also present some results using $p = 2$ and $p = 10$.

Our calculations of the expected distributions in the H_I for genuine hadronic events require a model for the complete structure of a hadron jet, rather than just one-particle momentum distributions $D(z)$. In using the complete jets provided by the Field-Feynman model [18], we are relying more heavily on its basic assumptions (especially independent emission) than do predictions for one-particle distributions. Limited experimental tests [19] on the detailed structure of jets predicted by the model have, however, proved successful. When further experimental data become available, the model for jet development must be refined accordingly.

The parameters in the Field-Feynman model were determined by fitting data from various reactions at comparatively low Q^2 assuming that all events contained only the minimum number of jets (two for e^+e^- annihilation). In reality, some of the events will have contained extra jets. On the other hand, we use the model to simulate the fragmentation of a single jet, and sometimes include explicitly the fragmentation of the extra jets. It therefore appears that the contribution of extra jets has been counted twice. However, our results show that for the low Q^2 at which the jet-model parameters were determined, the distributions of hadrons produced in two jets and in three jets of the same total energy are almost identical, so it seems that roughly the correct parameters to describe single-jet fragmentation at high energies were found.

Note that the Field-Feynman jet model gives rise to hadron transverse and longitudinal momentum (z) distributions which asymptotically become independent of the total jet energy, in contradiction to the predictions of QCD. In addition, as discussed in sect. 3, it does not include the 'mixing' of jets generated from quarks and from gluons implied by QCD.

The present formulation of the Field-Feynman jet model does not conserve energy and momentum exactly, as discussed in detail in ref. [18]. The violations are worst for low jet energies, and the model becomes unreliable for jets with energies below about 2 GeV. This inadequacy of the model for small jet energies prevents any useful comparison of its predictions with existing data on hadron production in e^+e^- annihilation. Moreover, there is some inconsistency between the data from different experiments [1].

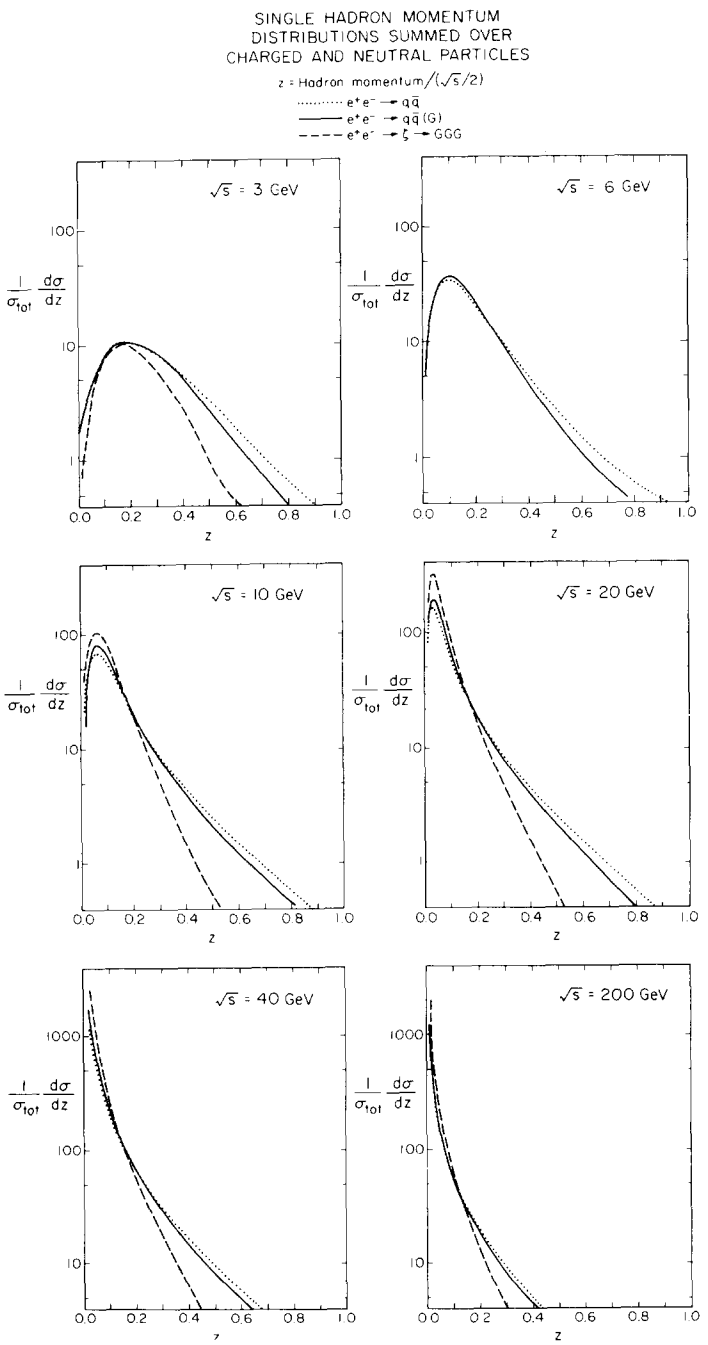

Fig. 31. Distributions in fractional momentum (z) for single hadrons produced by $e^+e^- \to q\bar{q}$, $e^+e^- \to q\bar{q}(G)$ and $e^+e^- \to \zeta \to GGG$ as a function of the c.m. energy $\sqrt{s}$.

5.2. Momentum distributions and multiplicities for two- and three-jet processes

In this and subsects. 5.3, 5.4, we discuss hadronic final states arising from the three basic processes

$$e^+e^- \to q\bar{q}\,, \qquad e^+e^- \to q\bar{q}(G)\,, \qquad e^+e^- \to \zeta \to GGG\,. \tag{5.4}$$

Of course, the process $e^+e^- \to q\bar{q}G$ cannot be observed in isolation, but only in combination with $e^+e^- \to q\bar{q}$. We denote the combined processes by $e^+e^- \to q\bar{q}(G)$. As discussed in sect. 3, the method of combination is not entirely unambiguous. Events arising from the process $e^+e^- \to q\bar{q}G$ are divided into two classes according to whether the value of H_2 calculated for the quarks and gluons is above or below a cut-off H_2^c. The events below the cut-off are considered as true three-jet events, and the fragmentations of the quark, antiquark and gluon into hadrons are treated separately. Events above the cut-off are taken to contain two, rather than three, jets and to be indistinguishable from $e^+e^- \to q\bar{q}$. The total cross section is only finite when these events are combined with the genuine $e^+e^- \to q\bar{q}$ term. We simply generate two-jet (quark and antiquark) final states for the combined $e^+e^- \to q\bar{q}G$ ($H_2 > H_2^c$) and $q\bar{q}$ ($H_2 = 1$) terms. An example may make this prescription clearer. For $\sqrt{s}$ = 20 GeV, the cross section for $e^+e^- \to q\bar{q}G$ for $H_2 < 0.8$ is 0.41 times the point cross section. In the same units, the total e^+e^- cross section to order g^2 is $1 + \alpha_s(s)/\pi \simeq 1.06$. At this energy, therefore, the ratio of three- to two-jet final states is 0.41 : 0.65. We shall usually take $H_2^c = 0.8$, although, as we shall discuss below, this choice is unreasonable in certain cases.

Fig. 31 shows the single-hadron fractional momentum (z) distributions (longitudinal plus transverse momentum) for hadronic final states resulting from the three basic processes $e^+e^- \to q\bar{q}$, $e^+e^- \to q\bar{q}(G)$ and $e^+e^- \to \zeta \to GGG$ (ζ is a heavy vector meson). Note that the turnover in the distributions at small z moves closer to zero as $\sqrt{s}$ increases. The presence of such a turnover is a consequence of the finite transverse momenta (k_T) of the hadrons in the jets. The Field-Feynman model is such that $\langle k_T \rangle$ and $\langle z \rangle$ are roughly constant with energy, so that as $\sqrt{s}$ increases, the transverse momenta of the hadrons become insignificant compared to their longitudinal momenta, and the turnover disappears. At very high energies, the hadron momentum distributions tend to a limit given for gluon jets by eq. (5.2) and for quark jets by ref. [18]. Notice that at all energies, the z distributions for hadrons from the process $e^+e^- \to \zeta \to GGG$ are significantly steeper than those from the processes $e^+e^- \to q\bar{q}$ and $e^+e^- \to q\bar{q}(G)$, while results for the latter two processes never differ by more than about 20%. The model we use predicts that even at $\sqrt{s}$ = 3 GeV, the process $\zeta \to GGG$ should give a steeper hadron z distribution than $e^+e^- \to q\bar{q}$. One would, therefore, expect a difference between the z distributions in ψ decays and in the surrounding continuum. This prediction seems difficult to avoid as it also occurs in simpler models not involving the generation of complete hadronic final states, but formulated solely in terms of fragmentation functions into single hadrons. It is, therefore, surprising that the experimental single-hadron distributions seem identical on and

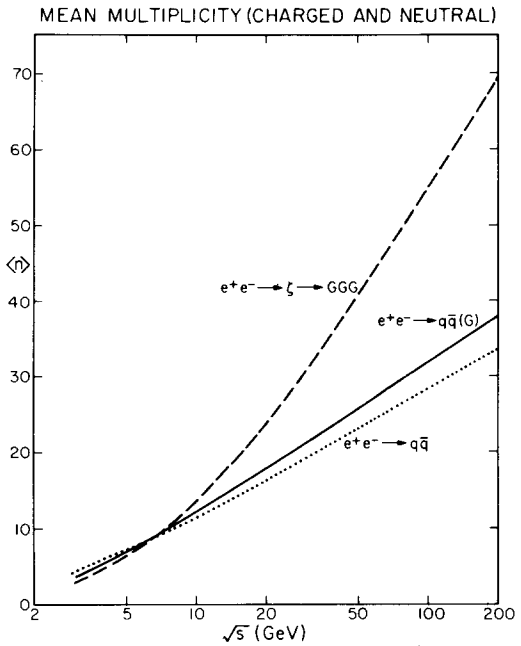

Fig. 32. The mean multiplicity of hadrons from the processes $e^+e^- \to q\bar{q}$, $e^+e^- \to q\bar{q}(G)$ and $e^+e^- \to \zeta \to GGG$ as a function of $\sqrt{s}$.

off the ψ resonance [1]. Nevertheless, the correct inclusion of scaling violations in the fragmentation functions (which is complicated by the need to consider $k_\perp$) could remove the discrepancy.

Fig. 32 shows the mean hadron multiplicity due to the processes $e^+e^- \to q\bar{q}$, $e^+e^- \to q\bar{q}(G)$ and $e^+e^- \to \zeta \to GGG$ as a function of the c.m. energy $\sqrt{s}$. At sufficiently high energies ($\sqrt{s} \gtrsim 20$ GeV), the multiplicities rise like $\log s$, with coefficients given by the heights of the rapidity plateaus for the various processes (or equivalently, the limits of $(z/\sigma)\, d\sigma/dz$ as $z \to 0$). Our choice for the gluon fragmentation function (eq. (5.2)) leads to a higher rapidity plateau (hence, higher hadron multiplicity) for gluon jets than for quark jets at high energies. At low energies, however, the rapidity plateau is not fully developed, and it is a matter of detailed calculation to determine whether quark or gluon jets have higher hadron multiplicities. We find, in fact, that below $\sqrt{s} \simeq 6$ GeV, the process $e^+e^- \to GGG$ gives a lower mean hadron multiplicity than $e^+e^- \to q\bar{q}$. The details are sensitive to the gluon fragmentation function. For example, in the Υ region ($\sqrt{s} \simeq 10$ GeV), we find

$$\begin{aligned} \langle n \rangle_{e^+e^- \to q\bar{q}} &\simeq 11.5\,, \\ \langle n \rangle_{e^+e^- \to q\bar{q}(G)} &\simeq 12.0\,, \\ \langle n \rangle_{e^+e^- \to \zeta \to GGG} &\simeq 13.5\,, \end{aligned} \tag{5.5}$$

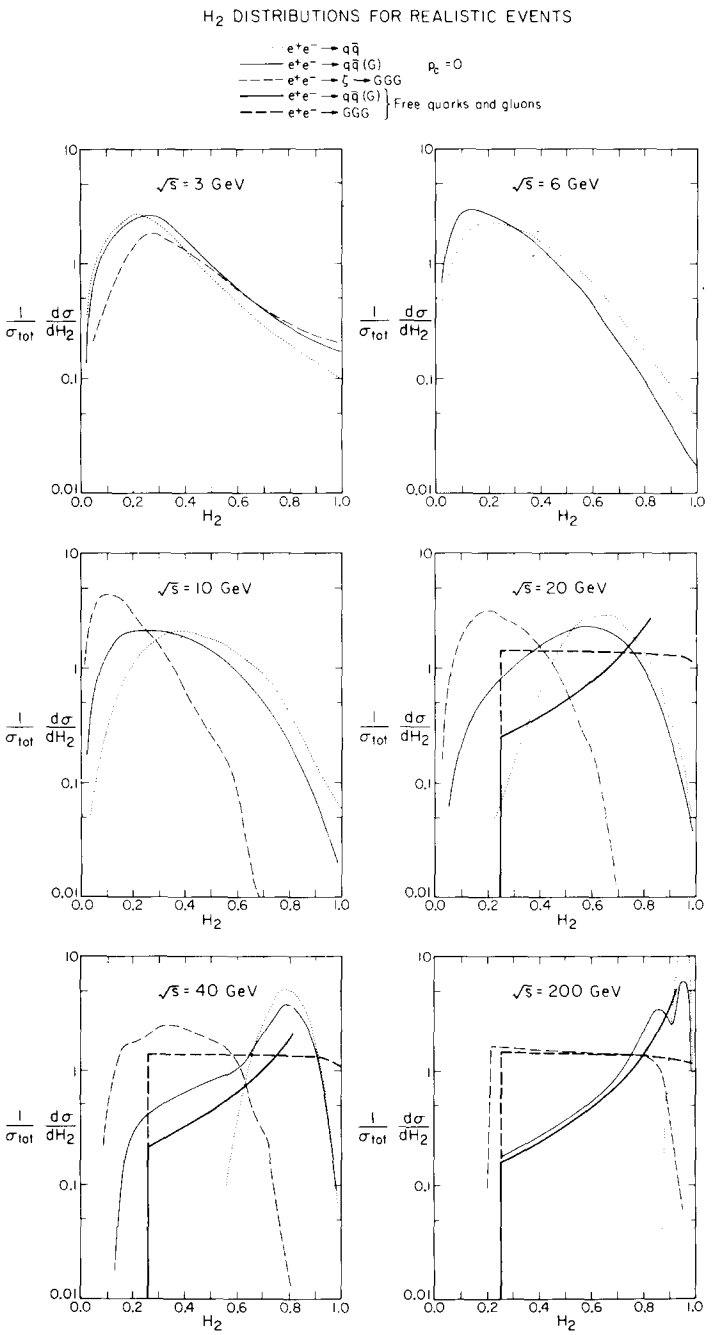

Fig. 33. The distributions $(1/\sigma_{tot})\, d\sigma/dH_2$ for hadronic events resulting from the processes $e^+e^- \to q\bar{q}$, $e^+e^- \to q\bar{q}(G)$ and $e^+e^- \to \zeta \to GGG$, at various c.m. energies, $\sqrt{s}$. All hadrons in the simulated events were used, no momentum cut (p_c) being imposed. On some of the graphs for high values of $\sqrt{s}$, we also show the distributions obtained for final states of free quarks and gluons (see fig. 23). The parameter H_2^c defined in subsect. 5.1 was taken to be 0.8 at all energies except $\sqrt{s}$ = 200 GeV, for which H_2^c = 0.95 was used.

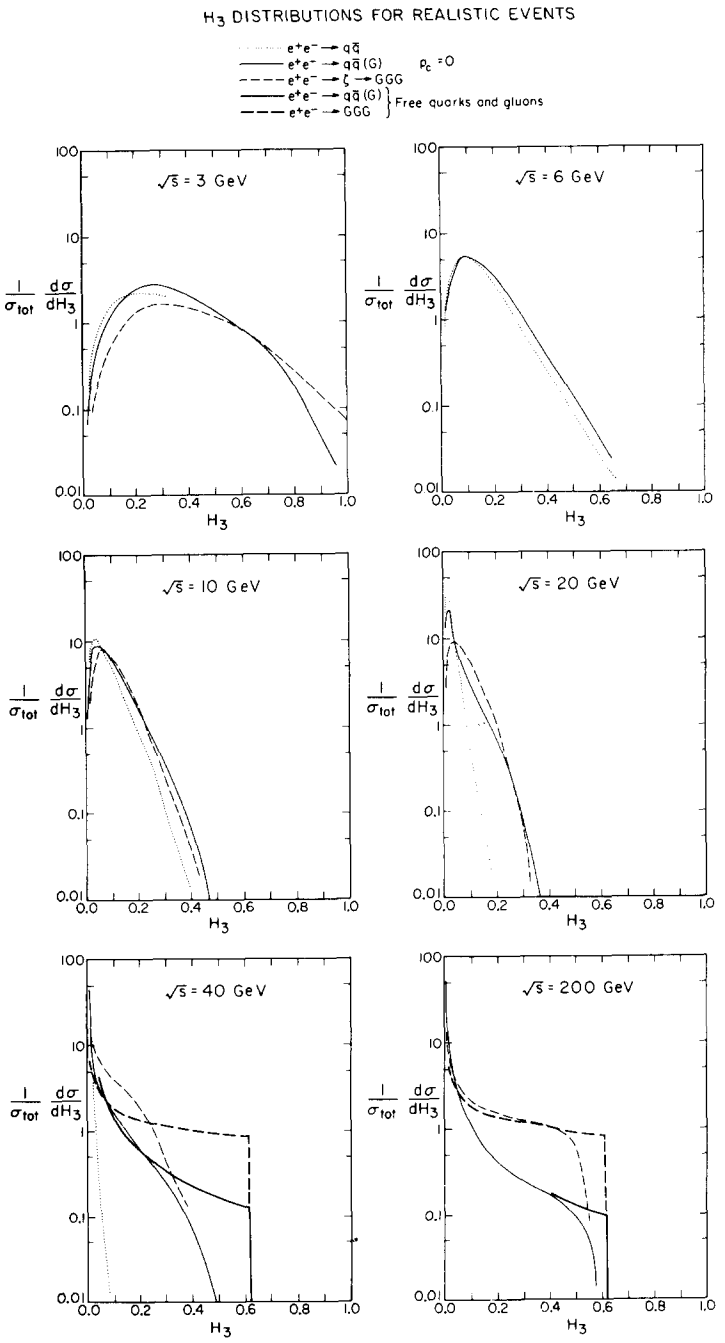

Fig. 34. The distributions $(1/\sigma_{tot})\, d\sigma/dH_3$ for hadronic events resulting from the processes $e^+e^- \to q\bar{q}$, $e^+e^- \to q\bar{q}(G)$ and $e^+e^- \to \zeta \to GGG$, at various c.m. energies, $\sqrt{s}$. See fig. 33 for other details.

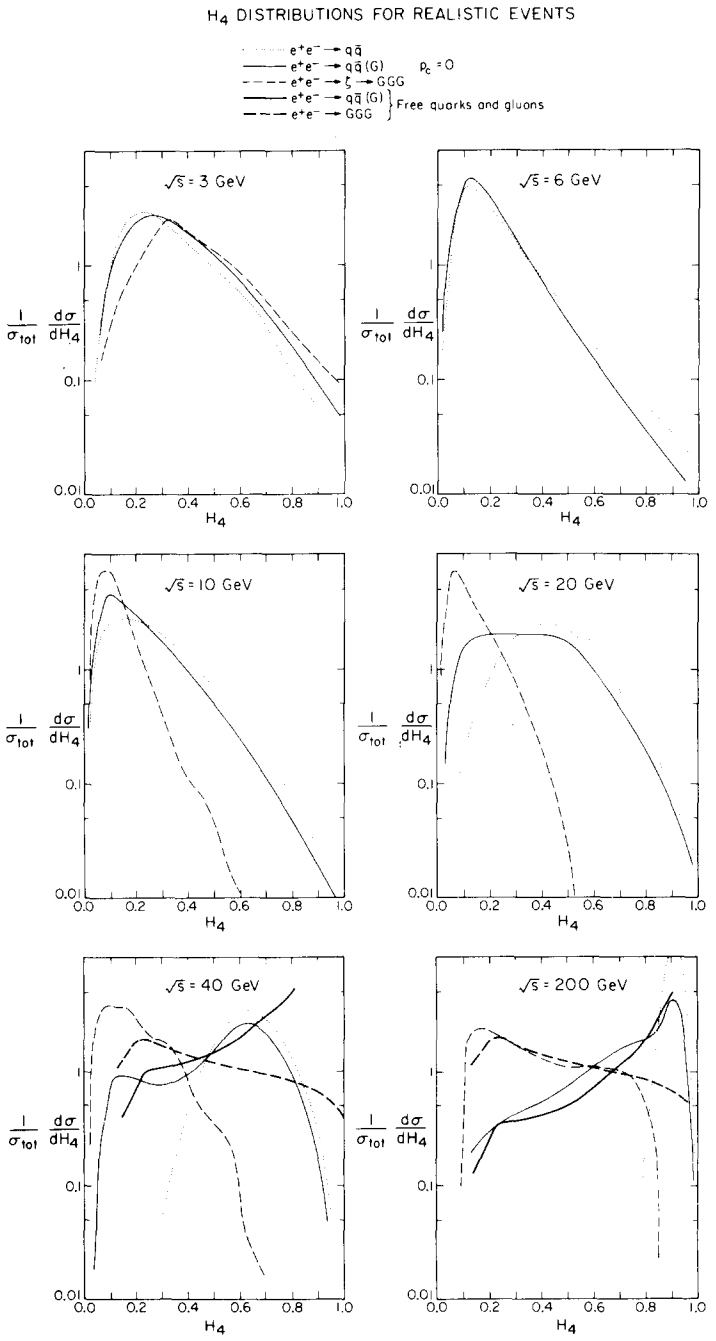

Fig. 35. The distributions $(1/\sigma_{tot})\, d\sigma/dH_4$ for hadronic events resulting from the processes $e^+e^- \to q\bar{q}$, $e^+e^- \to q\bar{q}(G)$ and $e^+e^- \to \zeta \to GGG$, at various c.m. energies, $\sqrt{s}$. See fig. 33 for other details.

Table 7
Average values of the H_l for realistic hadronic events resulting from the processes $e^+e^- \to q\bar{q}$, $e^+e^- \to q\bar{q}(G)$ (combination of $e^+e^- \to q\bar{q}$ and $e^+e^- \to q\bar{q}G$ calculated through $O(g^2)$) and $e^+e^- \to \zeta \to GGG$, for various c.m. energies $\sqrt{s}$

$\sqrt{s}$ (GeV)	p_c (GeV)		$\langle H_2 \rangle$		
			$q\bar{q}$	$q\bar{q}(G)$	GGG
3	0		0.33	0.39	0.49
6	0		0.33	0.25	
10	0		0.44	0.29	0.18
10	0	$zD(z) \sim (1-z)^2$	0.44	0.28	0.27
10	0	$zD(z) \sim (1-z)^{10}$	0.44	0.31	0.13
10	0.5		0.58	0.44	0.34
10	0.5	charged only	0.65	0.53	0.47
20	0		0.64	0.31	0.26
20	0.5		0.74	0.48	0.37
20	0.5	charged only	0.73	0.51	0.40
20	0.5	$H_2^c = 0.9$	0.74	0.57	0.37
20	0.5	$H_2^c = 0.6$	0.74	0.36	0.37
20	0.5	$zD(z) \sim (1-z)^2$	0.74	0.47	0.46
20	0.5	$zD(z) \sim (1-z)^{10}$	0.74	0.49	0.25
20	1		0.88	0.68	0.61
40	0		0.77	0.47	0.38
40	0.5		0.85	0.54	0.46
40	0.5	$H_2^c = 0.9$	0.85	0.64	0.46
40	1		0.93	0.60	0.59
200	0		0.95	0.58	0.55
∞			1.0	1.0	0.62

$\sqrt{s}$ (GeV)	p_c (GeV)		$\langle H_3 \rangle$		
			$q\bar{q}$	$q\bar{q}(G)$	GGG
3	0		0.32	0.39	0.50
6	0		0.15	0.18	
10	0		0.08	0.12	0.11
10	0	$zD(z) \sim (1-z)^2$	0.08	0.12	0.12
10	0	$zD(z) \sim (1-z)^{10}$	0.08	0.14	0.13
10	0.5		0.03	0.14	0.13
10	0.5	charged only	0.32	0.37	0.40
20	0		0.03	0.10	0.08
20	0.5		0.03	0.14	0.13
20	0.5	charged only	0.18	0.23	0.21
20	0.5	$H_2^c = 0.9$	0.03	0.10	0.13
20	0.5	$H_2^c = 0.6$	0.03	0.19	0.13
20	0.5	$zD(z) \sim (1-z)^2$	0.03	0.14	0.15
20	0.5	$zD(z) \sim (1-z)^{10}$	0.03	0.14	0.12
20	1		0.06	0.23	0.27
40	0		0.008	0.12	0.10

Table 7 (continued)

$\sqrt{s}$ (GeV)	p_c (GeV)		$\langle H_4 \rangle$ $q\bar{q}$	$q\bar{q}(G)$	GGG
40	0.5		0.007	0.14	0.13
40	0.5	$H_2^c = 0.9$	0.007	0.09	0.13
40	1		0.01	0.17	0.19
200	0		0.003	0.16	0.17
∞			0	0	0.21
3	0		0.33	0.40	0.49
6	0		0.23	0.20	
10	0		0.27	0.17	0.12
10	0	$zD(z) \sim (1-z)^2$	0.27	0.17	0.17
10	0	$zD(z) \sim (1-z)^{10}$	0.27	0.19	0.13
10	0.5		0.37	0.27	0.24
10	0.5	charged only	0.48	0.42	0.42
20	0		0.44	0.22	0.13
20	0.5		0.53	0.28	0.19
20	0.5	charged only	0.54	0.34	0.26
20	0.5	$H_2^c = 0.9$	0.53	0.36	0.19
20	0.5	$H_2^c = 0.6$	0.53	0.20	0.19
20	0.5	$zD(z) \sim (1-z)^2$	0.53	0.29	0.27
20	0.5	$zD(z) \sim (1-z)^{10}$	0.53	0.29	0.14
20	1		0.70	0.46	0.39
40	0		0.61	0.27	0.21
40	0.5		0.70	0.35	0.26
40	0.5	$H_2^c = 0.9$	0.70	0.35	0.26
40	1		0.81	0.46	0.38
200	0		0.91	0.44	0.39
∞			1.0	1.0	0.50

In some cases, a momentum cut p_c has been applied so that only hadrons with momenta above the cut are used in the calculation of the H_l for each event. 'Charged only' means that for that case, the $\langle H_l \rangle$ were computed using only the charged hadrons in the final state. H_2^c is a parameter which divides $e^+e^- \to q\bar{q}(G)$ processes into two and three-jet events. $D(z)$ is the gluon fragmentation function discussed in subsect. 5.1. The defaults are discussed in sect. 5.

if we use our standard choice of $(1-z)^4$ for the gluon fragmentation function. If we take instead $(1-z)^2$ or $(1-z)^{10}$, then the mean multiplicity for $\zeta \to GGG$ becomes 12.8 or 11.2, respectively.

5.3. *Shapes of two- and three-jet events*

We now discuss the H_l distributions for realistic hadronic events resulting from the processes $e^+e^- \to q\bar{q}$, $e^+e^- \to q\bar{q}(G)$ and $e^+e^- \to \zeta \to GGG$. It should be emphasized that, if QCD is correct, then the pure two-jet process $e^+e^- \to q\bar{q}$ should never be observed; only the combination of two- and three-jet processes which we denote

by $e^+e^- \to q\bar{q}(G)$ should be present. (Of course, higher-order processes involving the production of more than three jets should also occur, but we do not expect their inclusion to modify our results appreciably.)

Note that the H_l could also be used to distinguish the approximate two-jet structure expected from QCD from purely isotropic production of particles [17]. For an exactly isotropic event, $H_l = 0$ for all $l \geqslant 1$.

Figs. 33–35 show the distributions $(1/\sigma_{tot})\, d\sigma/dH_2$, $(1/\sigma_{tot})\, d\sigma/dH_3$ and $(1/\sigma_{tot})\, d\sigma/dH_4$ for simulated hadronic events resulting from $e^+e^- \to q\bar{q}$, $e^+e^- \to q\bar{q}(G)$ and $e^+e^- \to \zeta \to GGG$, at various center of mass energies $\sqrt{s}$. Table 7 gives $\langle H_2 \rangle$, $\langle H_3 \rangle$ and $\langle H_4 \rangle$ for these and other cases. Perhaps the most striking feature of these figures and the table is the large difference between the results for realistic hadronic final states, and those obtained using the free quark and gluon approximation (fig. 23 and table 6). We believe that large modification of free quark and gluon results for realistic final states is not a phenomenon peculiar to the H_l; rather, it will occur for all the other shape parameters previously investigated [5,6]. As we shall discuss in subsect. 5.4, use of only the higher momentum hadrons in each event leads to H_l distributions which are closer to the free quark and gluon approximations.

As discussed above, the model for jet fragmentation which we use is unreliable for total jet energies below about 2 GeV. Our results for three-jet production at $\sqrt{s}$ = 6 GeV should, therefore, not be taken too seriously while at $\sqrt{s}$ = 3 GeV, even the results for two-jet production should be considered somewhat suspect. However, we expect the similarity between the H_l distributions for the various processes at these energies to survive the use of a more adequate model.

At $\sqrt{s}$ = 10 GeV, the H_2 distribution for hadronic events resulting from the process $e^+e^- \to \zeta \to GGG$ is very different from that due to $e^+e^- \to q\bar{q}$ or $e^+e^- \to q\bar{q}(G)$. We find that at this energy (see table 7)

$$\langle H_2 \rangle_{e^+e^- \to q\bar{q}} \simeq 0.44\,,$$

$$\langle H_2 \rangle_{e^+e^- \to q\bar{q}(G)} \simeq 0.29 \qquad (5.6)$$

$$\langle H_2 \rangle_{e^+e^- \to \zeta \to GGG} \simeq 0.18\,.$$

A difference between the H_2 distributions and $\langle H_2 \rangle$ on and off resonance in the Υ region should, therefore, be easily measurable, and would provide an important test of the mechanism for the decays of heavy vector mesons. We usually take $D(z) \sim (1-z)^4/z$ for the gluon fragmentation function. Fig. 36 shows the dependence of the H_2 distribution at $\sqrt{s}$ = 10 GeV from $e^+e^- \to q\bar{q}(G)$ and $e^+e^- \to \zeta \to GGG$ on the form of the gluon fragmentation function $D(z)$. We consider the choices $D(z) \sim (1-z)^2/z$, $D(z) \sim (1-z)^4/z$ (standard choice) and $D(z) \sim (1-z)^{10}/z$. Very little change is effected in the H_2 distribution for $e^+e^- \to q\bar{q}(G)$, but the H_2 distribution for $e^+e^- \to \zeta \to GGG$ changes appreciably when different forms for the gluon fragmentation function are used. Since, however, the single-hadron momentum distributions from Υ decay should allow the gluon fragmentation function to be deter-

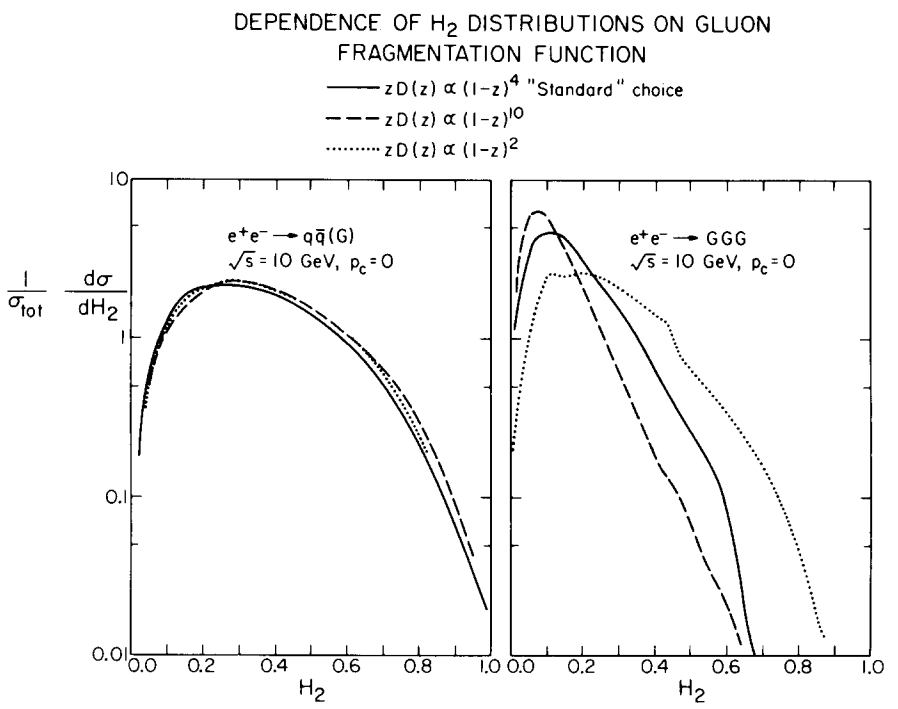

Fig. 36. The distributions $(1/\sigma_{tot})\, d\sigma/dH_2$ for hadronic events resulting from the processes $e^+e^- \to q\bar{q}(G)$ and $e^+e^- \to \zeta \to GGG$ for three possible forms of the gluon fragmentation function $D(z)$.

mined, the form of the H_2 distribution for the decay remains an important test of its basic mechanism. Note that, as discussed in sect. 4, even on the Υ resonance, there should be $q\bar{q}$ (in reality $q\bar{q}(G)$) as well as GGG final states. The contribution of the former must be subtracted before a study of the process $e^+e^- \to \zeta \to GGG$ may be made. We do not expect the change to be very large.

As shown by fig. 35 and table 7, the differences between the H_4 distributions and their means also provide a good method for identifying the possible two- and three-jet processes at $\sqrt{s} = 10$ GeV. H_2 and H_4 are particularly effective at discriminating between $e^+e^- \to \zeta \to GGG$ and $e^+e^- \to q\bar{q}(G)$. On the other hand, the H_3 distributions at $\sqrt{s} = 10$ GeV for the processes $e^+e^- \to q\bar{q}(G)$ and $e^+e^- \to \zeta \to GGG$ are rather similar, but are very different from those for $e^+e^- \to q\bar{q}$.

For $\sqrt{s} = 20$ GeV, the H_2, H_3 and H_4 distributions from $e^+e^- \to q\bar{q}$, $e^+e^- \to q\bar{q}(G)$ and $e^+e^- \to \zeta \to GGG$ events are all very different. Once again, the H_3 distribution is the best measure of any contributions from pure $e^+e^- \to q\bar{q}$ processes, while the H_4 and especially H_2 distributions exhibit the largest differences between the processes $e^+e^- \to \zeta \to GGG$ and $e^+e^- \to q\bar{q}(G)$ expected on and off heavy vector meson resonances.

At $\sqrt{s} = 40$ GeV, the H_2 distributions for $e^+e^- \to \zeta \to GGG$ and $e^+e^- \to q\bar{q}(G)$ show marked similarity to the distributions obtained for these processes in the approximation of free final quarks and gluons. Note the appearance of a kink in $(1/\sigma_{tot})\, d\sigma/dH_2$ for $e^+e^- \to q\bar{q}(G)$ events around $H_2 = 0.6$. Below the kink, most events of this type will have three-jet final states, while above, most will give only two jets. The distribution in H_2 for pure $e^+e^- \to q\bar{q}$ events is, of course, very similar to that for $e^+e^- \to q\bar{q}(G)$ when $H_2 \gtrsim 0.6$. The H_3 and H_4 distributions at $\sqrt{s} = 40$ GeV bear less resemblance to the free quark and gluon results than the H_2 distribution, but they still offer ample discrimination between events of different types.

It is interesting that $\sqrt{s} \gtrsim 30$ GeV is required for even the H_2 distribution for realistic hadron final states to be similar to the free quark and gluon approximation. This phenomenon should be universal to all parametrizations of the 'shapes' of final hadron states. Previous estimates of its importance for spherocity and thrust based on very simple models for quark and gluon fragmentation [6] were probably too optimistic. Nevertheless, it seems likely that our results for realistic hadronic events do not depend significantly on the details of the model for quark and gluon fragmentation used, and so remain firm predictions of QCD.

Finally, at $\sqrt{s} = 200$ GeV, all the distributions are very close to the free quark and gluon predictions. The cross sections for the simulated hadronic events drop away very quickly at the boundaries of the kinematic region for the quark-gluon subprocesses ($H_2 = 0.25, H_3 = 0.625, H_4 \simeq 0.141$). Four-jet events may give important contributions to the cross sections outside the physical regions for three-particle subprocesses.

In the H_2 distribution for $e^+e^- \to q\bar{q}(G)$ events at $\sqrt{s} = 200$ GeV, a dip around $H_2 \simeq 0.9$ is clearly visible. This dip signals the boundary between two- and three-jet processes, and is an artifact of our model. It has no physical significance.

As discussed above, it is necessary to separate $e^+e^- \to q\bar{q}(G)$ processes into two- and three-jet events in order to treat their fragmentation into hadrons. This separation is achieved by dividing the events according to the value of H_2 corresponding to the fragmenting quarks and gluons. For $H_2 > H_2^c$, $e^+e^- \to q\bar{q}(G)$ events are treated as being of the form $e^+e^- \to q\bar{q}$, while for $H_2 < H_2^c$ the event is assumed to contain three jets, and the fragmentations of the q, $\bar{q}$ and G into hadrons are treated separately. The magnitude of the two-jet contribution is determined by demanding that the sum of the two- and three-jet pieces reproduce the correct total cross section for $e^+e^- \to q\bar{q}(G)$ to $O(g^2)$. For most of the distributions shown in figs. 33–35 we used $H_2^c = 0.8$, but at $\sqrt{s} = 200$ GeV, we took instead $H_2^c = 0.95$. The value of H_2^c should be chosen so that $e^+e^- \to q\bar{q}G$ processes with $H_2 > H_2^c$ are indistinguishable from $e^+e^- \to q\bar{q}$ ones as far as their fragmentation to hadrons is concerned. H_2^c may be thought of as a parameter which determines the 'resolution' of the final hadron state to different configurations of the quarks and gluons produced in the primary interaction. The closer H_2^c is to one, the lower the energy (and angle) of the gluon in the process $e^+e^- \to q\bar{q}G$ must be for the hadronic final state not to reflect its presence, and to consist only of two jets. The choice of the

'resolution parameter' H_2^c for the hadronic final state depends on the model for quark and gluon fragmentation used. Even in the context of a particular model, its value must, at present, essentially be guessed. We have simply tried to choose it so that our results are not obviously unphysical. The signal for too small a choice of H_2^c is the appearance of separated peaks in $(1/\sigma_{tot})\, d\sigma/dH_2$ corresponding to two- and three-jet events. In this case, the 'resolution' of the simulated hadron final state is really finer than the division into two- and three-jet processes chosen; the hadron final state can

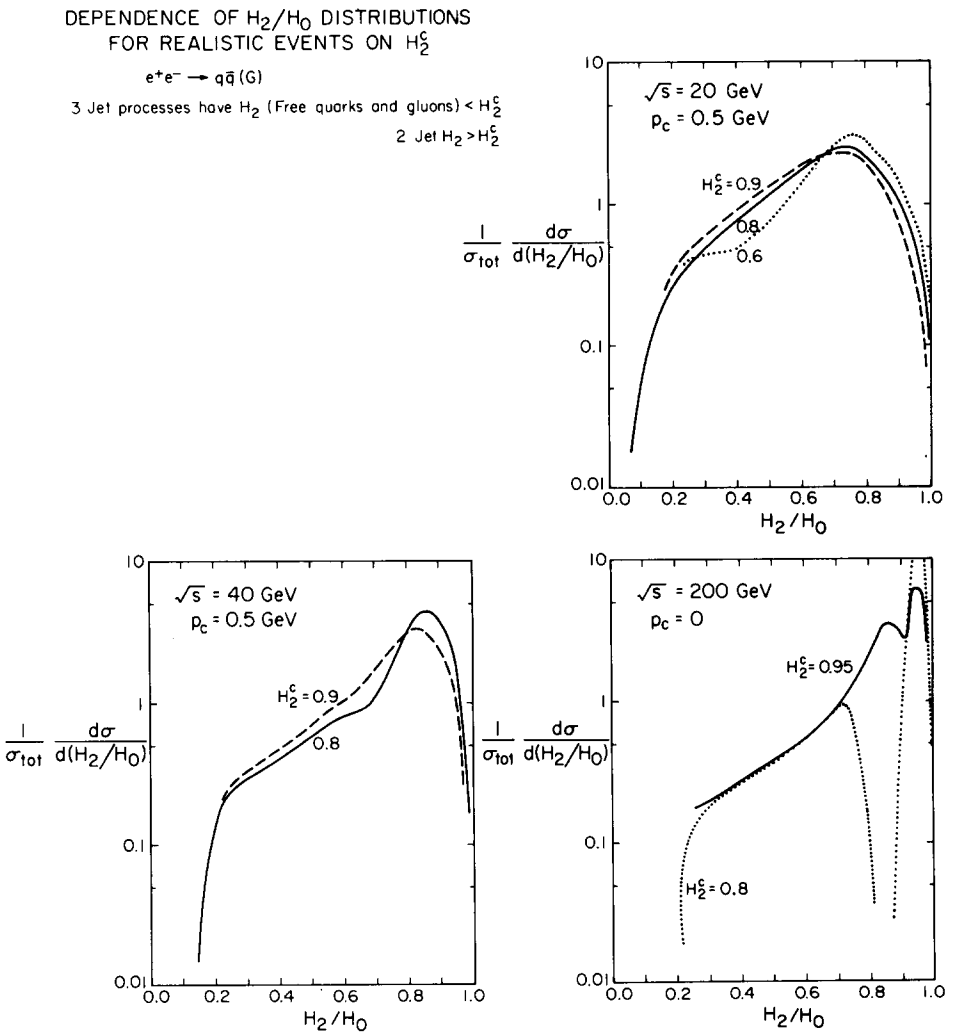

Fig. 37. The distributions $(1/\sigma_{tot})\, d\sigma/dH_2$ for hadronic events resulting from the process $e^+e^- \to q\bar{q}(G)$ for various choices of the parameter H_2^c which divides two- from three-jet final states.

'see' the arbitrary division between configurations of the quarks and gluons which are supposed to give two- and three-jet final states. If a very large value of H_2^c is chosen then negative amounts of $e^+e^- \to q\bar{q}$ have to be added in order to obtain the correct total cross section for $e^+e^- \to q\bar{q}(G)$ events, which seems undesirable.

In the Field-Feynman model for quark and gluon fragmentation, we find that, for most values of $\sqrt{s}$, the choice $H_2^c = 0.8$ avoids the pathologies mentioned above. At $\sqrt{s} = 200$ GeV, however, there is no value of H_2^c which avoids both of them. This is undoubtedly a signal of the incompatibility of the Field-Feynman model with QCD. Inclusion of the rise of $\langle k_T \rangle$ for the hadrons from quark and gluon fragmentation with increasing $\sqrt{s}$ implied by QCD would probably serve to alleviate the difficulty. We used $H_2^c = 0.95$ at $\sqrt{s} = 200$ GeV. Fig. 37 shows the dependence of $(1/\sigma_{tot})\, d\sigma/dH_2$ for $e^+e^- \to q\bar{q}(G)$ events on the choice of H_2^c. It seems clear from these results that $H_2^c = 0.8$ is adequate for predictions at c.m. energies $\sqrt{s}$ which will be attained by accelerators in the immediate future ($\sqrt{s} \lesssim 40$ GeV), and that at these energies the dependence of the results on the value of the unknown parameter H_2^c is very slight.

5.4. Results for incomplete final states

The H_l distributions for realistic hadronic events presented in sect. 4 exhibited rather large deviations from the free quark and gluon approximation. The discrepancy is, in part, due to the presence of many soft hadrons in the final state, and may be decreased by using only those particles whose momenta are above some lower cut-off p_c in the calculation of the H_l *. For sufficiently large p_c, such a cut leaves essentially only those hadrons moving along the jet direction, and removes the roughly isotropic background of low-momentum hadrons. The latter particles typically have momenta comparable with the transverse momentum of the jet fragmentation. If p_c is taken too large, however, then all the hadrons in a particular jet may be ignored, and the resulting H_l will once again not reflect the free quark and gluon results. We shall consider $p_c = 0.5$ and 1 GeV. Of course, our previous results used all the hadrons in each event, corresponding to $p_c = 0$.

Since we always work in the virtual photon rest frame, the three-momenta of all particles in an event should sum to zero, so that, for each event, $H_1 = 0$. In addition, if all hadrons in an event are massless, then energy conservation requires that $H_0 = 1$. The non-zero masses of the final hadrons serve to decrease the value of H_0 from one. The effect is small, and in the results of sect. 4 we always removed it by dividing H_l by H_0 for each event. We followed the same procedure when considering incomplete final states. Here the deviation of H_0 from 1 was, of course, much larger. The

* Note that the arguments for infrared stability of processes involving only quarks and gluons discussed in sect. 3 do not apply when only charged particles or particles with momenta above some lower cut-off p_c are considered. Cuts on hadronic final states cannot, however, be related directly to those on their quark-gluon parent states.

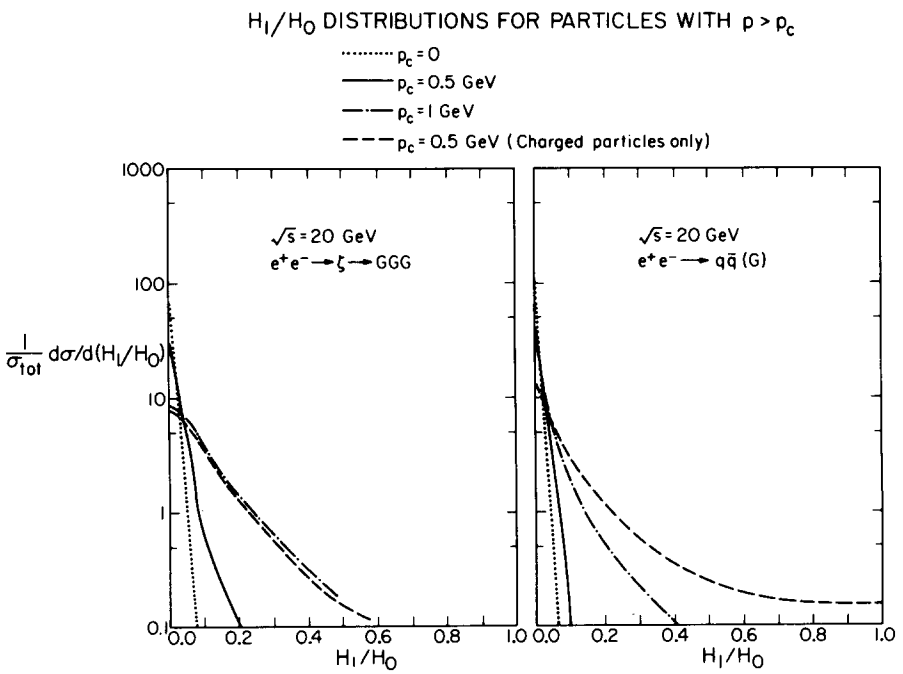

Fig. 38. The distributions $(1/\sigma_{tot})\, d\sigma/d(H_1/H_0)$ for simulated hadronic final states computed using only hadrons with momenta greater than p_c. The non-zero values of H_1/H_0 even when all hadrons in each event are included are a reflection of the fact that the model for jet fragmentation used does not conserve momentum exactly. In one of the curves, only the charged particles in each event have been used for the calculation of H_1.

total momentum measured in an 'incomplete' event will also be non-zero, so that $H_1/H_0 \neq 0$. Fig. 38 shows the distributions $(1/\sigma_{tot})\, d\sigma/d(H_1/H_0)$ for $e^+e^- \to q\bar{q}(G)$ and $e^+e^- \to \zeta \to GGG$ events at $\sqrt{s} = 20$ GeV, with various choices for p_c. $p_c = 0$ corresponds to measuring all particles in each event. That H_1/H_0 is not always zero even in this case is a reflection of the fact that the model we use to generate final states does not conserve momentum exactly. The narrowness of distribution in H_1/H_0 for this case shows that the discrepancy is, in fact, very small.

Fig. 39 shows the H_2/H_0 distributions for hadronic events resulting from the processes $e^+e^- \to q\bar{q}$, $e^+e^- \to q\bar{q}(G)$ and $e^+e^- \to \zeta \to GGG$ computed using only hadrons with momenta greater than p_c in each event. Note that larger values of p_c improve the agreement between the results for realistic hadronic final states and those obtained using the approximation of free quarks and gluons. However, if p_c is increased significantly above 1 GeV at $\sqrt{s} = 20$ GeV, the agreement begins to deteriorate again; the apparent values of H_l in some events are too small because all the particles in a jet have momenta below the cut-off p_c. In no case does the use of a momentum cut significantly improve the discrimination between different between different types of hadronic events provided by the H_l; it merely serves to make some

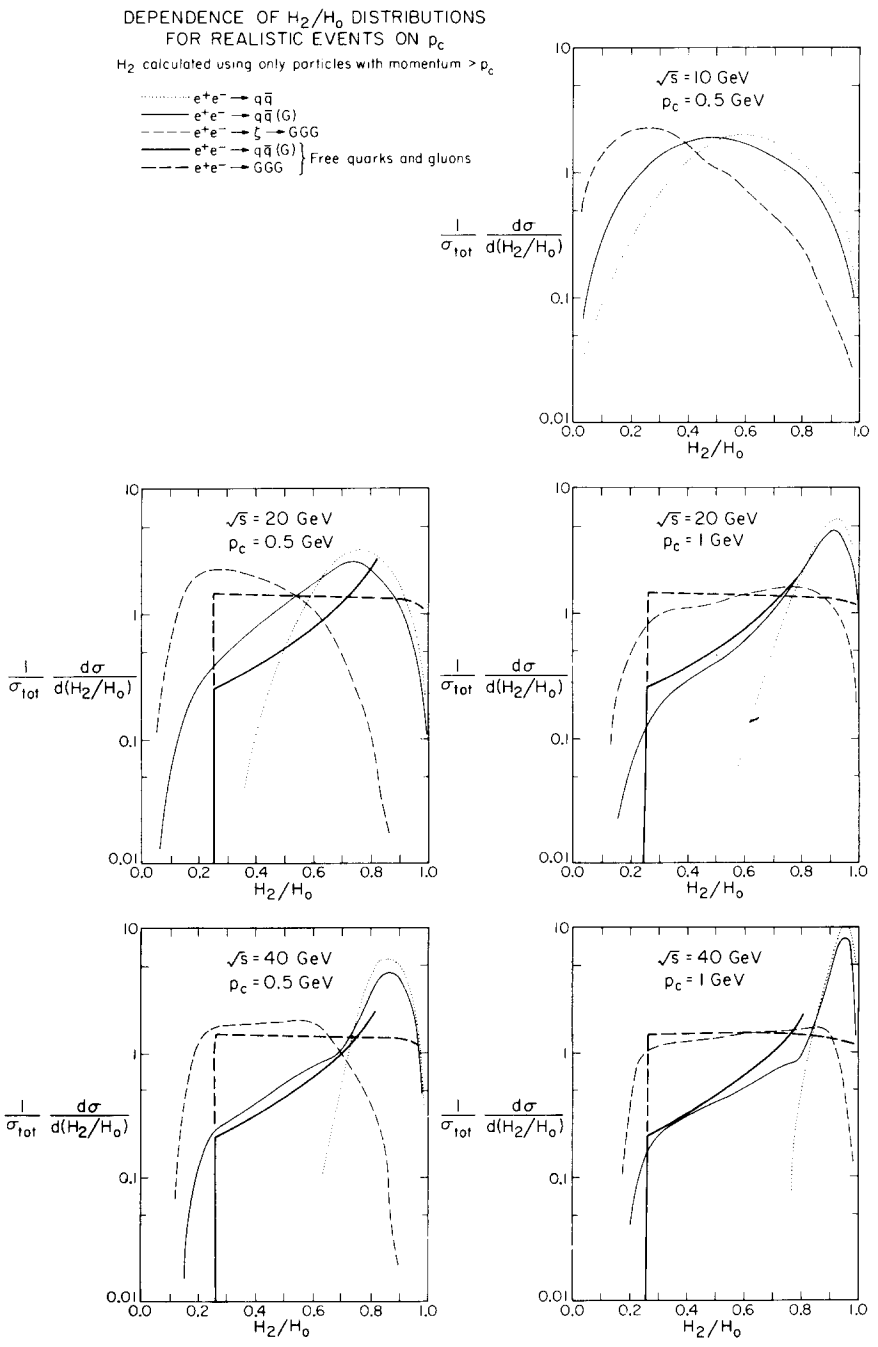

Fig. 39. The distributions $(1/\sigma_{tot})\, d\sigma/d(H_2/H_0)$ for simulated hadronic events calculated using only hadrons with momenta greater than p_c.

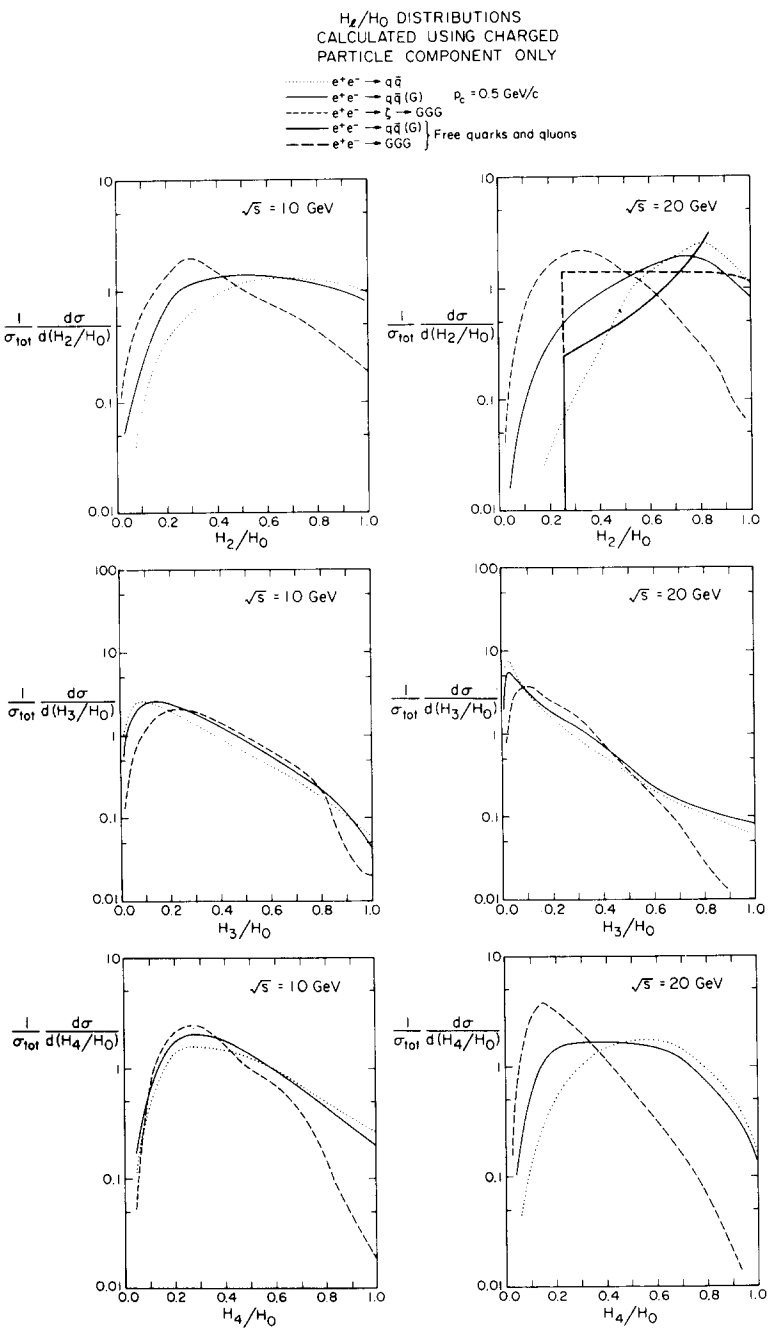

Fig. 40. The distributions $(1/\sigma_{tot})\, d\sigma/d(H_2/H_0)$, $(1/\sigma_{tot})\, d\sigma/d(H_3/H_0)$ and $(1/\sigma_{tot})\, d\sigma/d(H_4/H_0)$ for simulated hadronic events calculated using only charged hadrons.

of the distributions more similar to those obtained in the free quark and gluon approximation. These trends are reflected in the values of $\langle H_2/H_0 \rangle$, $\langle H_3/H_0 \rangle$ and $\langle H_4/H_0 \rangle$ given in table 7.

In actual experiments, not all the hadrons in each event will usually be detected. Some will be lost through imperfect angular acceptance, while others will simply not trigger the detectors. Note that the rotational invariance of the H_l renders them independent of the orientation of events, so that their values should be insensitive to gaps in angular acceptance. As an illustration of the consequences of these effects, we show in fig. 40 the distributions in H_2/H_0, H_3/H_0 and H_4/H_0 for hadronic events at $\sqrt{s}$ = 10 and 20 GeV calculated using only the charged hadrons in the final state. The discrimination between different processes provided by the H_l is not unduly affected by this cut. The enhancement of events at larger H_l if only charged particles are considered is a consequence of the large apparent violations of momentum conservation in this case. This phenomenon is reflected in the very broad H_1/H_0 distribution for these events shown in fig. 37. This artificial behaviour can be removed by considering only events with (charged) multiplicity greater than 3.[17,29]. Many of the new generation of detectors can measure neutral particles, and so will not encounter these problems. Of course, we cannot estimate the H_l distributions which should be observed by actual experiments; that would require a knowledge of the details of the apparatus used.

It is possible that cuts other than on hadron momenta may serve to 'clean up' the H_l distributions. For example, one might consider only events with a certain range of total multiplicities.

5.5. Heavy quark and lepton production

In this subsection, we present results for realistic events involving the production and decay of pairs of heavy quarks and leptons. We use the models for these processes discussed in subsect. 4.5, which are adequate only close to threshold.

Fig. 41 shows the fractional momentum (z) distributions for single hadrons from events involving heavy quark or lepton production (at $\sqrt{s}$ = 20 GeV). The distributions are all very similar, but are much softer than those for events of the $e^+e^- \to q\bar{q}(G)$ type.

Figs. 42–44 show the distributions $(1/\sigma_{tot})\, d\sigma/d(H_l/H_0)$ for realistic hadronic final states resulting from the production and decay of heavy quarks and leptons, and table 8 gives the $\langle H_l/H_0 \rangle$ for these processes at various c.m. energies. The fact that our models for heavy quark and lepton decay give rise to many jets of hadrons means that higher c.m. energies than for two- or three-jet production are necessary to obtain well-collimated jets, or for the H_l distributions for realistic hadronic events to approach the free quark and gluon approximation. The decays of heavy quark and lepton pairs into four hadronic jets give similar H_2/H_0 and H_4/H_0 distributions, but the heavy lepton gives a significantly harder H_3/H_0 distribution. The different mechanisms for heavy quark decay give slightly different H_l/H_0 distributions, even at $\sqrt{s}$ = 10 GeV, and it seems, therefore, that an analysis based on the H_l should be

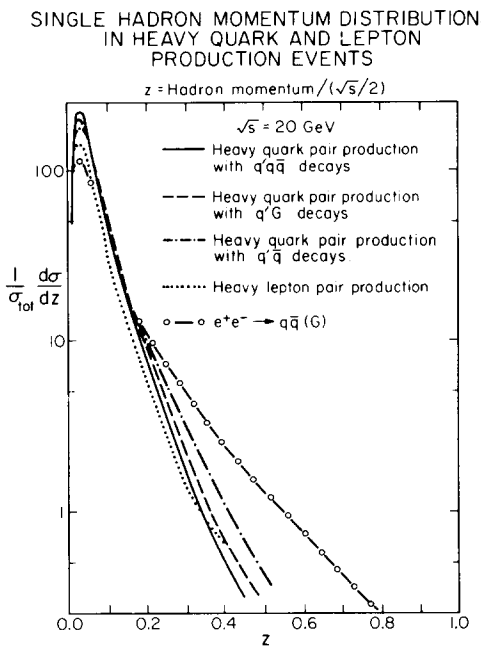

Fig. 41. Single hadron fractional momentum (z) distributions for simulated hadronic events involving the production and decay of heavy quarks and leptons, according to the models discussed in subsect. 4.5.

able to give some indication as to the mechanism for the weak decay of mesons with masses around 5 GeV. Mesons containing b quarks should have masses in this region, and it seems probable that they will decay through weak interactions.

At $\sqrt{s}$ = 20 GeV, the two-jet mechanisms for heavy quark decay give rise to definitely harder H_2 and H_4 distributions than the three-jet mechanism. In addition, because (in our model) quark jets are better collimated than gluon jets the $q\bar{q}$ decay mode gives a harder H_2 distribution than the qG mode.

Finally, at $\sqrt{s}$ = 200 GeV, the distributions for realistic hadronic events become very similar to those obtained in the free quark and gluon approximation (fig. 30), although they remain somewhat softer at large H_l. This is due to the large number of jets produced in each event; even at $\sqrt{s}$ = 200 GeV each jet does not have sufficient energy to appear like a free quark or gluon.

5.6. *The H_l for large l*

The forms of the H_l distributions for high l in the free quark and gluon approximation for the processes $e^+e^- \to q\bar{q}(G)$ and $e^+e^- \to \zeta \to GGG$ were presented in fig. 23. The $\langle H_l \rangle$ in these cases were given in table 6. In fig. 45, we plot the $\langle H_l \rangle$ for realistic hadronic events resulting from the processes $e^+e^- \to q\bar{q}$, $e^+e^- \to q\bar{q}(G)$ and $e^+e^- \to \zeta \to GGG$ for the range of c.m. energies which will be attained by the next

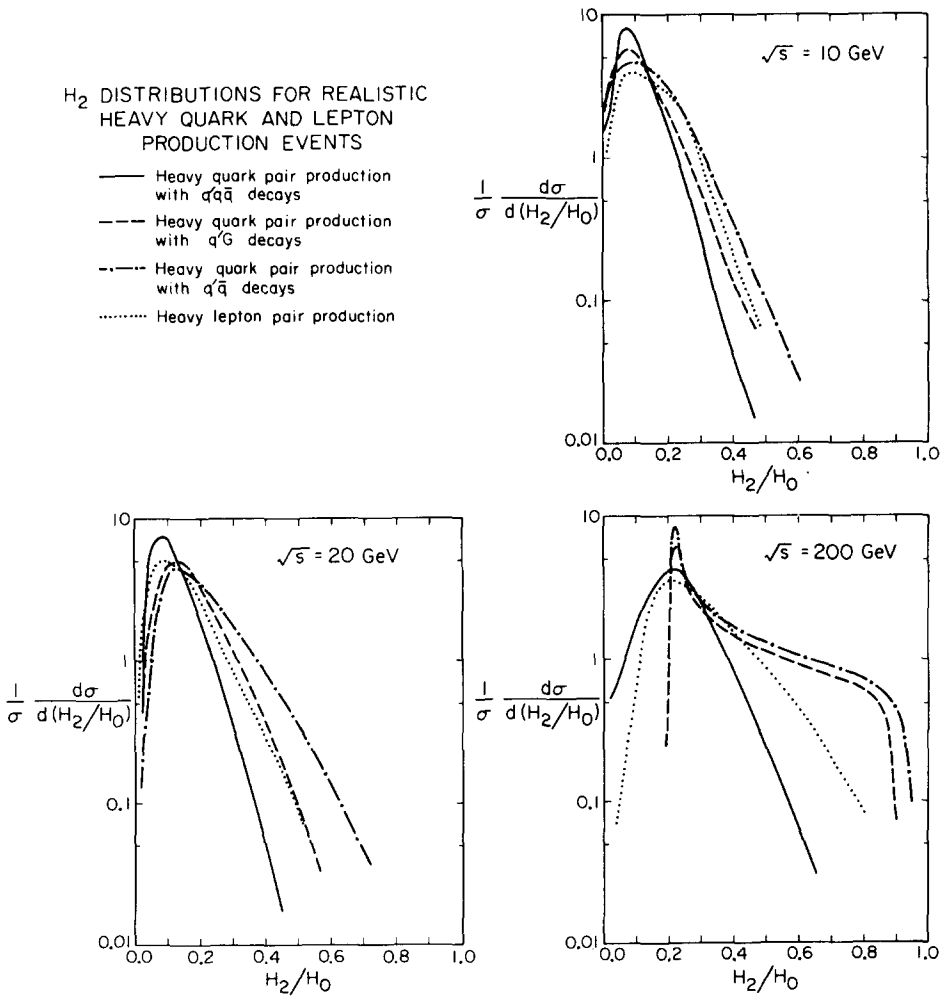

Fig. 42. The distributions $(1/\sigma_{tot})\, d\sigma/d(H_2/H_0)$ for simulated hadronic events involving the production and decay of heavy quarks and leptons.

generation of e^+e^- accelerators. It is clear that the power of the $\langle H_l \rangle$ to discriminate between the various processes diminishes as l increases. For large l, the H_l reflect only the small-scale angular structure of each event, which is determined more by the structure of the hadron jets than by the nature of the subprocess. Note also that the approach of the $\langle H_l \rangle$ for realistic hadronic events to the $\langle H_l \rangle$ obtained in the free quark and gluon approximation is less rapid for high l. Little new information may be gleaned from a measurement of the H_l for high l, and we believe that an experi-

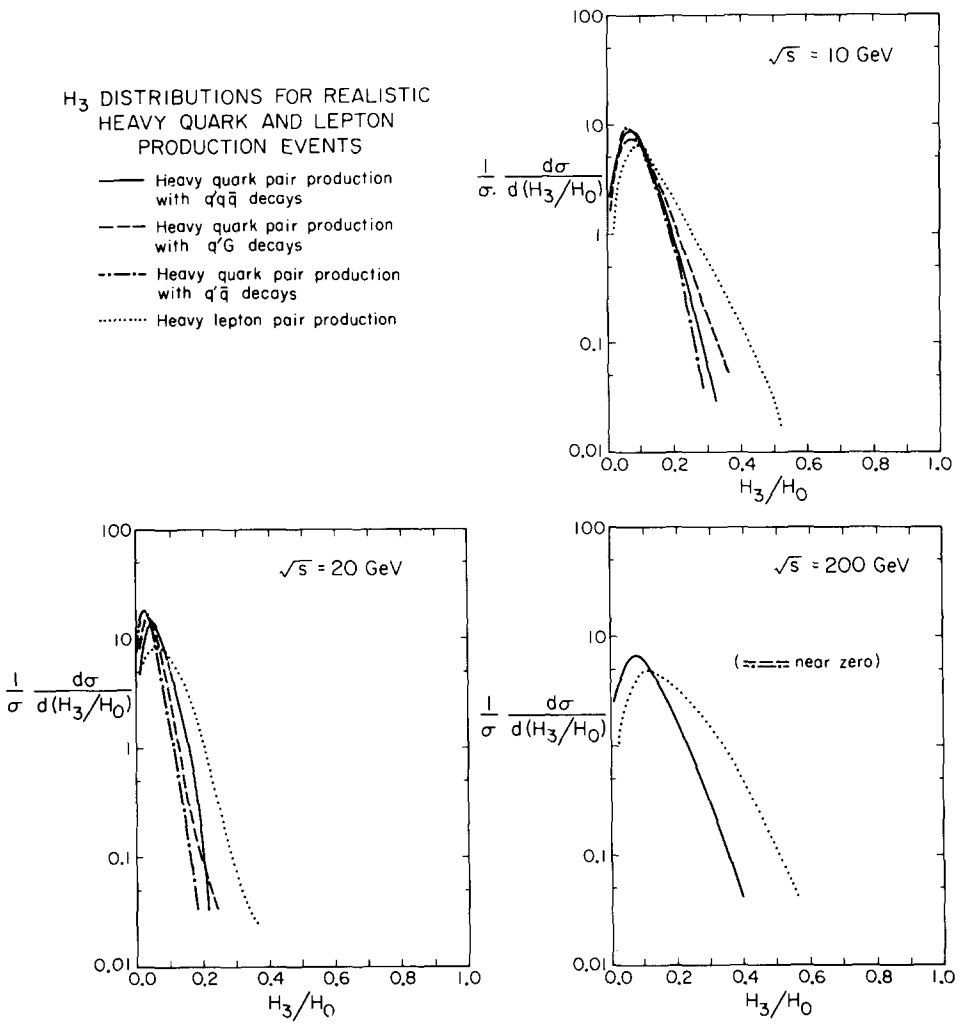

Fig. 43. The distributions $(1/\sigma_{tot})\, d\sigma/d(H_3/H_0)$ for simulated hadronic events involving the production and decay of heavy quarks and leptons.

mental measurement of the distributions in H_2 and H_3 should be sufficient. The $\langle H_l \rangle$ clearly have less power to discriminate between different types of events than do the complete distributions in the H_l.

From the $\langle H_l \rangle$ for realistic events, one may in principle construct an average 'correlation function' $F(x)$ (see sect. 2), using the series formula (2.10). Fig. 46 shows the $F(x)$ computed from the $\langle H_l \rangle$ for realistic events of various types at

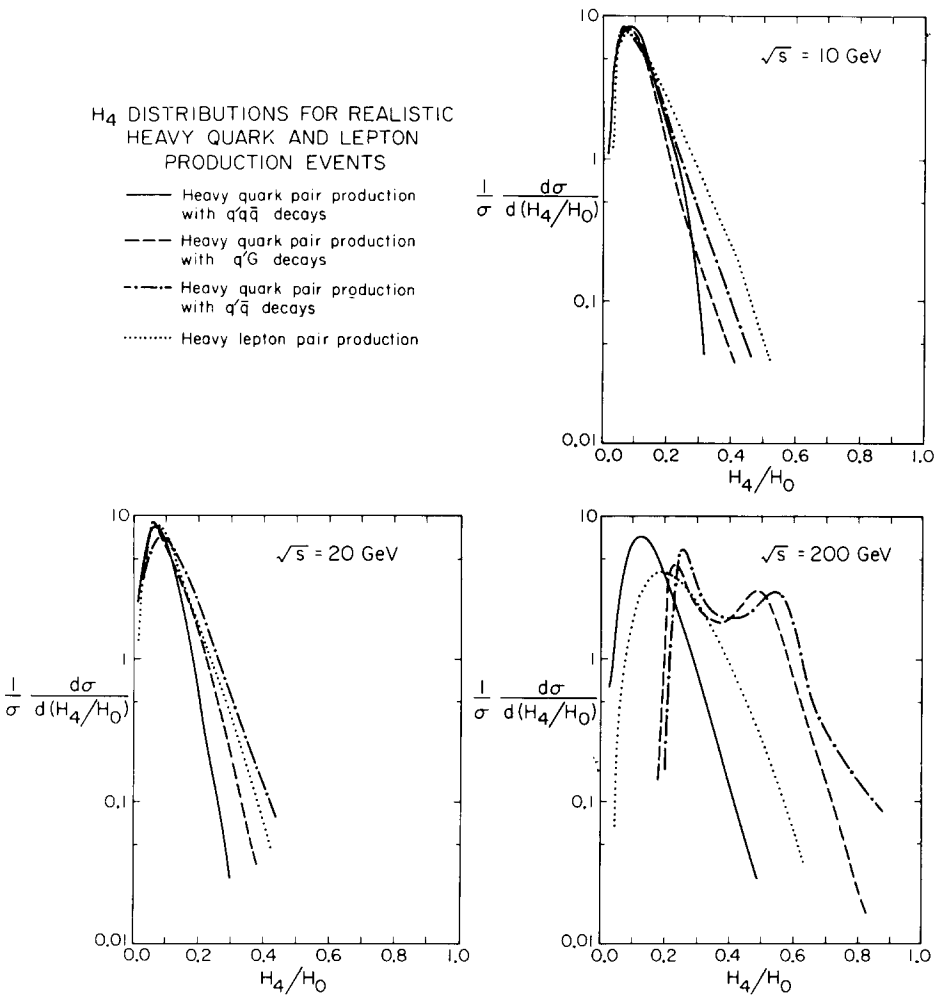

Fig. 44. The distributions $(1/\sigma_{tot})\, d\sigma/d(H_4/H_0)$ for simulated hadronic events involving the production and decay of heavy quarks and leptons.

$\sqrt{s} = 10$ GeV. For most of the curves, the series (2.10) was truncated at $l = 10$, but for $e^+e^- \to q\bar{q}$ events, we also show the form for $F(x)$ obtained by truncating the series at $l = 5$. The two results differ significantly, illustrating the very slow convergence of the series for $F(x)$. Note that $F(x)$ cannot be computed directly from real events, as the formula (2.7) involves products of delta functions. Rather, one must find the function F_2 (defined in eq. (2.22)) for some small, but finite,

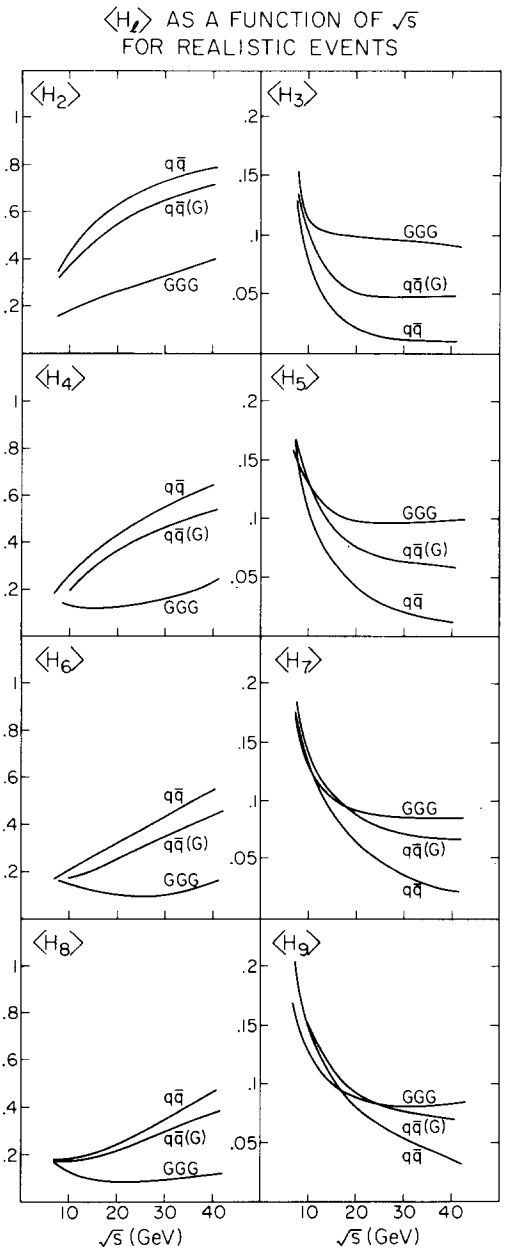

Fig. 45. The mean values of the H_l for realistic two- and three-jet events as a function of the c.m. energy $\sqrt{s}$ over the range accessible to the next generation of e^+e^- accelerators.

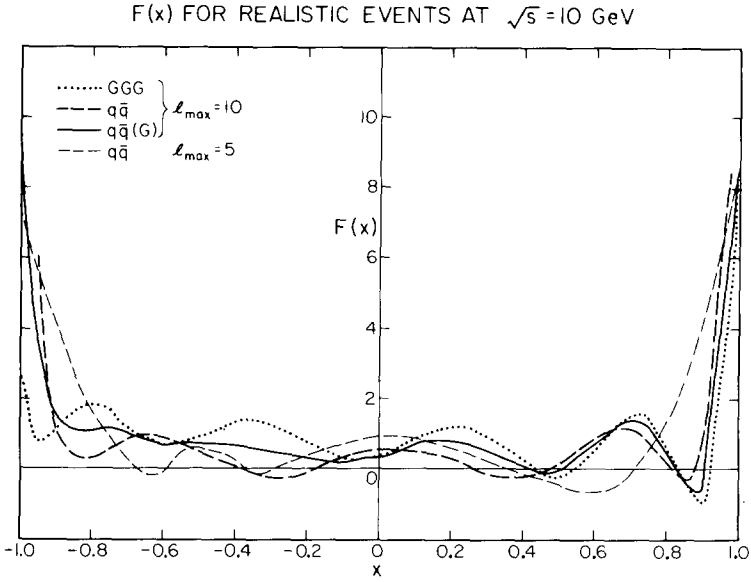

Fig. 46. The form for the 'correlation function' $F(x)$ calculated from the $\langle H_l \rangle$ for realistic two- and three-jet events at $\sqrt{s}$ = 10 GeV using the series (2.10). The series was truncated at $l = l_{max}$.

Table 8
Averages values of H_l/H_0 for realistic hadronic events resulting from heavy quark and lepton production and decay by the various mechanisms discussed in subsect. 4.5

$\sqrt{s}$ (GeV)	$\langle H_2/H_0 \rangle$			
	$qq\bar{q}\bar{q}\bar{q}q$	$qG\bar{q}G$	$q\bar{q}\bar{q}q$	$q\bar{q}(\nu)\,\bar{q}q(\nu)$
10	0.12	0.13	0.16	0.16
20	0.12	0.18	0.23	0.16
200	0.26	0.43	0.45	0.32
∞	0.28	0.50	0.50	0.35
$\sqrt{s}$ (GeV)	$\langle H_3/H_0 \rangle$			
	$qq\bar{q}\bar{q}\bar{q}q$	$qG\bar{q}G$	$q\bar{q}\bar{q}q$	$q\bar{q}(\nu)\,\bar{q}q(\nu)$
10	0.11	0.10	0.09	0.14
20	0.06	0.05	0.04	0.10
200	0.10	0.001	0.001	0.19
∞	0.13	0	0	0.23
$\sqrt{s}$ (GeV)	$\langle H_4/H_0 \rangle$			
	$qq\bar{q}\bar{q}\bar{q}q$	$qG\bar{q}G$	$q\bar{q}\bar{q}q$	$q\bar{q}(\nu)\,\bar{q}q(\nu)$
10	0.11	0.11	0.11	0.15
20	0.08	0.11	0.14	0.12
200	0.17	0.39	0.42	0.25
∞	0.21	0.50	0.50	0.30

detector size $|\sigma_i|$. This indicates that although in principle the H_l and $F(x)$ contain the same information (see subsect. 2.1), in practice they are not equivalent.

6. Harmonics about the beam axis

Most of this paper has been concerned with the analysis of the 'shapes' of final states in e^+e^- annihilation using observables which do not require a definite axis for their evaluation. The incoming beams provide, however, a natural axis for the analysis of the 'shape' of the final state. Nevertheless, we shall see that there is often insufficient correlation between the beam axis and the configuration of the final state to make such an analysis useful.

Define

$$B_l \equiv \sum_i \frac{|p_i|}{\sqrt{s}} P_l(\cos\alpha_i) , \tag{6.1}$$

where α_i is the angle that the final state particle i makes with the direction of the incoming electron. Energy-momentum conservation requires

$$\begin{aligned} B_0 &= \sqrt{H_0} = 1 , \\ B_1 &= 0 , \end{aligned} \tag{6.2}$$

if all the particles are massless. If the incoming beams are unpolarized, then all parity-conserving processes give

$$\langle B_l \rangle = 0 , \qquad (l \text{ odd}) , \tag{6.3}$$

and kinematics require that

$$P_{2l}(0) \leqslant B_{2l} \leqslant 1 . \tag{6.4}$$

The process $e^+e^- \to q\bar{q}$ illustrated in fig. 1 has

$$\frac{1}{\sigma}\frac{d\sigma}{d(\cos\alpha_i)\, dx_i} = \tfrac{3}{8}(1 + \cos^2\alpha_i)\,\delta(x_i - 1) , \qquad (i = 1, 2) , \tag{6.5}$$

yielding

$$\begin{aligned} \langle B_2 \rangle &= \tfrac{1}{10} , \\ \langle B_l \rangle &= 0 , \qquad (l > 2) . \end{aligned} \tag{6.6}$$

Data on angular distributions of two-jet final states in e^+e^- annihilation are often given in terms of the parameter λ, defined by

$$\left.\frac{1}{\sigma}\frac{d\sigma}{d(\cos\alpha_i)\, dx_i}\right|_{\text{jets}} = \frac{3}{2(\lambda + 3)}(1 + \lambda\cos^2\alpha_i)\,\delta(x_i - 1) , \qquad (i = 1, 2) . \tag{6.7}$$

In this case,

$$\langle B_2 \rangle = \frac{2\lambda}{5(\lambda+3)}, \qquad \langle B_l \rangle = 0, \quad (l > 2), \tag{6.8}$$

so that λ may be expressed in terms of the $\langle B_l \rangle$ as

$$\lambda = \frac{15\langle B_2 \rangle}{2 - 5\langle B_2 \rangle}. \tag{6.9}$$

Note that for pairs of particles produced at rest, $\lambda = 0$, so that $\langle B_2 \rangle = 0$. This effect may serve as a method for detecting the presence of heavy quark or lepton production near threshold (see below).

The differential cross section for $e^+e^- \to q\bar{q}$ in B_2 is given by

$$\frac{1}{\sigma}\frac{d\sigma}{dB_2} = \frac{\sqrt{3}(B_2+2)}{6\sqrt{1+2B_2}}. \tag{6.10}$$

Kinematics require that for any process

$$-\tfrac{1}{2} \leqslant B_2 \leqslant 1. \tag{6.11}$$

The divergence in $(1/\sigma)\, d\sigma/dB_2$ for $e^+e^- \to q\bar{q}$ at the edge of the physical region ($B_2 = -\frac{1}{2}$) is introduced by the Jacobian of the transformation from $\cos\alpha$ to B_2. The differential cross section (6.10) is plotted in fig. 47. We also show there the

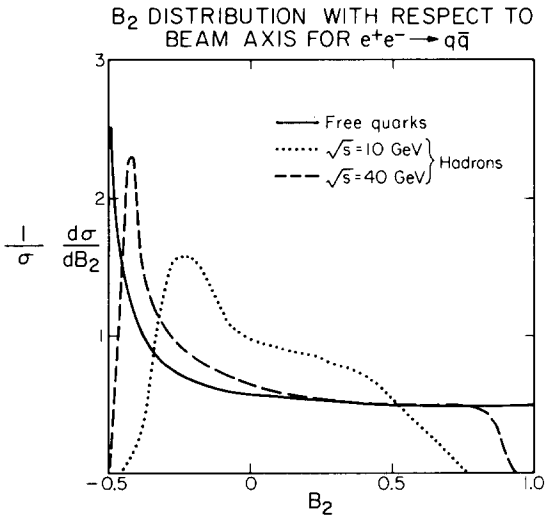

Fig. 47. The distributions in the beam moment B_2 for events arising from the process $e^+e^- \to q\bar{q}$.

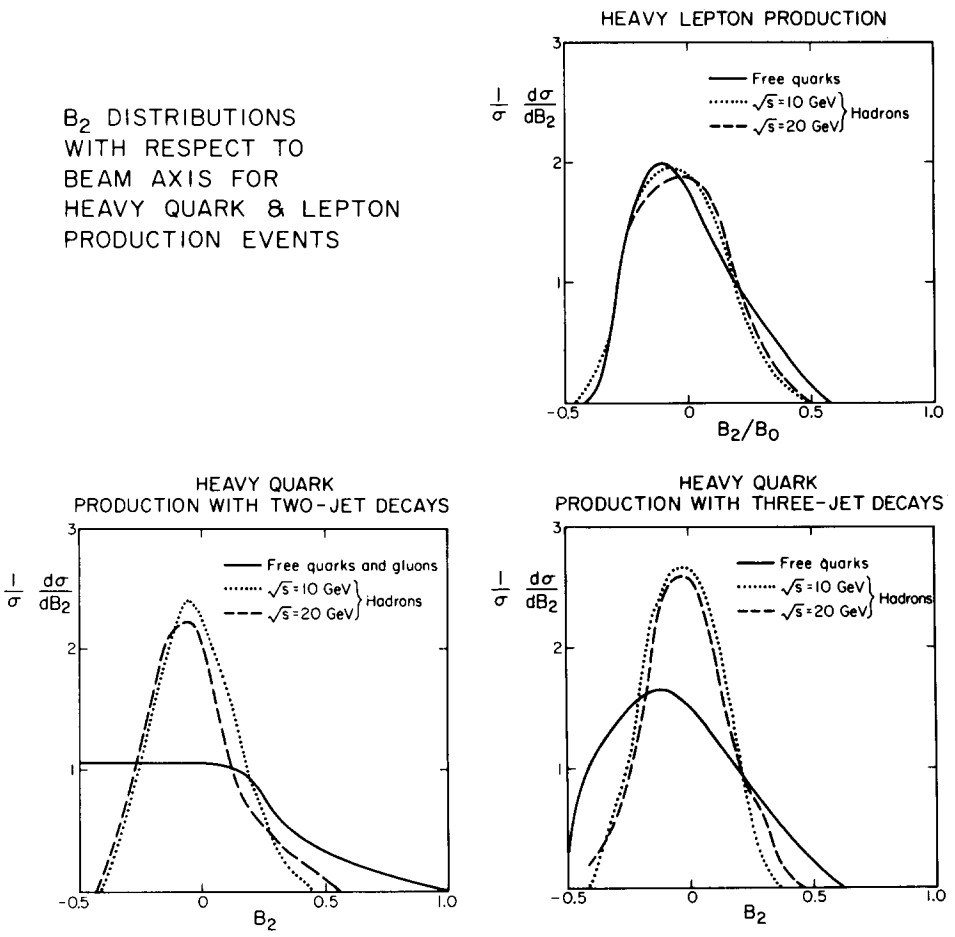

Fig. 48. The distributions in the beam moment B_2 for events involving the production and decay of heavy quarks and leptons.

forms for $(1/\sigma)\, d\sigma/dB_2$ resulting from the process $e^+e^- \to q\bar{q} \to$ hadrons, using the model for quark fragmentation described in sect. 5. A significant sharpening of the distribution may be observed for $\sqrt{s} = 40$ GeV as compared to $\sqrt{s} = 10$ GeV. The mean values of B_2 deduced from these distributions and for various other cases are given in table 9. None differ by more than about 0.04 from the free quark approximation value of 0.1.

Fig. 48 shows the distributions $(1/\sigma)\, d\sigma/dB_2$ due to the production and decay of heavy quarks and leptons, through the mechanisms discussed in subsect. 4.5. Clearly near the thresholds for these processes $\langle B_2 \rangle \simeq 0$. The production and decay of pairs of heavy spin-0 mesons always give $\langle B_2 \rangle = 0$, but production and weak decays of high-energy heavy leptons or quarks could yield non-zero values of $\langle B_2 \rangle$. This result is essentially unchanged by allowing the quarks and gluons generated in the

Table 9
Average values of B_2/B_0 for realistic hadronic events resulting from the process $e^+e^- \to q\bar{q}$: only hadrons with momenta larger than p_c are used in each computation of $\langle B_2/B_0 \rangle$

$\sqrt{s}$ (GeV)		$\langle B_2/B_0 \rangle$
3	$p_c = 0$	0.02
6	$p_c = 0$	0.05
10	$p_c = 0$	0.06
10	$p_c = 0.5$	0.07
10	$p_c = 0.5$ (charged only)	0.09
20	$p_c = 0$	0.07
20	$p_c = 0.5$ (charged only)	0.08
40	$p_c = 0$	0.07
40	$p_c = 0.5$	0.11
200	$p_c = 0$	0.09
∞		0.10

weak decays to fragment into hadrons. The distributions $(1/\sigma)\, d\sigma/dB_2$ for this case are shown in fig. 48 for various values of $\sqrt{s}$, using the models described in subsect. 4.5. The approximately Gaussian shapes of many of the distributions are a simple consequence of the central limit theorem. Away from the kinematic boundary $B_2 = -\frac{1}{2}$, the probability that a given particle has a particular value of B_2 is roughly uniform in B_2, and the values of B_2 for each of the particles are essentially uncorrelated. The B_2 for the complete event is a sum of the B_2 values for each of the particles, so that, at least away from $B_2 = -\frac{1}{2}$, it will be approximately normally distributed. The distribution is closer to Gaussian if 3-jet heavy quark decays are assumed rather than 2-jet ones. The difference between the value of $\langle B_2 \rangle$ for two-jet ($e^+e^- \to q\bar{q} \to$ hadrons) events ($\langle B_2 \rangle \simeq 0.1$) and for heavy quark or lepton production ($\langle B_2 \rangle = \simeq 0$) may allow the two processes to be distinguished by a measurement of $\langle B_2 \rangle$. (A similar method is proposed in ref. [20].) In addition, the distributions $(1/\sigma)\, d\sigma/dB_2$ for the processes are somewhat different (see figs. 47 and 48).
For the process $e^+e^- \to q\bar{q}(G)$, one finds that *

$$\langle B_2 \rangle = \frac{1}{10} + \frac{2\alpha_s}{3\pi} \int \frac{3(1-x_3)(x_1^2 + x_2^2 - 2(x_1 + x_2))}{10 x_1 x_2 x_3}\, dx_1\, dx_2$$
$$= \frac{1}{10} - \frac{3\alpha_s(s)}{10\pi}, \qquad (6.12)$$

* In this calculation we used the differential cross section for $e^+e^- \to q\bar{q}G$ [3] (1 = q, 2 = $\bar{q}$):

$$\frac{d\sigma}{dx_1\, dx_2\, d(\cos\theta)\, d\phi} = \frac{\alpha_s}{8\pi^2} \left[\frac{x_1^2(1 + \sin^2\theta \cos^2\phi_1) + x_2^2(1 + \sin^2\theta \cos^2\phi_2)}{(1-x_1)(1-x_2)} \right].$$

Integration over angles gives a term identical to the total cross section for $e^+e^- \to q\bar{q}G$ (multiplied by $\frac{1}{10}$) plus the term given as the integrand in eq. (6.12).

so that the angular distribution parameter defined in eq. (6.7) is given by

$$\lambda \simeq 1 - \frac{4\alpha_s(s)}{\pi} . \tag{6.13}$$

For $\sqrt{s}$ = 10 GeV, this gives

$$\langle B_2 \rangle \simeq 0.076 , \qquad \lambda \simeq 0.68 . \tag{6.14}$$

On comparing $\langle B_2 \rangle$ from eq. (6.14) with the results for $e^+e^- \to q\bar{q}$ in table 9, it becomes clear that it would be very difficult to distinguish between $e^+e^- \to q\bar{q}$ and $e^+e^- \to q\bar{q}(G)$ events by a measurement of $\langle B_2 \rangle$. Whereas two- and three-jet processes populate different regions in the H_l (see, for example, fig. 30), both populate the complete range of B_l. Hence, even a measurement of the distributions in the B_l will probably not be very effective at identifying two- and three-jet processes. In fact, the B_2 distributions for $e^+e^- \to q\bar{q}G$ and $e^+e^- \to q\bar{q}$ are very similar. For the former there is a slight depletion of events near the boundaries. The detailed results depend sensitively however on the treatment of three-jet fragmentation. Note that, because the photon has spin 1, $\langle B_l \rangle = 0$ for $l > 2$ even for three-jet processes.

The process $e^+e^- \to \zeta \to GGG$ is also amenable to analysis in terms of the B_l. If one assumes that the ζ is a pure s-wave state and contains no d-wave admixture, then the helicity amplitudes for the Q and $\bar{Q}$ within the ζ are determined simply by those of the virtual photon. It is, therefore, possible to compute the angular distribution of the gluons produced in the process of fig. 3 with respect to the beam axis. Using the results of ref. [30], we find that in this case

$$\langle B_2 \rangle = \frac{72 - 7\pi^2}{80(\pi^2 - 9)} \simeq 0.042 , \tag{6.15}$$

corresponding to

$$\lambda = \frac{72 - 7\pi^2}{13\pi^2 - 120} \simeq 0.35 . \tag{6.16}$$

The distribution in B_2 for $e^+e^- \to \zeta \to GGG$ is rather smooth, having no peak around $B_2 = -\frac{1}{2}$, and goes to zero as $B_2 \to 1$.

From the arguments made for the H_l in sect. 3, it is clear that the moments of the B_l should also be infrared finite to all orders in QCD perturbation theory. Since the angular distribution of energy produced in e^+e^- annihilation events is entirely determined by $\langle B_0 \rangle$ and $\langle B_2 \rangle$, it too must be infrared finite to all orders in g^2. The average energy angular distribution for $e^+e^- \to q\bar{q}(G)$ to $O(g^2)$ is calculated in ref. [27]. Because this may be expressed as a finite sum of B_l, it should be infrared stable, unlike $F(x)$, which is given only by an infinite sum of H_l. Note, however, that by considering only such an average angular distribution, one loses the information provided by the distribution of events in the B_l.

7. Application to deep inelastic scattering

In this section, we discuss the use of the H_l in the analysis of three-jet effects in deep inelastic lepton-nucleon (μN, eN and νN) interactions. We work mainly in the rest frame of the incoming virtual photon (or W) and the target nucleon. The γ^* (or W^*) is taken to have an energy ν in the rest frame of the target nucleon, and an invariant mass $-Q^2$. Bjorken's x variable is defined as $x = Q^2/2m_N\nu$.

The lowest-order process in deep inelastic lepton-nucleon scattering is the absorption of the virtual photon by a quark in the proton. The final state will contain two jets of hadrons; one arising from the quark and one from the fragmentation of the target nucleon. If the remnants of the target nucleon are treated as a single point particle then two-jet final states from deep inelastic scattering give the same values of the H_l as two-jet final states in e^+e^- annihilation. (The H_l are normalized so that $H_0 = 1$.) A cut may be made on the hadrons in the final state which ensures that few of those considered were fragments of the target, rather than of the produced quark. The requirement that all hadrons considered have momenta directed into the hemisphere ahead of the virtual photon (or W) direction (that is, all have $z > 0$) seems sufficient to veto most target fragments. In this case, only the fragments of the outgoing quark should contribute to the values of the H_l for the final state. Ignoring the fragmentation of the quark into hadrons, one finds that in this case all the H_l are simply equal to $\frac{1}{4}$. Three-jet final states (which arise from the processes $\gamma^* q \to qG$ and $\gamma^* G \to q\bar{q}$) will give a distribution of values of H_l. Unfortunately, the $z > 0$ cut on final particles may not lead to infrared stable results, so that it may not be possible to make reliable predictions for the H_l distributions in this case.

A closer analogy to e^+e^- annihilation is obtained if all the particles in the final state are considered. Let us assume that the fragments of the target may be treated as a single massless particle (perhaps akin to a 'diquark'). Then in the free massless quark approximation, the H_l for two-jet final states will be the same as for $q\bar{q}$ final states in e^+e^- annihilation; $H_l = 1$ for even l and $H_l = 0$ for odd l. This result holds only in the $\gamma^*(W^*)$ N rest frame. Note that because the H_l are rotationally invariant, their values are unaffected by the transverse momentum of the incoming quark or gluon with respect to its parent nucleon. Three-jet final states will again give a distribution of values of H_l. The distributions are qualitatively similar to those found in sects. 4 and 5 for e^+e^- annihilation. The details of the distributions depend on the momenta of the incoming and outgoing leptons (i.e., on Q^2, x and which of W_1, W_2 or W_3 is probed). The distributions also depend on the momentum distributions of quarks and gluons in the nucleon. As x tends to one, the H_l distributions tend to a non-trivial limit with means that are typically,

$$\langle H_2 \rangle \simeq 1 - 0.9\,\alpha_s(Q^2)\,, \qquad \langle H_3 \rangle \simeq 0.3\,\alpha_s(Q^2)\,, \tag{7.1}$$

very nearly equal to the $e^+e^- \to q\bar{q}(G)$ values quoted in table 6. Such a non-zero limit should be contrasted with other QCD effects in deep inelastic scattering (for example, the $O(g^2)$ contribution to $R = \sigma_L/\sigma_T$) which vanish like $(1 - x)$ as $x \to 1$.

For small values of x, the H_l distributions become more peaked towards the two-jet values, and, for example, at $x = 0.1$,

$$\langle H_2 \rangle \simeq 1 - 0.5\,\alpha_s(Q^2)\,, \qquad \langle H_3 \rangle \simeq 0.1\,\alpha_s(Q^2)\,. \tag{7.2}$$

The dominant contribution to these results comes from the process $\gamma^* q \to q(G)$; $\gamma^* G \to q\bar{q}$ is insignificant. Only transverse photons give significant contributions to the $\langle H_l \rangle$.

In deep inelastic scattering, the question of infrared stability is more complicated than in e^+e^- annihilation because the initial quark state is no longer a color singlet. As expected from the KLN theorem, infrared finite results are obtained only if all processes at $O(g^2)$ are added, including those containing extra particles in the *initial* state (e.g., $\gamma^* Gq \to q$). At $O(g^2)$, only $\gamma^* q \to qG$ and $\gamma^* G \to q\bar{q}$ can give 3-jet final states. For odd l, the H_l receive contributions only from 3-jet final states, and so their values are unaffected by the existence of many possible two-jet processes, while for even l the H_l contain an extra term which gives the total cross section upon integration over all possible final states. When this result is divided by the total cross section in order to obtain $\langle H_l \rangle$, the extra term becomes simply $1 + O(g^4)$. Thus, to order g^2 a knowledge of the total cross section is not necessary to obtain the $\langle H_l \rangle$.

In the results quoted above, we have assumed idealized jets, and have not included fragmentation into hadrons. This can be treated by the methods described in sect. 5. Note that the effects of hadron fragmentation will be characterized by the $\gamma^* N$ c.m. energy $\sqrt{s} = Q\sqrt{(1/x) - 1}$. As mentioned above, the H_l distributions for three-jet events become more distinct from the two-jet limit as x increases, but on the other hand, the smearing effects of fragmentation to hadrons will become smaller as x decreases ($\sqrt{s}$ increases). The optimum value of x at which to observe three-jet processes should, therefore, be determined by a compromise between these two effects.

In sect. 8, we shall present an alternative method for analyzing event shapes in deep inelastic scattering, which involves projecting the momenta in an event onto a particular plane. Although this technique has certain advantages, it does not retain the rotational invariance of the H_l and the resulting insensitivity to transverse momentum of the incoming quark and gluon. We shall discuss both techniques in more detail in a later publication.

Energy correlation functions (see subsect. 2.6) may also be useful in studies of deep inelastic scattering events.

8. Shape parameters for projections of events onto planes

There is no natural plane defined in an e^+e^- annihilation event. In other processes the directions of initial or final particles often define a plane, and it may be useful to analyze the 'shapes' of events projected onto this plane. For this purpose, define a set of observables

$$C_l = \left| \sum_i \frac{|\boldsymbol{p}_i|_{\text{proj}}}{\sqrt{s}}\, e^{il\phi_i} \right|^2 = \sum_{i,j} \frac{|\boldsymbol{p}_i|_{\text{proj}} |\boldsymbol{p}_j|_{\text{proj}}}{s} \cos[l(\phi_i - \phi_j)]\,, \tag{8.1}$$

where the sum runs over all particles or pairs of particles in each event, and the angles ϕ_i are measured with respect to an axis chosen in the plane, II. ($|\boldsymbol{p}_i|_{\text{proj}}$ are the magnitudes of the particles' momenta projected into the plane II.) The values of the C_l will be independent of the axis used, so long as it lies in II.

The occurrence of the $Y_l^m(\Omega)$ in the definition (1.1) of the 'shape' parameters H_l is a consequence of the fact that these functions form bases for the irreducible representations of the three-dimensional rotation group. It is the functions $e^{il\phi}$ which form bases for the representations (which are all trivial) of the two-dimensional rotation group, U(1), and so appear in the definition (8.1) of 'shape' parameters for two-dimensional projections of events.

To discuss the properties of the C_l, let us consider a continuous distribution $\rho(\phi)$ around a circle. In this case the C_l are given by

$$C_l = \left| \int_0^{2\pi} \rho(\phi)\, e^{il\phi}\, d\phi \right|^2 . \tag{8.2}$$

The C_l obtained using an axis rotated by an angle χ from the original axis are then given by

$$(C_l)' = \left| \int_0^{2\pi} \rho(\phi + \chi)\, e^{il\phi} d\phi \right|^2 = C_l , \tag{8.3}$$

thus proving the invariance of the C_l under rotations in the plane II. If another plane is chosen, then their values will clearly change.

If $\rho(\phi)$ is taken to be the amplitude of an electric current as a function of time, with period 2π, then C_l is simply the power in the lth harmonic of the signal.

The correlation function for the C_l may be defined in analogy to the function $F(x)$ (eq. (2.7)):

$$R(\chi) = \int_0^{2\pi} \rho(\phi + \chi)\, \rho^*(\phi)\, d\phi . \tag{8.4}$$

Defining the Fourier coefficients for the function $\rho(\phi)$ as

$$a_l = \frac{1}{\sqrt{2\pi}} \int \rho(\phi)\, e^{il\phi} d\phi , \tag{8.5}$$

the correlation function becomes

$$R(\chi) = \frac{1}{2\pi} \sum_{l,l'} \int e^{-il\chi}\, e^{i(l'-l)\phi} a_l a_{l'}^* d\phi = \frac{1}{2\pi} \sum_l e^{-il\chi} C_l . \tag{8.6}$$

This is the analogue for $R(\chi)$ of the series (2.10) for $F(x)$.

If all particles in the final state of an event are included in the sum (8.1), then

$$C_1 = 0 , \tag{8.7}$$

by momentum conservation. The value of C_0 depends on the plane chosen. It will,

therefore, usually be convenient to consider the observables C_l/C_0.

As an example of the use of the C_l, consider the process $e^+e^- \to q\bar{q}$. C_0 will be maximal if the q and $\bar{q}$ momenta lie in the plane (Π). All the C_l will be zero if the q and $\bar{q}$ momenta are perpendicular to Π. Except in this case it is clear that

$$\begin{aligned} C_l/C_0 &= 0\,, \qquad (l \text{ odd})\,, \\ &= 1\,, \qquad (l \text{ even})\,. \end{aligned} \tag{8.8}$$

In general, if $\rho(\phi)$ consists of a set of N delta functions of equal weight at equally-spaced points around a circle, then

$$\begin{aligned} C_l/C_0 &= 0\,, \qquad (l \neq \lambda N)\,, \\ &= 1\,, \qquad (l = \lambda N)\,, \end{aligned} \tag{8.9}$$

where λ is any integer. If $\rho(\phi)$ is uniform in ϕ, then $C_l = 0$ for all $l \neq 0$.

In deep inelastic lepton-nucleon scattering, the directions of the incoming and outgoing lepton in the target nucleon rest frame define a plane (Π). The hadronic final state may be analyzed by projecting all the hadron momenta on to this plane, and then evaluating the C_l. $\sqrt{s}$ is taken to be the c.m. energy in the γ^*N collision. For a two-jet production process, as illustrated in fig. 49, the C_l/C_0 will be approximately 1 for even l and zero for odd l (assuming the fragments of the target to behave roughly like a point particle). So long as the analysis is made in the nucleon rest frame, 'Fermi motion' of the struck quark within the target nucleon will have little effect on the values of the C_l for the event. A typical three-jet event is shown in fig. 50. Such a process will give $1 > C_l/C_0 \neq 0$ for all $l > 1$. The precise value will depend on assumptions about the structure of the target fragments, and on the momentum distribution of the primary quark or gluon within the nucleon. It will be infrared stable (see sect. 3).

A much better analysis of deep inelastic lepton-nucleon scattering event may be made using the C_l in the plane (Π) orthogonal to the virtual photon (or W) direc-

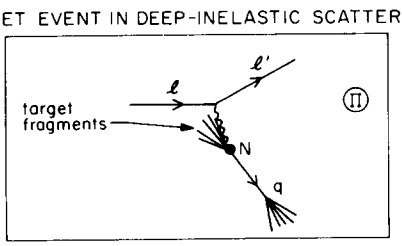

Fig. 49. A typical two-jet event in deep inelastic scattering pictured in the target nucleon rest frame. The momenta of the final hadrons are projected into the plane Π shown for the calculation of the C_l.

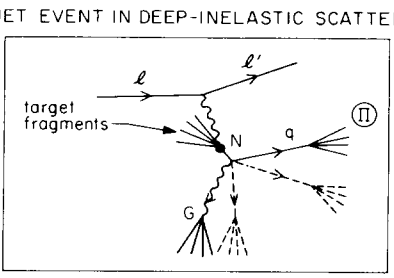

Fig. 50. A typical three-jet event in deep inelastic scattering pictured in the target nucleon rest frame. The projections of the momenta of the final particles into the plane Π used for the calculations of the C_l are shown as dashed lines.

tion. This arrangement for a two-jet event is shown in fig. 51. Treating the target fragments as a point particle, and using the free quark approximation, one finds that $C_l = 0$ for all l in this case. 'Fermi motion' of the initial quark within the target nucleon, the fragmentation of the outgoing quark into hadrons, and allowing for realistic target fragments will all serve to modify this result. Note, however, that a shower of hadrons which has cylindrical symmetry when projected on to Π will make no contribution to the C_l. The arrangement for a three-jet event is shown in fig. 52. The target fragments will be directed approximately perpendicular to Π, and so will not contribute to the C_l for the event. The projections of the momenta of the outgoing quark and gluon (in some events, outgoing q and $\bar{q}$) on to Π will be equal and opposite, by momentum conservation. For three jet events, therefore, $C_l \simeq 0$ for odd l and $C_l/C_0 \simeq 1$ for even l. In idealized three-jet events, $1 \geqslant 0$ for even l, and $C_l = 0$ for odd l. The shapes of the distributions in C_{2l} are similar to those in $1 - H_2$ shown in fig. 23. $\langle C_{2l} \rangle$ is typically 0.06 α_s at $x = 0.1$, rising smoothly to about 0.15

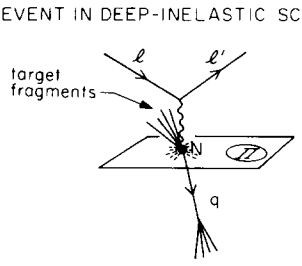

Fig. 51. A typical two-jet event in deep-inelastic scattering. In this case, the plane Π is taken orthogonal to the virtual photon (or W) direction, and the projections of the momenta of the final hadrons on to Π (shown dashed) are distributed roughly symmetrically about the $\gamma^*(W^*)$ direction, so that they give a small value of C_l.

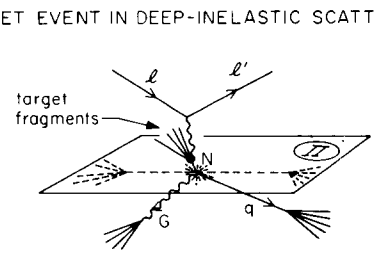

Fig. 52. A typical three-jet event in deep-inelastic scattering, with the plane Π taken orthogonal to the virtual photon (or W) direction.

α_s for $x = 0.8$. Once again, $\gamma^*G \to q\bar{q}$ and longitudinal photons make an insignificant contribution.

The C_l may be computed by measuring the angles ϕ_i of the hadron momenta projected on to the plane Π with respect to any axis in Π. However, in deep inelastic scattering, a natural axis in Π is defined by the projection of the incoming and outgoing lepton (ℓ and ℓ') directions on to Π. In this case, one may define a set of variables analogous to the B_l (see sect. 6):

$$D_l = \sum_i \frac{|p_i|_{\text{proj}}}{\sqrt{s}} \cos(l\alpha_i) , \tag{8.10}$$

where α_i is the angle which particle i makes with the fixed axis in the plane Π. For a two-jet event $D_l \simeq 0$. Three-jet events will have a distribution of values of D_l; the precise form depends on the detailed assumptions made about the inclusion of effects associated with hadrons. Note that because the photon (or W) has spin 1, $D_l = 0$ for $l > 2$. $\langle D_1 \rangle$ is simply the $\langle \boldsymbol{p}_\perp \rangle$ summed over all hadrons in the event relative to the projection of the lepton direction.

Previous authors have considered the possibility of detecting three-jet production in deep inelastic ℓN scattering by measuring the angular distribution of a single particle in the final state [21]. The discussion given in sect. 3 indicates that this procedure should not lead to infrared stable results, since processes involving the emission of particles of indefinitely low energy are distinguished from those in which no particles are emitted. To order g^2, it turns out that the single-particle angular distributions are infrared finite, but this property will not survive in higher orders. This suggests that only angular distributions weighted with momenta and summed over all final particles as in the definition of the D_l should be considered. These will be infrared stable.

We hope to discuss the use of the C_l and D_l in the analysis of final states from deep inelastic lepton-nucleon scattering in a future publication.

The C_l may also be useful in an analysis of the structure of final states in high-energy hadron-hadron (hh') collisions involving the production of jets of hadrons with large transverse momenta ($p_\perp$). We shall work in the c.m.s. for the colliding hadrons. We consider the C_l for a plane Π orthogonal to the directions of the initial

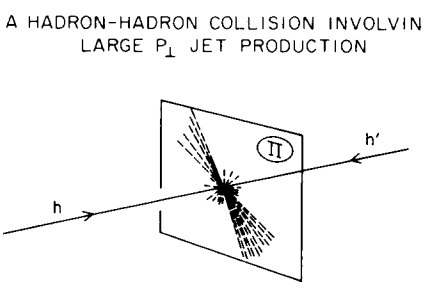

Fig. 53. A typical hadron-hadron collision involving the production of two high transverse momentum jets of hadrons, shown projected on to the plane Π orthogonal to the directions of the incoming particles in their c.m.s.

hadrons, as illustrated in fig. 53. The fragments of the initial hadrons should form a halo of particles around the hh′ axis. Fig. 53 shows a typical event involving the production of two jets of hadrons with high transverse momenta, as expected from QCD models for large $p_\perp$ processes [22]. QCD also predicts that in some events, three high transverse momentum hadron jets should be produced, arising, for example, from the subprocess qq → qqG. Measurements of the C_l could be used to disentangle the different types of event. In an experiment with an azimuthally symmetric trigger, the halo of low $p_\perp$ particles from the fragmentation of the beam and target will be distributed symmetrically about the hh′ axis. Because of their isotropy, these unwanted particles will not contribute significantly to the values of the C_l for an event. Care must be taken if a trigger is used which requires a particle or a jet at a particular azimuthal angle. In that case, the beam and target fragments tend to be directed oppositely to the trigger particles, and will therefore affect the values of the C_l [23]. The application of a transverse momentum cut on the particles used in the calculation of the C_l would, however, remove their effect. (This cut is the two-dimensional analogue of the total momentum cut p_c discussed in sect. 5.4.) Final states containing two high transverse momentum jets will give $C_l/C_0 \simeq 1$ (l even) and $C_l \simeq 0$ (l odd), while those in which more jets are produced will give rise to a wider distribution of C_l values.

It appears that the C_l should provide a powerful tool for the analysis of high $p_\perp$ hadron events. QCD makes definite predictions for the distributions of events in the C_l.

9. Conclusions

In this paper, we have presented several sets of observables for the analysis of the 'shapes' of final states in events of various processes. We have considered mainly e^+e^- annihilation, for which no natural axis is defined in the final state. The H_l

(defined in eq. (1.1)) appear to be the most suitable class of observables for this case since they are rotational invariants whereas previous observables proposed require minimization to find a preferred axis in each event. An axis must be chosen to evaluate the H_l, but their values are independent of the choice. In sect. 2, we showed that the information on the 'shape' of an event contained in the H_l may be reexpressed in a generalized 'correlation function' $F(x)$ for the relative density of particles at different angles. $F(\cos\beta)$ may be interpreted as an energy correlation function between two detectors an angle β apart, in the limit that their areas tend to zero (see subsect. 2.6). In sect. 3, we showed that to order g^2 in QCD perturbation theory, the moments of the H_l are infrared finite, and we gave arguments that this result will survive the inclusion of higher-order effects. ($F(x)$ is not, however, infrared finite.) If the quarks and gluons produced in the primary interaction are allowed to fragment into hadrons, then the resulting distributions in the H_l are also infrared finite. The reason for this is that the fragmentation process acts somewhat like a detector with finite energy (and angular) resolution and properly averages over 2-jet events ($q\bar{q}$) and 3-jet events ($q\bar{q}G$) that are 'near' the two-jet kinematic configuration.

For the process $e^+e^- \to q\bar{q}$, $H_l = 1$ for even l, and $H_l = 0$ for odd l. Energy-momentum conservation requires $H_0 \simeq 1$ and $H_1 = 0$. For final states consisting of three quarks and gluons, H_2 and H_3 are simple functions of the energies of the final particles. We gave analytic expressions for $\langle H_2 \rangle$ and $\langle H_3 \rangle$ for the processes $e^+e^- \to \zeta \to$ GGG, where ζ is a heavy vector meson containing a pair of heavy quarks, and $e^+e^- \to q\bar{q}(G)$. The latter process is defined to be a combination of $e^+e^- \to q\bar{q}$ and $e^+e^- \to q\bar{q}G$. According to QCD, only this combination should be present. The fact that $\langle H_2 \rangle$ and $\langle H_3 \rangle$ are finite for that case is an explicit demonstration of the infrared stability of the H_l to order g^2.

We used the Field-Feynman model for the fragmentation of quarks and gluons into hadrons. We found that for c.m. energies above about $\sqrt{s} = 10$ GeV, the distributions of events in H_2 and H_3 allow good differentiation between the various mechanisms. The H_2 distribution was particularly powerful at distinguishing the processes $e^+e^- \to q\bar{q}(G)$ and $e^+e^- \to \zeta \to$ GGG, while the H_3 distribution should provide a good measure of any pure $e^+e^- \to q\bar{q}$ processes. At least $\sqrt{s} \simeq 30$ GeV is required, however, before the H_2 and H_3 distributions for realistic hadronic events become similar to those obtained in the free quark and gluon approximation. Only for these energies can the H_2 and H_3 distributions be considered as direct quantitative tests of perturbative QCD; at lower energies, the details of the distributions calculated from QCD perturbation theory are blurred by the fragmentation of the quarks and gluons into hadrons. The agreement between the results for realistic hadron final states and for free quarks and gluons can be improved slightly by considering only the higher-momentum hadrons in each event. This procedure does not affect the discrimination between different types of events offered by the H_l; it merely gives results which are closer to the free quark and gluon approximation.

We also considered the production and decay of heavy leptons and of mesons

containing heavy quarks. These processes give rise to events of a rather spherical 'shape', which should be clearly distinguished from other types of event. Several possible mechanisms for the weak decays of heavy mesons were considered. It should be possible to discriminate between them on the basis of measurements of the 'shapes' of events using the H_l.

In sect. 6, we discussed a class of observables (B_l) which use the direction of the incoming beams as an axis and are, therefore, not rotationally invariant. There is no clean separation of $e^+e^- \to q\bar{q}$ and $q\bar{q}(G)$ in the B_l distributions and generally they do not provide very good discrimination between different types of events, although events involving heavy quark or lepton production could be distinguished by their use.

In sect. 7, we considered the extension of our analysis of event shapes in e^+e^- annihilation to final states in deep inelastic lepton-hadron scattering. The main difficulty in this case is the presence of fragments of the target in the final state. Nevertheless, it appears that the H_l could be used to identify three-jet final states in deep inelastic scattering.

Finally, in sect. 8, we gave a very brief discussion of the analogues of the H_l in two dimensions (the C_l). These should be useful for analyses of final states in which a natural plane is defined. If this plane is chosen to be orthogonal to the virtual photon direction in the target nucleon's rest frame, then idealized two-jet events in deep inelastic lepton-nucleon scattering give $C_l \simeq 0$, while three-jet ones give non-zero values for C_{2l}. The C_l also promise to be useful in the analysis of hadron-hadron collisions involving the production of particles with large transverse momenta. The related variables D_l, also discussed in sect. 7, appear to allow a more precise formulation of certain azimuthal angular correlations that have been previously proposed as tests of QCD.

We hope to present more detailed analyses of the 'shapes' of events in deep inelastic lepton-nucleon scattering in a future publication.

We are grateful to R.D. Field and R.P. Feynman for the use of their jet-development computer program, and to the MATHLAB group of the MIT Laboratory for Computer Science for the use of MACSYMA.

Appendix

Three-jet kinematics

The momenta for e^+e^- annihilation to three particles *via* a virtual photon are assigned according to fig. 54. In our calculations, at most one of the final particles has a non-zero mass, and, in this case, the kinematics for the process become very

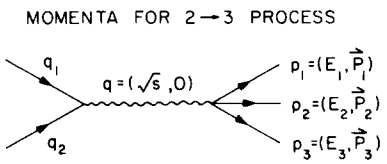

Fig. 54. Definitions of the momenta for a $2 \to 3$ process.

simple. Let us work in the rest frame of the 'decaying' virtual photon, so that

$$\boldsymbol{q} = \boldsymbol{p}_1 + \boldsymbol{p}_2 + \boldsymbol{p}_3 = 0 ,$$

$$E_1 + E_2 + E_3 = \sqrt{s} . \tag{A.1}$$

Now define

$$x_i = \frac{2E_i}{\sqrt{s}}, \qquad (i = 1, 2, 3) . \tag{A.2}$$

Energy conservation demands

$$\sum x_i = 2 . \tag{A.3}$$

Take particle 3 to be massive, and write

$$p_1^2 = p_2^2 = 0 , \qquad p_3^2 = \mu^2 . \tag{A.4}$$

Then

$$q = (\sqrt{s}, 0, 0, 0) ,$$

$$p_i = \tfrac{1}{2} x_i \sqrt{s}\, (1, 0, \sin \alpha_i, \cos \alpha_i) , \qquad (i = 1, 2) . \tag{A.5}$$

The expression for p_3 does not have such a simple form. However, for all i and $j (k \neq i \neq j)$

$$\begin{aligned} p_i \cdot p_j &= p_i \cdot (q - p_k) - p_i^2 = p_j \cdot (q - p_k) - p_j^2 \\ &= \tfrac{1}{2}[(p_i + p_j) \cdot (q - p_k) - p_i^2 - p_j^2] \\ &= \tfrac{1}{2}[q^2 - 2q \cdot p_k + p_k^2 - p_i^2 - p_j^2] . \end{aligned} \tag{A.6}$$

If all the final particles are massless, this gives

$$p_i \cdot p_j = \tfrac{1}{2} s (1 - x_k) . \tag{A.7}$$

When particle 3 has mass μ, define

$$\beta = \frac{\mu^2}{s} = \frac{p_3^2}{s} . \tag{A.8}$$

Then

$$p_1 \cdot p_2 = \tfrac{1}{2}s[1 - x_3 + \beta] ,$$
$$p_2 \cdot p_3 = \tfrac{1}{2}s[1 - x_1 - \beta] , \tag{A.9}$$
$$p_1 \cdot p_3 = \tfrac{1}{2}s[1 - x_2 - \beta] .$$

Now

$$p_1 \cdot p_2 = E_1 E_2 (1 - \cos\phi_{12})$$
$$= \tfrac{1}{4}x_1 x_2 s(1 - \cos\phi_{12}) = \tfrac{1}{2}s[x_1 + x_2 - 1 + \beta] , \tag{A.10}$$

so that the angle ϕ_{12} between the three-momenta of particles 1 and 2 is given by

$$\cos\phi_{12} = 1 - \frac{2[x_1 + x_2 - 1 + \beta]}{x_1 x_2}$$

$$= \frac{2[(1 - x_1)(1 - x_2) - \beta]}{x_1 x_2} - 1 . \tag{A.11}$$

The physical region for the process of fig. 54 is determined simply by demanding that

$$-1 \leqslant \cos\phi_{12} \leqslant 1 , \tag{A.12}$$

which implies

$$(1 - x_1)(1 - x_2) \geqslant \beta , \qquad x_1 + x_2 \geqslant 1 - \beta . \tag{A.13}$$

The physical region for a characteristic value of β is illustrated in fig. 55. Solving the inequalities (A.13), one finds that

$$(1 - \beta - x_1) \leqslant x_2 \leqslant \left(\frac{1 - x_1 - \beta}{1 - x_1}\right) , \tag{A.14}$$

while

$$0 \leqslant x_1 \leqslant 1 - \beta . \tag{A.15}$$

The expressions for $\cos\phi_{13}$ and $\cos\phi_{23}$ are simple only if all the final particles are massless, in which case

$$\cos\phi_{ij} = 1 - \frac{2(1 - x_k)}{x_i x_j} , \qquad (i \neq j \neq k) \tag{A.16}$$

The momenta q_1 and q_2 of the incoming electron and positron clearly satisfy

$$q_1 \cdot q_2 = \tfrac{1}{2}s \tag{A.17}$$

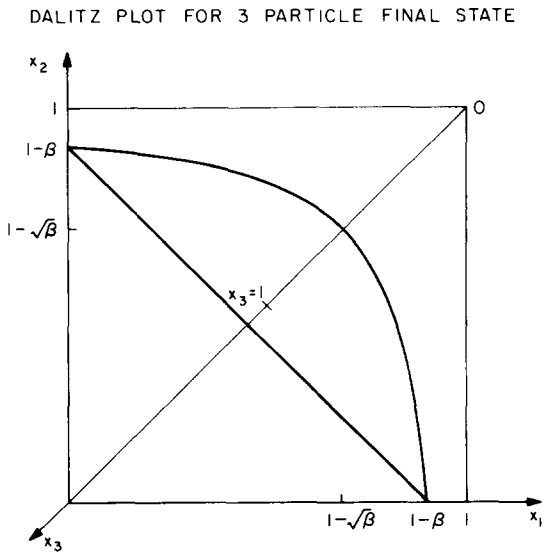

Fig. 55. The physical region in the fractional energies $x_i = 2E_i/\sqrt{s}$ for a process with three final-state particles. Particles 1 and 2 are taken to be massless, while particle 3 has a mass $\mu = \sqrt{\beta s}$.

in their c.m. frame (virtual photon rest frame). Momentum conservation requires the momenta of the final particles to lie in a plane. Let θ be the angle which the normal (N) to this plane makes with the direction of the electron's momentum. Then, if all the particles are massless,

$$q_1 \cdot p_i = \tfrac{1}{4} s x_i (1 - \sin\theta \cos\phi_i), \qquad (i = 1, 2, 3),$$
$$q_2 \cdot p_i = \tfrac{1}{4} s x_i (1 + \sin\theta \cos\phi_i), \tag{A.18}$$

where ϕ_i are the angles of the final particles' momenta relative to the axis formed by the intersection of the plane containing N and the e^- direction with the plane of the final particles.

References

[1] B.H. Wiik and G. Wolf, A review of e^+e^- interactions, DESY preprint 78/23 (May 1978).
[2] G. Sterman and S. Weinberg, Phys. Rev. Lett. 39 (1977) 1436.
[3] J. Ellis, M.K. Gaillard and G.G. Ross, Nucl. Phys. B111 (1976) 253.
[4] T. Applequist and H.D. Politzer, Phys. Rev. Lett. 34 (1975) 43; Phys. Rev. D12 (1975) 1404.
[5] H. Georgi and M. Machacek, Phys. Rev. Lett. 39 (1977) 1237;
E. Farhi, Phys. Rev. Lett. 39 (1977) 1587;
S.-Y. Pi, R.L. Jaffe and F.E. Low, Phys. Rev. Lett. 41 (1978) 142.

[6] A. de Rújula, J. Ellis, E.G. Floratos and M.K. Gaillard, Nucl. Phys. B138 (1978) 387.
[7] M.G. Rossman (ed.), The molecular replacement method (Gordon and Breach, New York, 1972).
[8] T. Kinoshita, J. Math. Phys. 3 (1962) 650;
T.D. Lee and M. Nauenberg, Phys. Rev. 133 (1964) B1549;
G. Sterman, Phys. Rev. D14 (1976) 2123.
[9] J. Frenkel, R. Meuldermans, I. Mohammad and J.C. Taylor, Nucl. Phys. B121 (1977) 58.
[10] H. Georgi and H.D. Politzer, Nucl. Phys. B136 (1978) 445.
[11] T. Applequist and H. Georgi, Phys. Rev. D8 (1973) 4000;
A. Zee, Phys. Rev. D8 (1973) 4038.
[12] S. Wolfram, Non-logarithmic terms and the effective coupling, Caltech preprint in preparation.
[13] A. Ore and J.L. Powell, Phys. Rev. 75 (1949) 1696.
[14] M. Krammer and H. Krasemann, Phys. Lett. 73B (1978) 58.
[15] L. Lewin, Dilogarithms and associated functions (McDonald, 1958).
[16] I.S. Gradshteyn and I.M. Ryzhik, Table of integrals, series and products, (Academic Press, New York, 1965).
[17] G.C. Fox and S. Wolfram, Tests for coplanar events in e^+e^- annihilation, Phys. Lett. B, in press.
[18] R.D. Field and R.P. Feynman, Nucl. Phys. B136 (1978) 1.
[19] W.G. Scott, *in* 'Neutrinos-78', ed. E.C. Fowler, Purdue, 1978.
[20] U. Sukhatme and J. Tran Thanh Van, Phys. Lett. 76B (1978) 489.
[21] H. Georgi and H.D. Politzer, Phys. Rev. Lett. 40 (1978) 3;
A. Méndez, Nucl. Phys. B145 (1978) 199.
[22] R.P. Feynman, R.D. Field and G.C. Fox, Phys. Rev. D18 (1978) 3320.
[23] M.G. Albrow et al., Nucl. Phys. B135 (1978) 461.
[24] S. Brandt and H.D. Dahmen, Axes and scalar measures of two-jet and three-jet events, Z. Phys. C, in press.
[25] G. Sterman, Phys. Rev. D17 (1978) 2789.
[26] G. Källén and A. Sabry, Mat. Fys. Medd. Dan. Vid. Selsk, 29 (1955) no.17.
[27] C.L. Basham, L.S. Brown, S.D. Ellis and S.T. Love, Phys. Rev. D17 (1978) 2298.
[28] C.L. Basham, L.S. Brown, S.D. Ellis and S.T. Love, Phys. Rev. Lett. 41 (1978) 1585.
[29] G.C. Fox and S. Wolfram, Energy correlations in e^+e^- annihilation events, Caltech preprint in preparation.
[30] K. Koller, H. Krasemann and T.F. Walsh, The 3-gluon decay of quarkonium, DESY preprint, 78/37 (1978).
[31] G.C. Fox and S. Wolfram, Phys. Rev. Lett. 41 (1978) 1581.